

# The Mechanism of Rhodium Catalyzed Allylic C–H Amination

Robert Harris, Jiyong Park, Taylor Nelson, Nafees Iqbal, Daniel Salgueiro, John Bacsa, Cora MacBeth, Mu-Hyun Baik, Simon Blakey

Submitted date: 01/09/2019 • Posted date: 04/09/2019

Licence: CC BY-NC-ND 4.0

Citation information: Harris, Robert; Park, Jiyong; Nelson, Taylor; Iqbal, Nafees; Salgueiro, Daniel; Bacsa, John; et al. (2019): The Mechanism of Rhodium Catalyzed Allylic C–H Amination. ChemRxiv. Preprint.

The mechanism of catalytic allylic C–H amination reactions promoted by Cp\*Rh complexes is reported. Reaction kinetics experiments, stoichiometric studies, and DFT calculations demonstrate that allylic C–H activation to generate a Cp\*Rh( $\pi$ -allyl) complex is viable under mild reaction conditions. The role of external oxidant in the catalytic cycle is elucidated. Quantum mechanical calculations, stoichiometric reactions, and cyclic voltammetry experiments support an oxidatively induced reductive elimination process of the allyl fragment with an acetate ligand. Lastly, evidences supporting the amination of an allylic acetate intermediate is presented. Both nucleophilic substitution catalyzed by Ag<sup>+</sup> that behaves as a Lewis acid catalyst and an inner-sphere amination catalyzed by Cp\*Rh are shown to be viable for the last step of the allylic amination reaction.

## File list (3)

Blakey-Baik-Rh-AllylicCHAMination-Mechanism.pdf (3.16 MiB)	<a href="#">view on ChemRxiv</a> • <a href="#">download file</a>
Blakey-Baik-Rh-AllylicCHAMination-Mechanism.docx (2.69 MiB)	<a href="#">view on ChemRxiv</a> • <a href="#">download file</a>
Compiled Allylic Amination Mechanism SI.pdf (8.76 MiB)	<a href="#">view on ChemRxiv</a> • <a href="#">download file</a>

# The Mechanism of Rhodium Catalyzed Allylic C–H Amination

Robert J. Harris,<sup>†</sup> Jiyong Park<sup>‡,§</sup>, Taylor A. F. Nelson,<sup>†</sup> Nafees Iqbal,<sup>‡,§</sup> Daniel C. Salgueiro,<sup>†</sup> John Bacsa,<sup>†</sup> Cora E. MacBeth,<sup>†</sup> Mu-Hyun Baik<sup>\*,§,‡</sup> and Simon B. Blakey<sup>\*,†</sup>

<sup>†</sup>Department of Chemistry, Emory University, Atlanta, GA, 30322, U.S.A.

<sup>‡</sup>Department of Chemistry, Korea Advanced Institute of Science and Technology (KAIST), Daejeon 34141, Republic of Korea

<sup>§</sup>Center for Catalytic Hydrocarbon Functionalizations, Institute for Basic Science (IBS), Daejeon 34141, Republic of Korea

## ABSTRACT

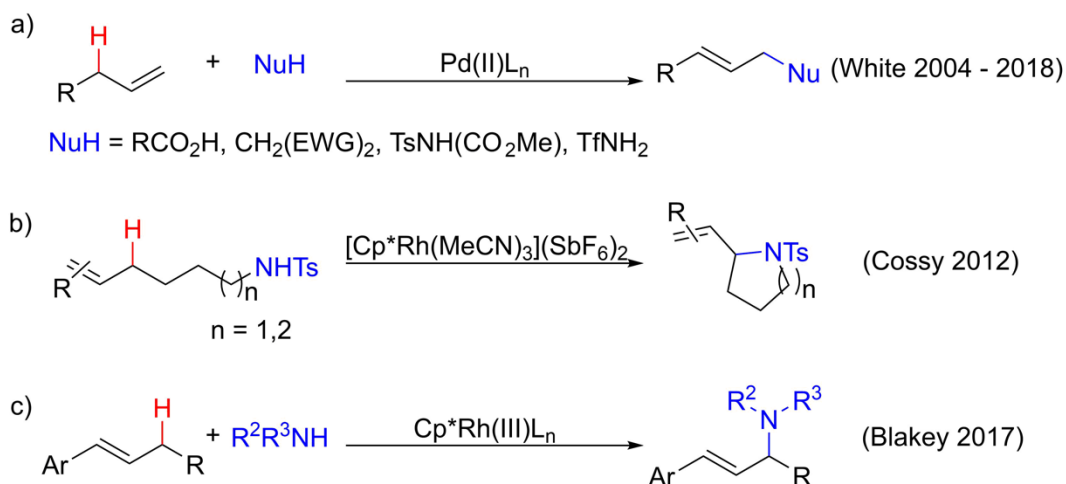
The mechanism of catalytic allylic C–H amination reactions promoted by Cp<sup>\*</sup>Rh complexes is reported. Reaction kinetics experiments, stoichiometric studies, and DFT calculations demonstrate that allylic C–H activation to generate a Cp<sup>\*</sup>Rh( $\pi$ -allyl) complex is viable under mild reaction conditions. The role of external oxidant in the catalytic cycle is elucidated. Quantum mechanical calculations, stoichiometric reactions, and cyclic voltammetry experiments support an oxidatively induced reductive elimination process of the allyl fragment with an acetate ligand. Lastly, evidences supporting the amination of an allylic acetate intermediate is presented. Both nucleophilic substitution catalyzed by Ag<sup>+</sup> that behaves as a Lewis acid catalyst and an inner-sphere amination catalyzed by Cp<sup>\*</sup>Rh are shown to be viable for the last step of the allylic amination reaction.

**Keywords:** Density Functional Theory, C–H amination, Rhodium, Allylic functionalization, Mechanism

## INTRODUCTION

Transition-metal-mediated direct activation of C(sp<sup>3</sup>)-H bonds to install C-X (X = C, N, and O) functionalities has become an indispensable method in modern synthetic strategy. Precisely controlling the regio- and diastereo-selectivities in these reactions is a key challenge that has been achieved using directing groups<sup>1</sup> or by taking advantage of the inherent reactivities of the C-H bonds.<sup>2</sup> Direct and efficient synthetic protocols that afford desired selectivities continue to be actively sought after. In 2004, White and co-workers reported the catalytic allylic C-H acetoxylation of terminal olefins in complex settings catalyzed by palladium.<sup>3</sup> In a series of reports that followed, Pd( $\pi$ -allyl) intermediates were intercepted with a variety of stabilized carbon, nitrogen, and oxygen nucleophiles (Scheme 1a).<sup>4</sup> Cossy and co-workers subsequently reported the use of Cp<sup>\*</sup>Rh to catalyze the intramolecular cyclization of aminoalkenes by allylic C-H functionalization, as illustrated in Scheme 1b.<sup>5</sup> More recently our group disclosed the intermolecular allylic C-H amination of internal aryl and alkyl alkenes with primary and secondary amines bearing only one electron withdrawing group (Scheme 1c).<sup>6</sup>

**Scheme 1.** Transition metal catalyzed allylic C-H amination with nucleophilic amines



The development of catalytic methods for C(sp<sup>3</sup>)-H functionalization has exceeded our mechanistic understanding of these transformations. In the case of rhodium catalyzed allylic C-H functionalization, Cossy suggested that a plausible mechanism would involve an allylic C-H insertion to generate a Rh( $\pi$ -allyl) complex followed by N-metallation and reductive elimination from a Rh(III) intermediate to generate the allylic amine and a Rh(I) species that would be reoxidized to Rh(III) to complete the catalytic cycle. This mechanism is in accord with reports on the rhodium catalyzed allylic substitution with phosphine and phosphite supporting ligands.<sup>7</sup> Similar catalytic reactions involving Rh(III/I) have also been proposed for C(sp<sup>2</sup>)-H bond activations that utilize cyclopentadienyl supporting ligands.<sup>8</sup> However, we note that higher oxidation states of rhodium have also been proposed in Cp<sup>\*</sup>Rh catalyzed C(sp<sup>2</sup>)-H activation.<sup>9</sup>

Providing additional complexity to the mechanistic picture, the synthesis and reactivity of several group IX  $\pi$ -allyl complexes similar to those invoked by Cossy and our group in the Cp<sup>\*</sup>Rh catalyzed allylic C-H amination have been reported. Bergman isolated and characterized the Cp<sup>\*</sup>Rh( $\pi$ -allyl) complex **I** (Figure 1a)<sup>10</sup> and Stryker

subsequently determined the structures of the *exo* and *endo* isomers of IrCp\*( $\pi$ -allyl) complex **II** (Figure 1b).<sup>10b</sup> In each case, the *exo*-isomers of the  $\pi$ -allyl complexes react with hard nucleophiles at the central carbon to generate metallocyclobutane products. Additionally, Tanaka reported the isolation and characterization of the Rh(III)Cp<sup>E</sup>( $\pi$ -allyl) complex **III** bearing a pendent tosyl amine nucleophile (Figure 1c).<sup>10c</sup> When complex **III** was treated with AgSbF<sub>6</sub> to abstract the chloride and generate a vacant coordination site for *N*-metallation, the expected cyclization product was not observed. When complex **III** was treated with both AgSbF<sub>6</sub> and Cu(OAc)<sub>2</sub>, the expected amination product was observed in 51% yield. The authors did not postulate specific roles of Cu(OAc)<sub>2</sub> in this transformation. However, Jones and coworkers have reported the use of a copper salt as an oxidant to induce reductive elimination of a C(sp<sup>2</sup>)–N(sp<sup>2</sup>) bond from a Cp\*Rh<sup>III</sup> complex.<sup>9b</sup> In 2017, Chang and Baik reported a detailed mechanistic study of a C–H arylation reaction catalyzed by Cp\*Ir, in which a strong oxidant facilitates the C–H arylation by oxidizing the metallated  $\pi$ -allyl complex via an oxidatively induced reductive elimination (Figure 1d).<sup>11</sup>

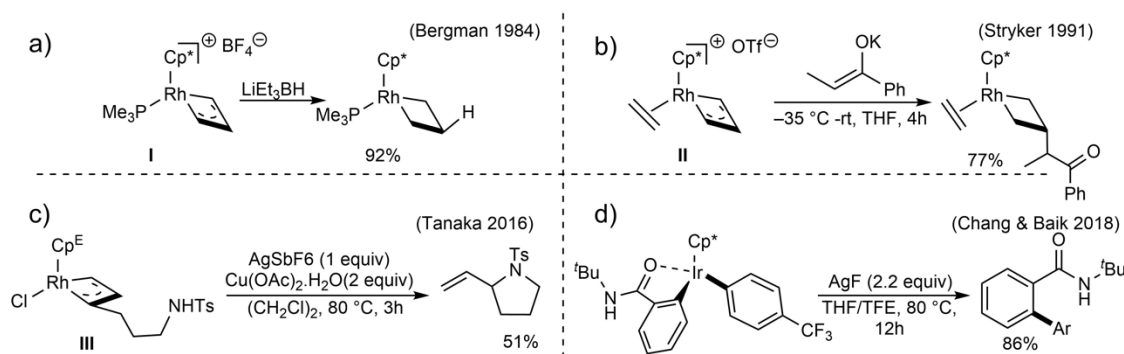
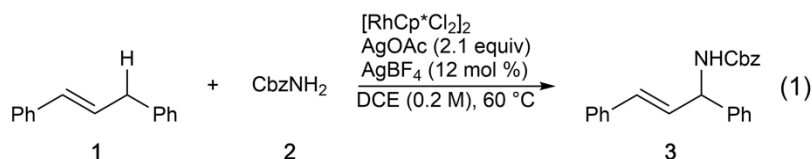


**Figure 1.** Previously reported reactions of group IX  $\pi$ -allyl complexes

The reactivity of  $\pi$ -allyl complexes (**I–III**) is largely inconsistent with the previously proposed Rh(III/I) mechanism for Cp\*Rh catalyzed allylic C–H amination. Herein, we describe a detailed study combining experimental observations including kinetic analysis, isolation and characterizations of reactivities of putative intermediates, and cyclic voltammetry measurements, that are corroborated with quantum mechanical calculations, to elucidate the mechanism of the Rh-catalyzed C(sp<sup>3</sup>)–H activations that afford allylic amination products.

## RESULTS AND DISCUSSION

**Kinetic analysis:** To obtain experimental data to facilitate a deeper understanding of the mechanism for the rhodium catalyzed allylic C–H amination, we targeted 1,3-diphenylpropene **1** as a simple model substrate, in which complications caused by regioselectivity are not present (eq 1). We note that our initial attempt to monitor the reaction progress using *p*-toluenesulfonamide as a nucleophile was complicated due to its insolubility, leading us to choose benzyl carbamate as the nucleophile.



Analysis of initial rates of reactions of diphenylpropene **1** with benzyl carbamate **2** catalyzed by [Cp\*RhCl<sub>2</sub>]<sub>2</sub>/AgBF<sub>4</sub> showed that allylic amine production was linearly dependent on the concentrations of the Rh,



alkene, and carbamate with slopes of  $k_1 = 2.4 \pm 0.4 \times 10^{-4} \text{ s}^{-1}$ ,  $k_2 = 1.5 \pm 0.1 \times 10^{-5} \text{ s}^{-1}$  and  $k_3 = -5.2 \pm 0.6 \times 10^{-5} \text{ s}^{-1}$  respectively (Figures S2-S4). These data indicate the reaction is first-order in rhodium and alkene concentrations. Also an inverse rate constant for the carbamate concentration was observed, that is consistent with the carbamate nucleophile binding to the rhodium catalyst in an off cycle equilibrium (Scheme S1).

Deuterium exchange experiments provide insight into the rate determining step (RDS). A 1:1 mixture of **1** and **1-d<sub>2</sub>** (0.2 M) in DCE was treated with benzyl carbamate **2** (0.49 M), [Cp\*RhCl<sub>2</sub>]<sub>2</sub> ([Rh] = 12 mM), AgBF<sub>4</sub> (26 mM), and AgOAc (2.1 equiv). The reaction was stopped after 2 hours (~10% conversion), and allylic amine **3** was isolated in 5% yield (Figure 2). Analysis of the <sup>1</sup>H NMR of **3** established a 14% deuterium incorporation at both C1 and C3, which is consistent with a primary KIE of  $k_H/k_D = 2.5$ . In our original disclosure of the rhodium catalyzed allylic C–H amination, we showed that C–H cleavage was irreversible.<sup>6</sup> Taken together, these observations along with the first order dependence of rate on **1**, establish that C–H cleavage is rate-determining.<sup>11</sup>

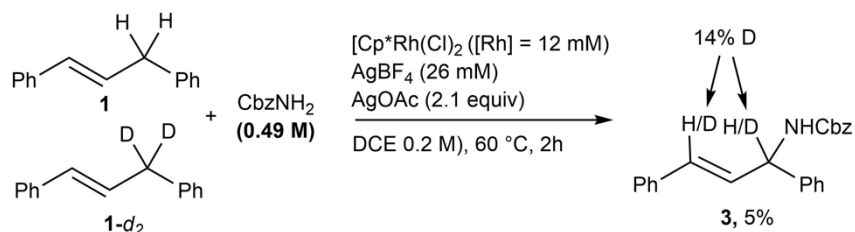


**Figure 2.** Amination of a 1:1 mixture of **1** and **1-d<sub>2</sub>** with benzyl carbamate catalyzed by [Cp\*RhCl<sub>2</sub>]<sub>2</sub>

### Synthesis, Characterization, and Reactivity of rhodium $\pi$ -allyl complexes

The kinetic data presented above are consistent with the notion that C–H activation step is rate limiting, and consequently overall reaction kinetics cannot be used to probe the mechanism of C–N bond formation or catalyst regeneration. In order to gain insight into this sequence in the catalytic cycle, we synthesized plausible putative intermediates in the catalytic cycle and examined their reactivities. Analogous to Tanaka's synthesis of Cp<sup>F</sup>Rh( $\pi$ -allyl) complex **III**, we attempted to synthesize a Rh( $\pi$ -allyl) complex with a Cp\* supporting ligand. Initial attempts to make a Cp\*Rh( $\pi$ -allyl) complex starting from [Cp\*RhCl<sub>2</sub>]<sub>2</sub> in the presence of AgSbF<sub>6</sub> were unsuccessful and led to a complex mixture of products. However, stirring [Cp\*Rh(NCMe)<sub>3</sub>](SbF<sub>6</sub>)<sub>2</sub> with cesium acetate (1.5 equiv) and 4-phenyl-1-butene (2 equiv) in CH<sub>2</sub>Cl<sub>2</sub> at room temperature for 16 h followed by the addition of tetraethylammonium chloride, lead to the isolation of a mixture of Rh( $\pi$ -allyl) complexes **IV** and **V** in 53% yield (9:1 ratio, Figure 3a). By using DCE as a solvent and heating the reaction to 80 °C we were able to isolate complex **V** exclusively as the thermodynamic product in 61% yield (Figure 3b).

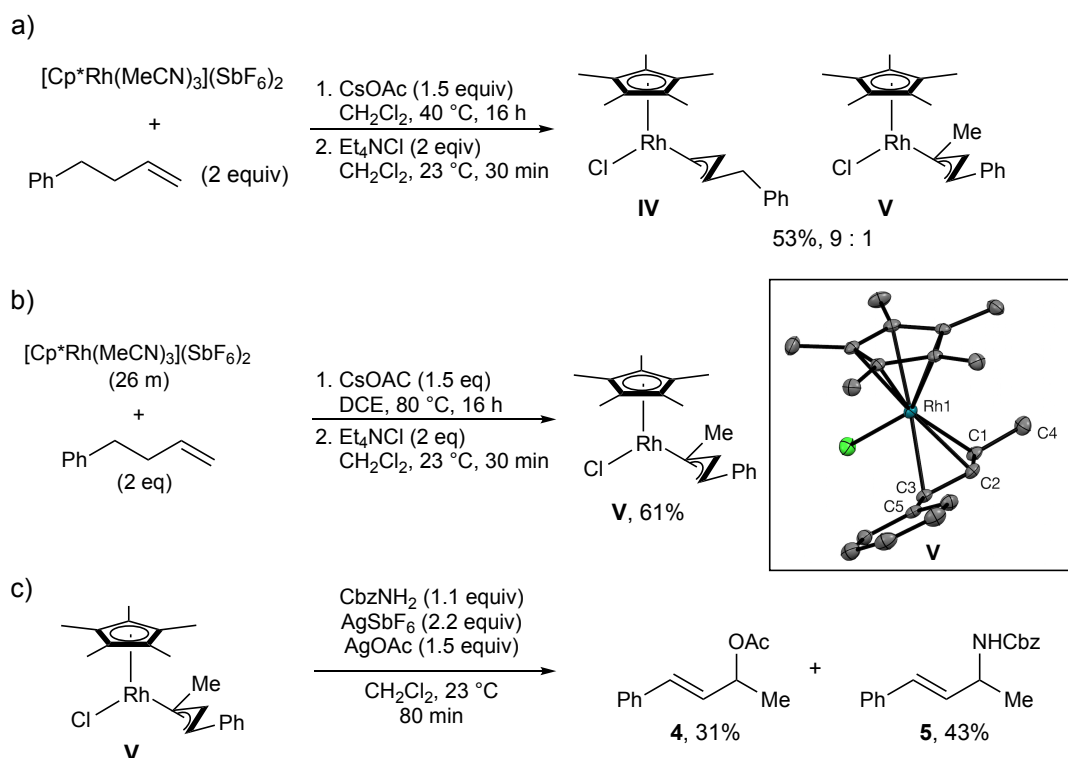


**Figure 3.** Synthesis and structure of Cp\*Rh( $\pi$ -allyl)Cl complex. ORTEP diagram of **V** depicted with ellipsoids shown at the 50% probability level and hydrogen atoms omitted for clarity

Complex **V** was fully characterized by  $^1\text{H}$  and  $^{13}\text{C}$  NMR spectroscopy and single crystal X-ray diffraction. The  $^1\text{H}$  NMR spectrum of **V** displayed a characteristic triplet of doublets at  $\delta = 4.55$  ppm with coupling constants  $J_{\text{HH}} = 10.7$  Hz and  $J_{\text{RhH}} = 2.0$  Hz corresponding to the proton attached to the central carbon of the  $\pi$ -allyl ligand. Vapor diffusion of pentane into a concentrated ether solution of **V** at 25 °C provided crystals suitable for X-ray analysis (Figure 3b, inset). The allyl ligand of complex **V** adopts a near planar geometry with dihedral angles  $\text{C1} - \text{C2} - \text{C3} - \text{C5} = 173.8^\circ$  and  $\text{C4} - \text{C1} - \text{C2} - \text{C3} = 178.6^\circ$ . The Rh–C1 and Rh–C3 bond distances are approximately equal with bond lengths of 2.203(2) and 2.219(2) Å respectively while the Rh–C2 bond length is significantly shorter with a bond length of 2.133(2) Å.

With complex **V** in hand, we began to investigate Cp\*Rh( $\pi$ -allyl) complexes' reactivity toward nucleophiles. In an initial experiment, complex **V** was treated with a single equivalent of benzyl carbamate **2** in  $\text{CH}_2\text{Cl}_2$  at 23 °C. Unsurprisingly, even after 48 h, complex **V** remained unreacted. However, when complex **V** was treated with benzylcarbamate (**2**, 1.1 equiv) in the presence of  $\text{AgSbF}_6$  (2.2 equiv, as a halide abstractor) and  $\text{AgOAc}$  (1.5 equiv) in  $\text{CH}_2\text{Cl}_2$  at 23 °C to mimic the reaction conditions that yielded aminated products, allylic acetate **4** and the expected allylic amine **5** were generated in 31% and 43% yield respectively (Figure 3c). This result suggests that while **V** is likely not a catalytically relevant species, the cationic complex generated from abstracting a chloride from **V** could be. Also the result indicate that silver additives are essential for the activation of the Rh( $\pi$ -allyl) complex **V**. Lastly, the significant quantities of allylic acetate **4** observed in the reaction lead us to consider the possibility that the amination reaction might proceed through an allylic acetate intermediate.

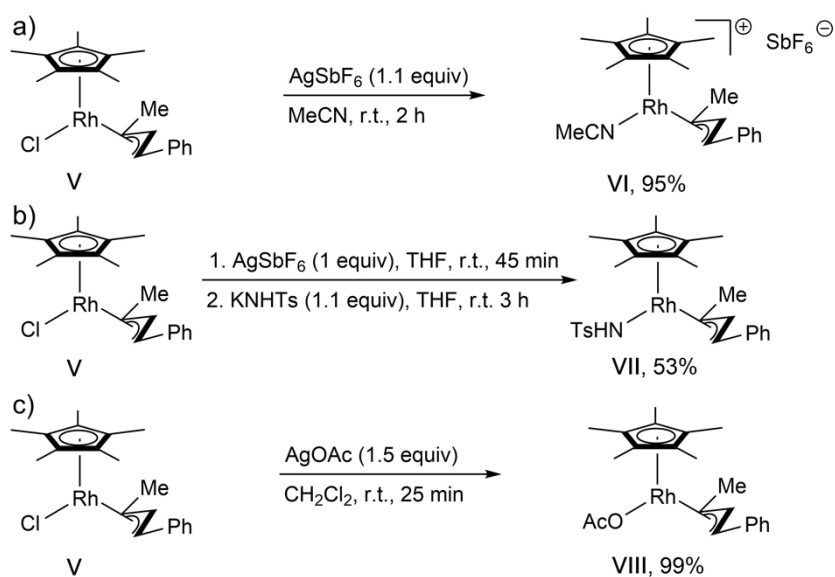


**Figure 4.** Synthesis of Cp<sup>\*</sup>Rh(III)(π-allyl) complexes bearing acetonitrile, tosylamine and acetate ligands

To further probe these possibilities we synthesized the cationic Cp<sup>\*</sup>Rh(π-allyl)(MeCN)(SbF<sub>6</sub>) complex **VI** (Figure 4a), the Cp<sup>\*</sup>Rh(π-allyl)(NHTs) complex **VII** (Figure 4b) and the Cp<sup>\*</sup>Rh(π-allyl)(OAc) complex **VIII** (Figure 4c). Complexes **VI**, **VII** and **VIII** were characterized by <sup>1</sup>H and <sup>13</sup>C NMR spectroscopy and **VII** and **VIII** were further characterized by single crystal X-ray diffractions (Figures S5 and S6). The isolation of complexes **VII** and **VIII** unambiguously rules out the possibility that allylic C-N or C-O bond formation by reductive elimination from these Rh(III) species is possible under the catalytic conditions (Figures S5 and S6). Furthermore, the fact that no allylic amine or allylic acetate product was observed during the synthesis of complexes suggests that outer-sphere nucleophilic attack of these nucleophiles on cationic Rh(III)(π-allyl) complexes is also not a plausible explanation for product formation in the catalytic reaction.

This conclusion is further supported by the observation that when cationic complex **VI** was reacted with benzylcarbamate at 40°C for 14h that did not yield allylic amine. Instead, Cp<sup>\*</sup>Rh(π-allyl)Cl complex **V** was recovered in 92% yield after a chloride quench (Figure 5a). To investigate the potential for an oxidatively induced reductive elimination mechanism to be operating, we exposed both Cp<sup>\*</sup>Rh(π-allyl)(NHTs) complex **VII** and Cp<sup>\*</sup>Rh(π-allyl)(OAc) complex **VIII** to two equivalents AgSbF<sub>6</sub>. In the reaction of Cp<sup>\*</sup>Rh(π-allyl)(NHTs) complex **VII**, two equivalents of benzensulfonamide were included that allows us to probe both an oxidatively induced inner-sphere reductive elimination, and an oxidatively induced outer-sphere nucleophilic attack. In this reaction, only 10% combined yield of allylic amine products (**6** and **7**) was observed. No rhodium(π-allyl) complexes could be recovered (Figure 5b). In contrast, when the Cp<sup>\*</sup>Rh(π-allyl)(OAc) complex **VIII** was oxidized with two equivalents AgSbF<sub>6</sub>, clean conversion to the allylic acetate product **4** was observed (Figure 5c). These observations suggest that the catalytic allylic amination reactions proceed through an allylic acetate intermediate, obtained by an oxidatively induced reductive elimination mechanism.

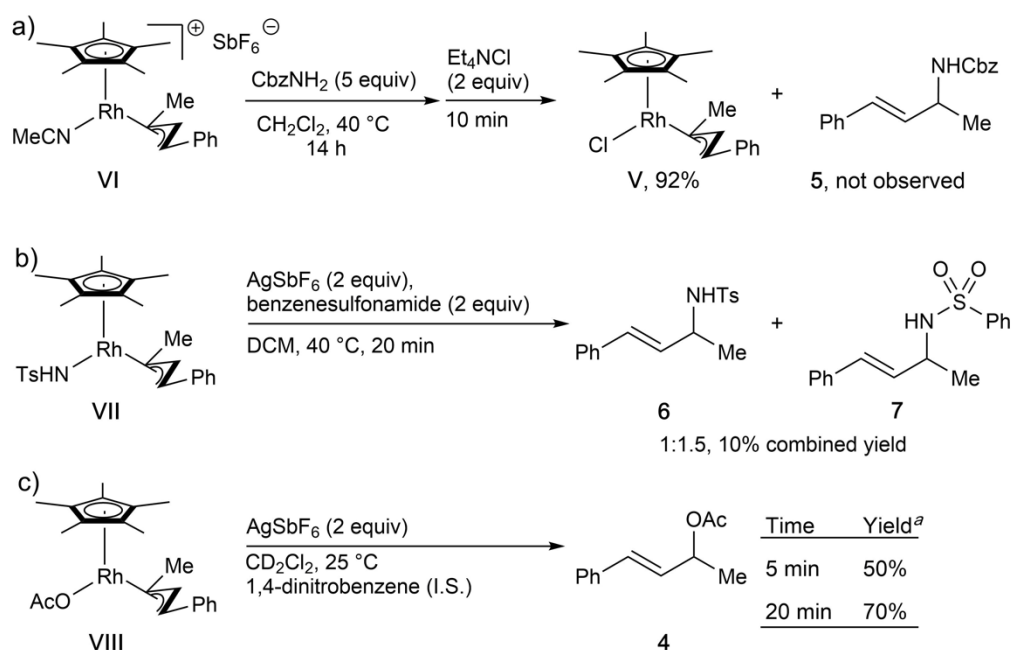


**Figure 5.** Reactivity of Cp<sup>\*</sup>Rh(III)( $\pi$ -allyl) complexes demonstrating the feasibility of oxidatively induced reductive elimination of an allyl acetate. <sup>a</sup>Yields were determined by <sup>1</sup>H NMR analysis of the reaction mixture using 1,4-dinitrobenzene as an internal standard.

To complete our experimental investigation, we demonstrated that allylic acetate **4** is readily converted to the allylic amine **3** in the presence of the Lewis acid components present in the catalytic reactions (Table 1). Both cationic Ag(I) and cationic Rh(III) are able to promote this reaction. In the absence of either silver cation or Cp<sup>\*</sup>Rh, the allylic acetate remained unchanged. These data provide a plausible hypothesis of the pathway toward the completion of the allylic amination catalytic cycle.

**Table 1.** Reactivity of allylic acetate **4** benzyl carbamate **2** in the presence of Ag(I) or Rh(III) as a catalyst.

entry	Catalyst	Yield
1	AgSbF <sub>6</sub>	91%
2	AgBF <sub>4</sub>	76%
3	[Cp <sup>*</sup> RhCl <sub>2</sub> ] <sub>2</sub> /AgSbF <sub>6</sub> <sup>a</sup>	73%
4	[Cp <sup>*</sup> Rh(NCMe) <sub>3</sub> ](SbF <sub>6</sub> ) <sub>2</sub>	84%
5	none	0% <sup>b</sup>

<sup>a</sup>[Cp<sup>\*</sup>RhCl<sub>2</sub>]<sub>2</sub> (25 mM) and AgSbF<sub>6</sub> (40 mM) were stirred in DCM with benzyl carbamate (**2**) at 60 °C for 30 min before allylic acetate **6** was added to be sure that there was no Ag<sup>+</sup> in solution. <sup>b</sup>Allylic amine was not observed by <sup>1</sup>H NMR.

## Computational Investigation of the key steps in the catalytic cycle

Density functional theory (DFT) calculations were carried out to construct a catalytic mechanism incorporating the experimental observations mentioned above. Using 1,3-diphenylpropene **1** as the substrate, we compared the activation barriers of the reductive elimination from the three relevant oxidation states Rh(III), Rh(IV) and Rh(V), as illustrated in Figure 6. The reductive elimination initiated from the Rh(III) intermediate to give Rh(I) is not viable, as the computed activation barrier of 38.4 kcal/mol corresponds to an Eyring rate of  $0.6 \times 10^{-10}$  mol/day at 298 K (Figure 6a). As expected, the oxidation of the metal center to Rh(IV) lowers the activation barrier notably by more than 21 kcal/mol to 17.6 kcal/mol (Figure 6b), which suggests an acceleration of the reaction by more than  $10^{10}$  fold compared to the Rh(III) intermediate. Our calculations suggest that a second oxidation to access the Rh(V) center does not enhance the reaction rate further, as the calculated barrier increases to 19.5 kcal/mol (Figure 6c).

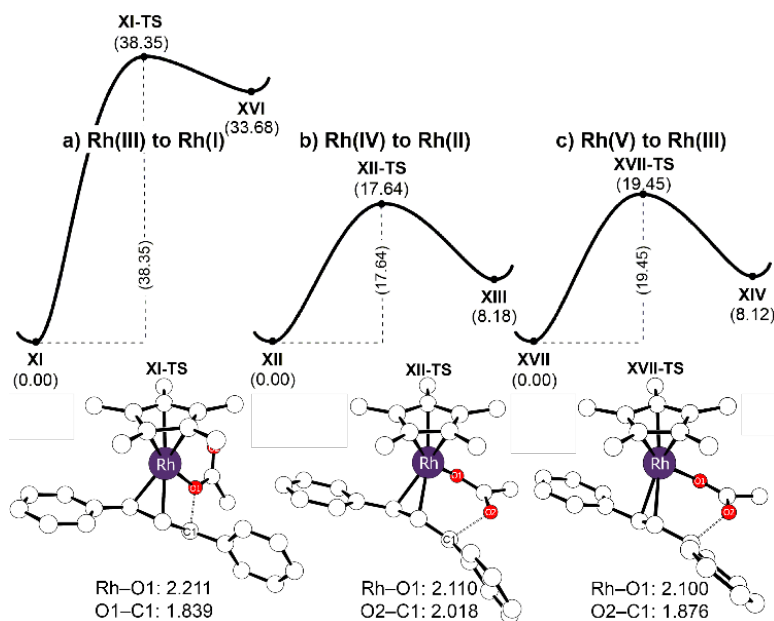


**Figure 6.** Calculated energy profiles for reductive elimination from the a) Rh(III)-, b) Rh(IV)-, and c) Rh(V)- $\pi$ -allyl intermediates, leading to the Rh(I), Rh(II), and Rh(III) products, respectively. The detailed molecular structure of each TS is shown as well. The unit of energy is kcal/mol and of bond length is Å.

A closer inspection of the transition structures reveals that the two oxygen atoms of the acetate introduce a slight variation in the transition states. During the reductive elimination from the Rh(III)-center, the O-C bond is formed by the acetate-oxygen that is directly bound to the metal, as illustrated in Figure 6a. The Rh-O bond elongates from 2.121 to 2.211 Å as the transition state **XI-TS** is traversed with the C-O distance being 1.839 Å. This bond forming event is best conceptualized by considering that the allylic fragment formally donates two electrons to the Rh-center to accomplish the reductive part of the reductive elimination step. Consequently, it becomes a positively polarized electrophile that can engage the acetate and form the C-O bond. Of course, these two processes are concerted in reality, but it is instructive to visualize them separately. When the metal is oxidized

to Rh(IV) or Rh(V), it is the distal oxygen of the acetate that attacks the carbon and the Rh–O bond is mostly maintained with the Rh–O bond lengths being 2.110 (**XII-TS**) and 2.100 Å (**XVII-TS**), respectively, as illustrated in Figures 6b and 6c. Thus, whereas the Rh(III) center carries out a classical reductive elimination, the other higher valent metal centers prefer to reductively couple the acetate with the allyl functionality without eliminating the acetate. This subtle change in mechanism is easy to understand considering that the Rh–O bond becomes much stronger in Rh(IV) and Rh(V) compared to Rh(III). As the acetate acts as a nucleophile in this step, the higher oxidation state at the metal decreases its nucleophilicity and results in a higher barrier in the Rh(V)-complex. Thus, Rh(IV) constitutes an ideal compromise between the two governing forces, namely the ability of the metal center to oxidize the allyl fragment and the nucleophilicity of the acetate.

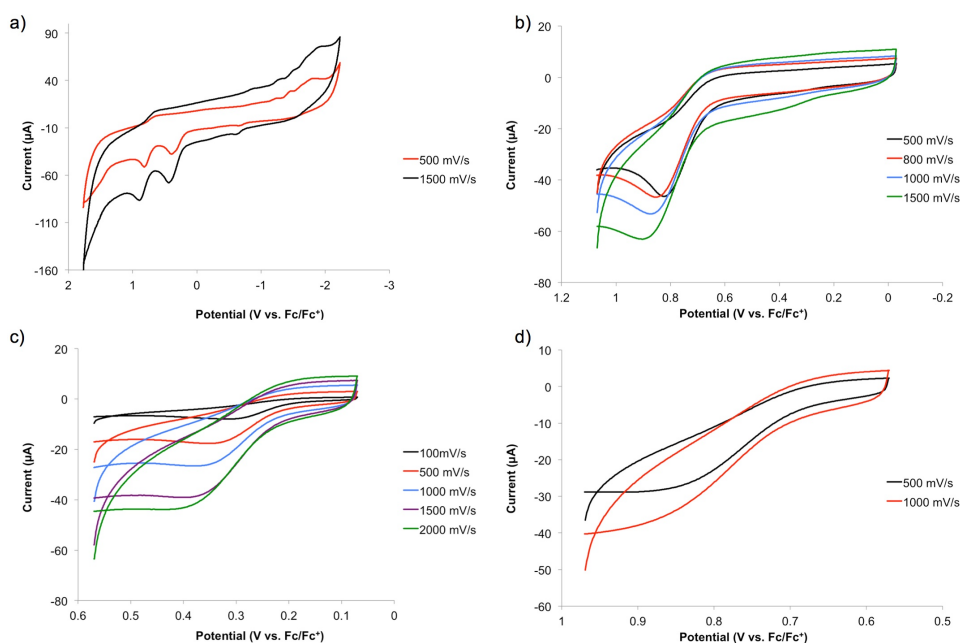
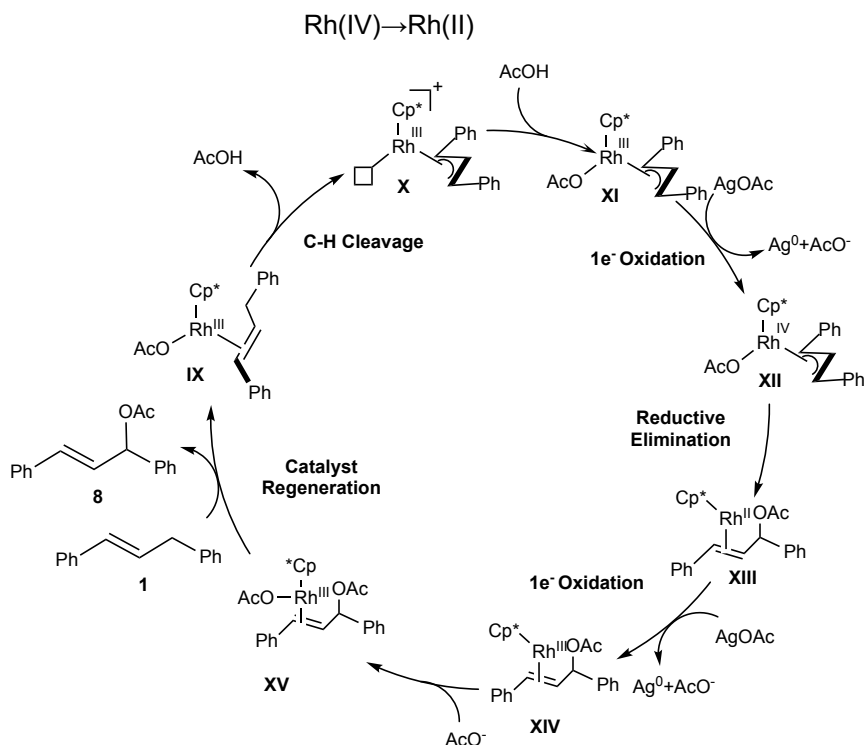


**Figure 7.** Cyclic voltammograms of rhodium acetate complex **VIII**. Voltammograms recorded in  $\text{CH}_2\text{Cl}_2$  with 0.1 M TBAPF<sub>6</sub> as the supporting electrolyte.

To test the proposed catalytic mechanism, cyclic voltammetry experiments were carried out. Complex **VIII** showed two irreversible oxidation waves, suggesting that both Rh(IV) and Rh(V) are accessible on an electrochemical time scale (Figures 7a and 7b). As is expected for an electrochemical step that is coupled with a chemical event, the peak position of both steps are scan rate dependent (Figures 7c and 7d). The first oxidation occurs at  $E_p = \sim 0.42$  V versus Fc/Fc<sup>+</sup> which we assign to the Rh(III)/(IV) couple, and the second event occurs at  $E_p = \sim 0.85$  V that is attributed to the Rh(IV)/(V) couple. Importantly, even at fast scan rates of 2,000 mV/s the Rh(III)/(IV) redox event is irreversible suggesting that reductive elimination from Rh(IV) is fast (Figure 7c). Given that the redox potential of Ag<sup>+</sup> in  $\text{CH}_2\text{Cl}_2$  is 0.65 V, it is unlikely that the Rh(V) complex can be accessed via chemical oxidation. Taken together, these data support a catalytic cycle that consists of the sequence Rh(III) → Rh(IV) → Rh(II) → Rh(III).

Scheme 2 summarizes the proposed mechanism of the Rh catalyzed allylic acetylation and the corresponding reaction energy profile is shown in Figure 8. The catalytic cycle begins with the coordination of the acetate and the olefin substrates **1** to the Cp<sup>\*</sup>Rh fragment to form the initial reactant complex **IX**, which undergoes a concerted metalation deprotonation (CMD) traversing the transition **VI-TS** to activate the allylic C–H bond. The computed activation energy for this step is 26.7 kcal/mol, which is in good agreement with the experimental observation that a mildly elevated temperature is required to prepare the acetylated intermediate **XIII** (*vide supra*). Ligand exchange affords the Cp<sup>\*</sup>Rh(III)( $\pi$ -allyl)OAc complex **XI**. As discussed above, reductive elimination from this intermediate is associated with a very high barrier (Figure 6a). To push the reaction forward, one electron oxidation of Rh(III) to Rh(IV) is needed which enables the reductive elimination via **XIV-TS** with a computed barrier of 17.6 kcal/mol. Intermediate **XIII** can easily undergo an one-electron oxidation to form the Rh(III) intermediate **XIV**, which releases product **4** via ligand exchange steps.

**Scheme 2.** Proposed catalytic mechanism of the rhodium catalyzed allylic acetylation going through



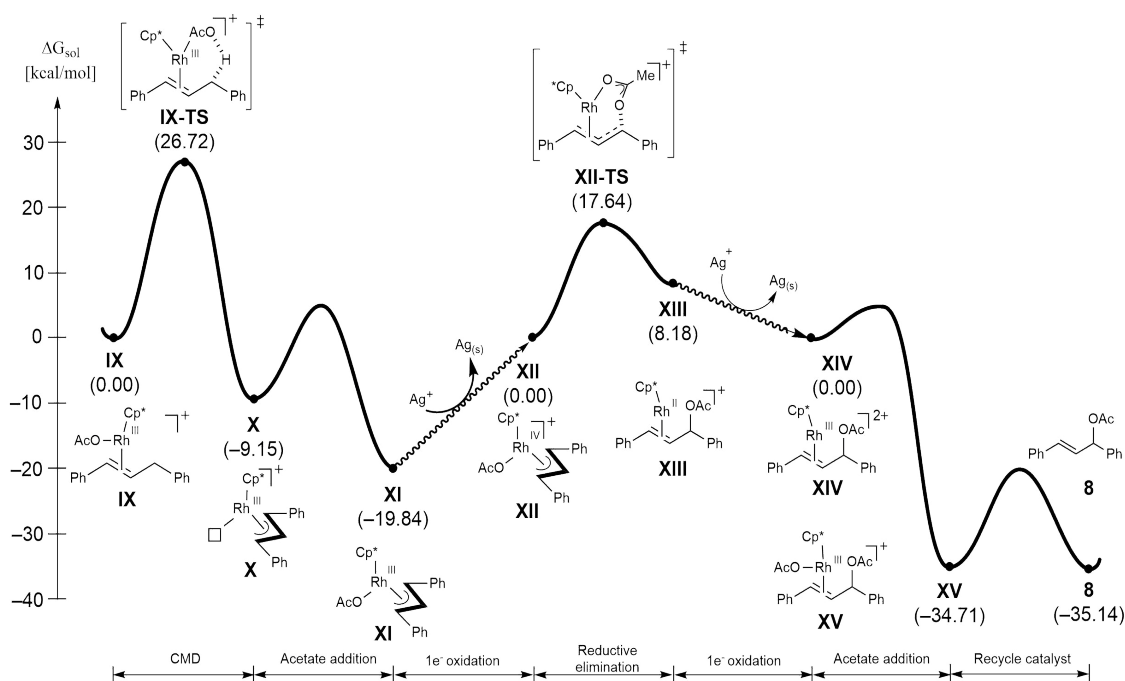
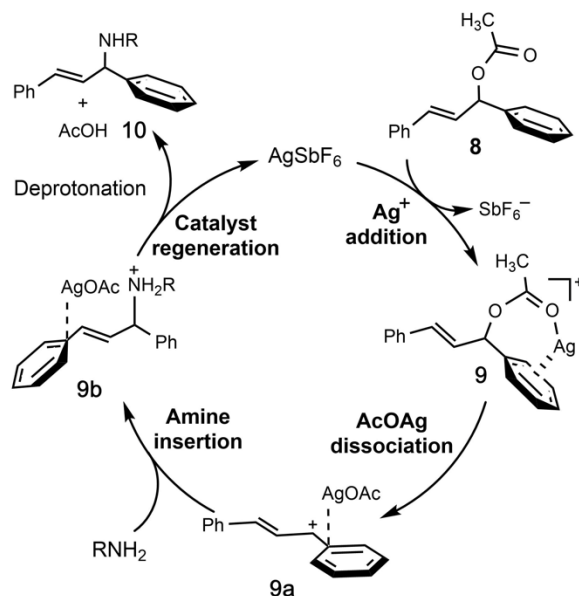


**Figure 8.** Energy profile for Rh-catalyzed allylic acetylation going through Rh (IV $\rightarrow$ II)

**Formation of Allylic Amines** With the detailed mechanism of the intermediate allylic acetate formation in hand, we turned our attention to the role of the silver and rhodium salts in the conversion of the allylic acetate to the allylic amine product, seeking to differentiate between simple Lewis acid promoted nucleophilic substitution or a more complicated allylic substitution proceeding through additional  $\pi$ -allyl complexes. In the following, we delineate the mechanistic details of the two possible mechanistic hypotheses for the formation of allylic amine product from the allylic acetate intermediate, by means of DFT calculations.

**Scheme 3.** Proposed mechanism for  $\text{AgSbF}_6$  catalyzed allylic C–H amination from allylic acetate





Inspired by the related  $\text{AgSbF}_6$  catalyzed amination of allylic acetate,<sup>12</sup> we compiled a plausible mechanistic pathway for the amination reaction which involves an initial  $\text{Ag}^+$  addition to allylic acetate to prepare a silver coordinated allylic acetate complex, as illustrated in Scheme 3. The energy profile for the allylic amination of allylic acetate **8** catalyzed by  $\text{Ag}^+$  is depicted in Figure 9. The catalytic cycle is initiated by the addition of  $\text{Ag}^+$  to allylic acetate intermediate yielding **9**. Out of the three possible scenarios of the nucleophilic substitutions ( $\text{S}_{\text{N}}1$ ,  $\text{S}_{\text{N}}2$ , and  $\text{S}_{\text{N}}2'$ ), our DFT calculations suggested that the  $\text{S}_{\text{N}}1$  mechanism is the most plausible route for the nucleophilic substitution. The dissociation of  $\text{AgOAc}$ , facilitated by  $\text{Ag}^+$  as a Lewis acid, yields an allylic cation intermediate **9a**, associated with an activation barrier of 14.4 kcal/mol (**9-TS**). The addition of nucleophile (**9a-TS**) requires 16.7 kcal/mol of activation energy, which is predicted to be the most difficult step to activate of the amination reaction, yet is viable under the reaction condition used. In comparison, the  $\text{S}_{\text{N}}2$  and  $\text{S}_{\text{N}}2'$  reactions are much more difficult to activate with the calculated activation barriers being 23.0 and 27.6 kcal/mol, respectively. To push the reaction forward, the aminated intermediate **9b** undergoes a concerted deprotonation via traversing the transition structure **9b-TS** to produce the allylic amine product bound to a silver cation **9c**.

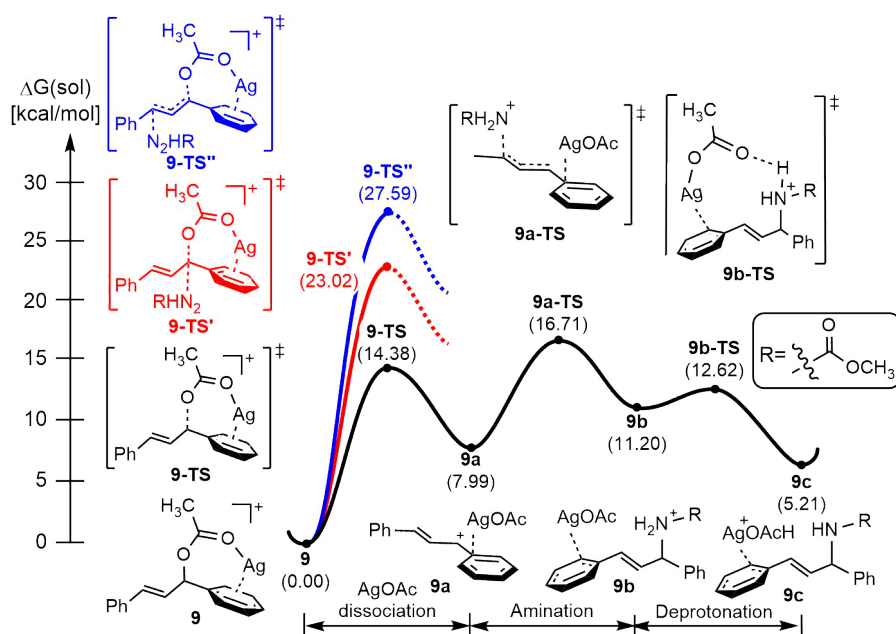
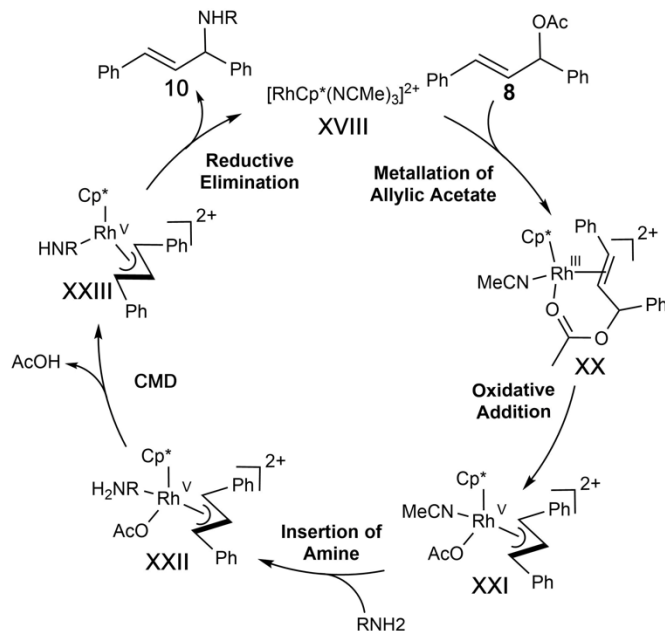


**Figure 9.** Energy profile for  $\text{AgSbF}_6$  catalyzed allylic C–H amination from allylic acetate

**Scheme 4.** Proposed mechanism of the inner-sphere Rh-catalyzed allylic C–H amination from allylic acetate



The catalytic cycle for a  $\text{Cp}^*\text{Rh}$  catalyzed allylic amination of allylic acetate via the inner-sphere mechanism is depicted schematically in Scheme 4. A complete energy profile of the inner-sphere amination is depicted in Figure 10. To reduce the computational cost, we simplified the amine source to methylcarbamate. Commencing from the active catalyst XVIII, an intermediate XIX is formed through coordination of the allylic double bond, that is 12.8 kcal/mol uphill in energy. A ligand exchange step follows to allow the acetate of the substrate to coordinate the metal center to form XX, that is found at 9.5 kcal/mol higher in energy from that of the active catalyst. Subsequent oxidative addition of acetate takes place to yield an intermediate XXI that is 15.9 kcal/mol uphill in energy, via traversing the transition state XX-TS with an activation barrier of 22.8 kcal/mol. After the addition of acetate, a ligand exchange step follows to replace a coordinating acetonitrile with the amine ligand (XXII). The amine ligand undergoes a concerted metalation and deprotonation step (CMD) with the removal of an acetic acid molecule via a transition structure (XXII-TS) with the activation barrier of 26.2 kcal/mol, to find an intermediate XXIII that is 20.1 kcal/mol uphill in energy. In the next step, Rh(V) complex undergoes the reductive elimination from Rh(V)→Rh(III) to construct a new C–N bond via traversing a transition structure XXIII-TS with an activation energy barrier of 27.3 kcal/mol. The reductive elimination is the most difficult step to activate throughout the inner-sphere amination pathway. The computed activation energy barrier is moderately high yet is predicted to be viable under the reaction conditions used in some of the catalytic amination reactions (60°C), as the computed Eyring rate of the activation is 0.2 mol/day at 60°C. Upon completion of the reductive elimination, ligand exchanges steps follow to yield the aminated product 10 and to regenerate the catalyst XXIII. We also investigated the nucleophilic substitution of acetate by amine via the outer-sphere mechanism (Scheme S4 and Figure S10), and found a computed activation energy barrier for the amination of 41.0 kcal/mol, precluding this mechanism under the reaction conditions used.

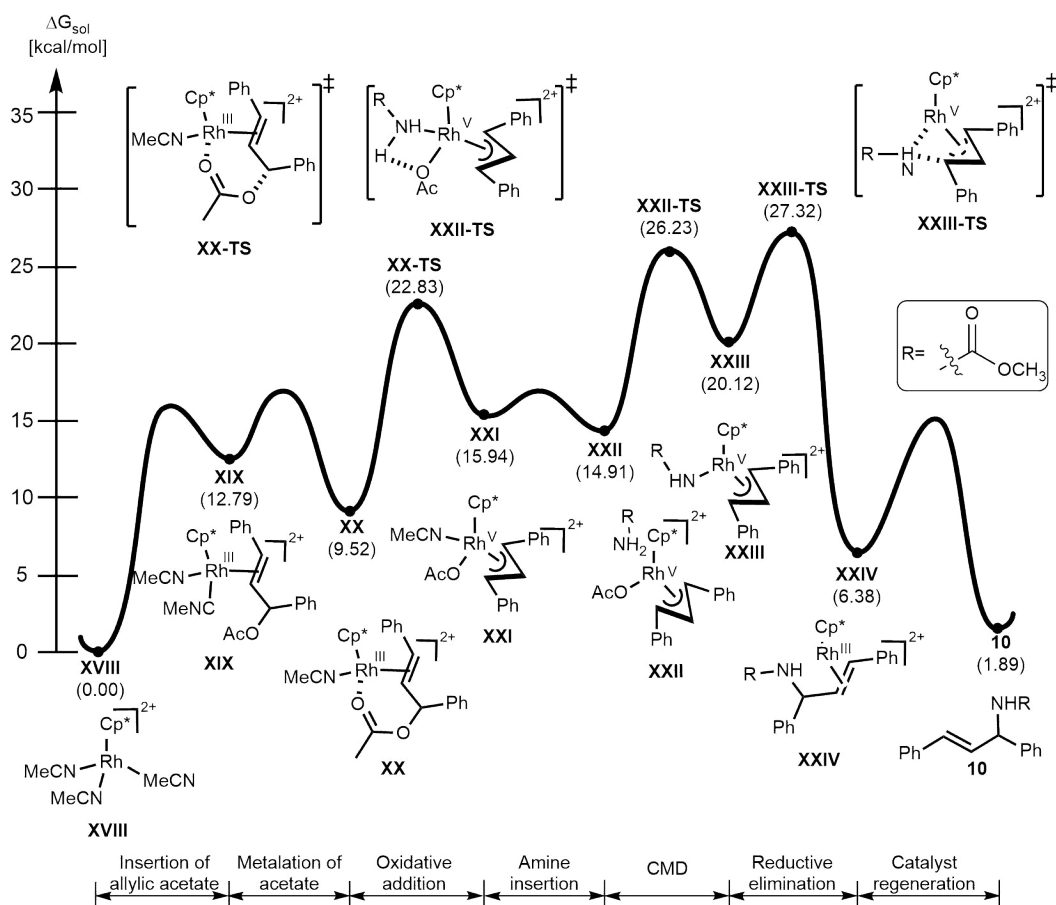


**Figure 10.** energy profile of the inner-sphere Rh-catalyzed amination of allylic acetate **4**

## CONCLUSIONS

The computational and experimental data provided a detailed picture of the rhodium-catalyzed  $\text{C}(\text{sp}^3)\text{-H}$  allylic amination. Overall, the rate-determining step of the entire catalytic cycles examined computationally was found to be the C–H activation of allylic substrate with a DFT-computed barrier of 26.8 kcal/mol. This is consistent with the experimental kinetic observations that also support C–H activation as the rate determining step in this transformation. Calculations revealed that the Rh catalyst facilitates the formation of the allylic acetate using the silver salt as an oxidizing agent via an oxidatively induced reductive elimination reaction<sup>11</sup> where the Rh(III) center of the key intermediate is first oxidized to Rh(IV). Interestingly, the two-electron oxidation to possibly access the Rh(V) analogue is not found to be helpful and we found good experimental evidence that Rh(IV) is indeed the catalytically competent species. Further experimental studies as well as DFT calculations suggested that the amination of the allylic acetate intermediate proceeds by an  $\text{S}_{\text{N}}1$  ligand exchange mechanism mediated by silver acting as a Lewis acid catalyst. Although a  $\text{Cp}^*\text{Rh}$  catalyzed pathway was calculated to be feasible under the reaction conditions, the barriers were significantly higher than those calculated for the silver promoted pathway, and are unlikely to contribute significantly to product formation. We note that this study provides insights that are likely applicable to the related rhodium catalyzed allylic etherification and arylation reactions that were recently disclosed,<sup>13</sup> but likely do not explain the allylic arylation reaction utilizing aryl boronic acids,<sup>14</sup> or the allylic amidation

processes using dioxazolone reagents.<sup>15</sup> Further studies to provide a unified mechanistic picture of this emergent field are required.

### Computational details

All calculations were constructed using computer models based on density functional theory (DFT)<sup>16</sup> implemented in the Jaguar 9.1 suite<sup>17</sup> of ab initio quantum chemistry programs. Geometry optimizations were performed using the B3LYP<sup>18</sup> functional including Grimme's D3 dispersion correction<sup>19</sup> and the 6-31G(d,p) basis set, where rhodium was represented with the Los Alamos LACVP basis set,<sup>20</sup> which incorporates effective core potentials that describes the relativistic effects (B3LYP-D3/LACVP). Upon completion of the geometry optimizations, single point SCF electronic energies of the optimized geometries were calculated using Dunning's correlation consistent triple- $\zeta$  basis set (cc-pVTZ(-f))<sup>21</sup> that includes a double set of the polarization functions. For rhodium, a modified version of LACVP, designed as LACV3P is used to match the effective core potential with triple- $\zeta$  quality was used for the single point SCF calculations (B3LYP-D3/cc-pVTZ(-f)/LACV3P). Solvation energies were evaluated using the self-consistent reaction field (SCRF)<sup>22</sup> approach based on the accurate numerical solutions of the Poisson-Boltzmann equation. For the solvation calculations, 6-31G(d,p)/LACVP basis at the optimized gas-phase geometries were used with the solvent dielectric constant of  $\epsilon = 9.08$  for the solvent medium considered (1,2-dichloroethane). It is noted that the solvation energies are contingent on the empirical parameterization of atomic radii used to generate the solute surface, wherein we used the standard set of optimized radii for H (1.150 Å), C (1.900 Å), N (1.600 Å), O (1.550 Å), Ag (1.574 Å), Sb (2.210 Å), F (1.682 Å), and Rh (1.464 Å) that are employed in the Jaguar 9.1 suite.<sup>23</sup> To confirm the proper convergence to well-defined minima (intermediates and products) or saddle points (transition structures) on the potential energy surface, vibrational frequencies based on harmonic approximation were computed with the 6-31G\*\*/LACVP basis set. The energy components were calculated by adopting the protocol given below (eqs 2–6):

$$G(\text{Sol}) = G(\text{gas}) + G(\text{solv}) \quad (2)$$

$$G(\text{gas}) = H(\text{gas}) - TS(\text{gas}) \quad (3)$$

$$H(\text{gas}) = E(\text{SCF}) + \text{ZPE} \quad (4)$$

$$\Delta E(\text{SCF}) = \Sigma E(\text{SCF}) \text{ for products} - \Sigma E(\text{SCF}) \text{ for reactants} \quad (5)$$

$$\Delta G(\text{sol}) = \Sigma G(\text{sol}) \text{ for products} - \Sigma G(\text{sol}) \text{ for reactants} \quad (6)$$

,  $G(\text{sol})$  is the Gibbs free energy in solution phase,  $G(\text{gas})$  is the Gibbs free energy in gas phase,  $G(\text{solv})$  is the free energy of solvation,  $H(\text{gas})$  is the enthalpy in gas phase,  $T$  is the temperature (298.15 K),  $S(\text{gas})$  is the entropy in gas phase, ZPE is the zero point energy, and  $E(\text{SCF})$  is the self-consistent electronic field energy calculated by the SCF procedure.<sup>24</sup>

## ASSOCIATED CONTENT

### Supporting Information

## Author Information

### Corresponding Author

\*E-mail: mbaik2805@kaist.ac.kr

\*E-mail: sblakey@emory.edu

### ORCID

Mu-Hyun Baik: 0000-0002-8832-8187

Simon B. Blakey: 0000-0002-4100-8610

Jiyong Park: 0000-0002-3225-4510

Cora E. MacBeth: 0000-0003-3877-2236

Jaohn Bacsa: 0000-0001-5681-4458

### Notes

The authors declare no competing financial interest.

## ACKNOWLEDGMENT

The research was supported in part by the Institute for Basic Science (IBS-R010-DI) in Korea and by the National Science Foundation (NSF) under the CCI Center for Selective C-H Functionalization (CHE-1700982). NMR studies for this research were performed on instrumentation funded by the NSF (CHE-1531620). The X-ray analysis was done by the Emory X-ray Crystallography Facility using the Rigaku Synergy-S diffractometer, supported by the NSF (CHE-1626172).

## REFERENCES

- (a) Wang, N.-X.; Xing, Y.; Zhang, W., Advances in Transition-Metal-Catalyzed Direct sp<sup>3</sup>-Carbon–Hydrogen Bond Functionalization. *Synlett* **2015**, 26 (15), 2088-2098.(b) Yang, X.; Shan, G.; Wang, L.; Rao, Y., Recent advances in transition metal (Pd, Ni)-catalyzed C(sp<sup>3</sup>) H bond activation with bidentate directing groups. *Tetrahedron Lett.* **2016**, 57 (8), 819-836.(c) Saint-Denis, T. G.; Zhu, R.-Y.; Chen, G.; Wu, Q.-F.; Yu, J.-Q., Enantioselective C(sp<sup>3</sup>)–H bond activation by chiral transition metal catalysts. *Science* **2018**, 359 (6377).(d) Chu, J. C. K.; Rovis, T., Complementary Strategies for Directed C(sp<sup>3</sup>)–H Functionalization: A Comparison of Transition-Metal-Catalyzed Activation, Hydrogen Atom Transfer, and Carbene/Nitrene Transfer. *Angew. Chem. Int. Ed Engl.* **2018**, 57 (1), 62-101.
- Li, C.-J., Cross-Dehydrogenative Coupling (CDC): Exploring C–C Bond Formations beyond Functional Group Transformations. *Acc. Chem. Res.* **2009**, 42 (2), 335-344.
- Chen, M. S.; Whilte, M. C., A Sulfoxide-Promoted, Catalytic Method for the Regioselective Synthesis of Allylic Acetates from Monosubstituted Olefins via C–H Oxidation. *J. Am. Chem. Soc.* **2004**, 126 (5), 1346-1347.
- (a) Young, A. J.; White, M. C., Catalytic Intermolecular Allylic C-H Alkylation. *J. Am. Chem. Soc.* **2008**, 130 (43), 14090-14091.(b) Reed, S. A.; White, M. C., Catalytic Intermolecular Linear Allylic C–H Amination via Heterobimetallic Catalysis. *J. Am. Chem. Soc.* **2008**, 130 (11), 3316-3318.(c) Reed, S. A.; Mazzotti, A. R.; White,

- M. C., A Catalytic, Brønsted Base Strategy for Intermolecular Allylic C–H Amination. *J. Am. Chem. Soc.* **2009**, *131* (33), 11701-11706.(d) Pattillo, C. C.; Strambeanu, I. I.; Calleja, P.; Vermeulen, N. A.; Mizuno, T.; White, M. C., Aerobic Linear Allylic C–H Amination: Overcoming Benzoquinone Inhibition. *J. Am. Chem. Soc.* **2016**, *138* (4), 1265-1272.(e) Ma, R.; White, M. C., C–H to C–N Cross-Coupling of Sulfonamides with Olefins. *J. Am. Chem. Soc.* **2018**, *140* (9), 3202-3205.(f) Fraunhoffer, K. J.; White, M. C., syn-1,2-Amino Alcohols via Diastereoselective Allylic C–H Amination. *J. Am. Chem. Soc.* **2007**, *129* (23), 7274-7276.(g) Chen, M. S.; Prabakaran, N.; Labenz, N. A.; White, M. C., Serial Ligand Catalysis: A Highly Selective Allylic C–H Oxidation. *J. Am. Chem. Soc.* **2005**, *127* (19), 6970-6971.(h) Campbell, A. N.; White, P. B.; Guzei, I. A.; Stahl, S. S., Allylic C–H Acetoxylation with a 4,5-Diazafluorenone-Ligated Palladium Catalyst: A Ligand-Based Strategy To Achieve Aerobic Catalytic Turnover. *J. Am. Chem. Soc.* **2010**, *132* (43), 15116-15119.
5. Cochet, T.; Bellosta, V.; Roche, D.; Ortholand, J.-Y.; Greiner, A.; Cossy, J., Rhodium(iii)-catalyzed allylic C–H bond amination. Synthesis of cyclic amines from  $\omega$ -unsaturated N-sulfonylamines. *Chem. Commun.* **2012**, 48 (87), 10745.
  6. Burman, J. S.; Blakey, S. B., Regioselective Intermolecular Allylic C–H Amination of Disubstituted Olefins via Rhodium/ $\pi$ -Allyl Intermediates. *Angew. Chem. Int. Ed Engl.* **2017**, *129* (44), 13854-13857.
  7. (a) Leahy, D. K.; Evans, P. A., Rhodium(I)-Catalyzed Allylic Substitution Reactions and Their Applications to Target Directed Synthesis. *ChemInform* **2005**, *36* (33).(b) Evans, P. A.; Nelson, J. D., Conservation of Absolute Configuration in the Acyclic Rhodium-Catalyzed Allylic Alkylation Reaction: Evidence for an Enyl( $\sigma$ - $\pi$ ) Organorhodium Intermediate. *J. Am. Chem. Soc.* **1998**, *120* (22), 5581-5582.
  8. (a) Satoh, T.; Miura, M., Oxidative coupling of aromatic substrates with alkynes and alkenes under rhodium catalysis. *Chemistry* **2010**, *16* (37), 11212-11222.(b) *Issues in Chemistry and General Chemical Research: 2011 Edition*. ScholarlyEditions: 2012; p 6580.
  9. (a) Vásquez-Céspedes, S.; Wang, X.; Glorius, F., Plausible Rh(V) Intermediates in Catalytic C–H Activation Reactions. *ACS Catal.* **2017**, *8* (1), 242-257.(b) Li, L.; Brennessel, W. W.; Jones, W. D., An Efficient Low-Temperature Route to Polycyclic Isoquinoline Salt Synthesis via C–H Activation with  $[\text{Cp}^*\text{MCl}_2]_2$  (M = Rh, Ir). *J. Am. Chem. Soc.* **2008**, *130* (37), 12414-12419.
  10. (a) Periana, R. A.; Bergman, R. G., Rapid intramolecular rearrangement of a hydrido(cyclopropyl)rhodium complex to a rhodacyclobutane. Independent synthesis of the metallacycle by addition of hydride to the central carbon atom of a cationic rhodium  $\pi$ -allyl complex. *J. Am. Chem. Soc.* **1984**, *106* (23), 7272-7273.(b) Wakefield, J. B.; Stryker, J. M., Metallacyclobutanes from kinetic nucleophilic addition to  $\eta^3$ -allyl ethylene complexes of iridium. Regioselectivity dependence on nucleophile and allyl orientation. *J. Am. Chem. Soc.* **1991**, *113* (18), 7057-7059.(c) Shibata, Y.; Kudo, E.; Sugiyama, H.; Uekusa, H.; Tanaka, K., Facile Generation and Isolation of  $\pi$ -Allyl Complexes from Aliphatic Alkenes and an Electron-Deficient Rh(III) Complex: Key Intermediates of Allylic C–H Functionalization. *Organometallics* **2016**, *35* (10), 1547-1552.
  11. Shin, K.; Park, Y.; Baik, M.-H.; Chang, S., Iridium-catalysed arylation of C–H bonds enabled by oxidatively induced reductive elimination. *Nat. Chem.* **2017**, *10*, 218.
  12. Dagar, A.; Guin, S.; Samanta, S., AgSbF<sub>6</sub>-Catalyzed Tandem Reaction of 2-Alkynylanilines with Cyclic Enynones: Efficient access to 3-Furo[3,2-c]chromenylindoles and Related Scaffolds. *Asian J. Org. Chem.* **2017**, *7* (1), 123-127.
  13. (a) Nelson, T. A. F.; Blakey, S. B., Intermolecular Allylic C–H Etherification of Internal Olefins. *Angew. Chem. Int. Ed Engl.* **2018**, *130* (45), 15127-15131.(b) Lerchen, A.; Knecht, T.; Koy, M.; Ernst, J. B.; Bergander, K.; Daniliuc, C. G.; Glorius, F., Non-Directed Cross-Dehydrogenative (Hetero) arylation of Allylic C (sp<sup>3</sup>)-H bonds enabled by C–H Activation. *Angew. Chem. Int. Ed.* **2018**, *57* (46), 15248-15252.
  14. Knecht, T.; Pinkert, T.; Dalton, T.; Lerchen, A.; Glorius, F., Cp\*Rh<sup>III</sup>-Catalyzed Allyl–Aryl Coupling of Olefins and Arylboron Reagents Enabled by C(sp<sup>3</sup>)-H Activation. *ACS Catal.* **2019**, *9* (2), 1253-1257.
  15. (a) Lei, H.; Rovis, T., Ir-Catalyzed Intermolecular Branch-Selective Allylic C–H Amidation of Unactivated Terminal Olefins. *J. Am. Chem. Soc.* **2019**, *141* (6), 2268-2273.(b) Knecht, T.; Mondal, S.; Ye, J.-H.; Das, M.; Glorius, F., Intermolecular, Branch-Selective, and Redox-Neutral Cp\*Ir<sup>III</sup>-Catalyzed Allylic C–H Amidation. *Angew. Chem. Int. Ed Engl.* **2019**, *58* (21), 7117-7121.(c) Burman, J. S.; Harris, R. J.; B. Farr, C. M.; Bacsá, J.; Blakey, S. B., Rh(III) and Ir(III)Cp\* Complexes Provide Complementary Regioselectivity Profiles in Intermolecular Allylic C–H Amidation Reactions. *ACS Catal.* **2019**, 5474-5479.
  16. Parr, R. G.; Yang, W., *Density-Functional Theory of Atoms and Molecules*. Oxford University Press: 1994.
  17. Bochevarov, A. D.; Harder, E.; Hughes, T. F.; Greenwood, J. R.; Braden, D. A.; Philipp, D. M.; Rinaldo, D.; Halls, M. D.; Zhang, J.; Friesner, R. A., Jaguar: A high-performance quantum chemistry software program with strengths in life and materials sciences. *Int. J. Quantum Chem.* **2013**, *113* (18), 2110-2142.
  18. (a) Becke, A. D., Density-Functional Thermochemistry 3. The Role of Exact Exchange. *J. Chem. Phys.* **1993**, *98* (7), 5648-5652.(b) Lee, C.; Yang, W.; Parr, R. G., Development of the Colle-Salvetti correlation-energy formula into a functional of the electron-density. *Phys. Rev. B* **1988**, *37* (2), 785-789.

19. Grimme, S.; Antony, J.; Ehrlich, S.; Krieg, H., A consistent and accurate ab initio parametrization of density functional dispersion correction (DFT-D) for the 94 elements H-Pu. *J. Chem. Phys.* **2010**, *132* (15).
20. (a) Hay, P. J.; Jeffrey Hay, P.; Wadt, W. R., Ab initio effective core potentials for molecular calculations. Potentials for K to Au including the outermost core orbitals. *J. Chem. Phys.* **1985**, *82* (1), 299-310.(b) Wadt, W. R.; Jeffrey Hay, P., Ab initio effective core potentials for molecular calculations. Potentials for main group elements Na to Bi. *J. Chem. Phys.* **1985**, *82* (1), 284-298.(c) Hay, P. J.; Jeffrey Hay, P.; Wadt, W. R., Ab initio effective core potentials for molecular calculations. Potentials for the transition metal atoms Sc to Hg. *J. Chem. Phys.* **1985**, *82* (1), 270-283.
21. Dunning, T. H., Gaussian basis sets for use in correlated molecular calculations. I. The atoms boron through neon and hydrogen. *J. Chem. Phys.* **1989**, *90* (2), 1007-1023.
22. (a) Friedrichs, M.; Zhou, R.; Edinger, S. R.; Friesner, R. A., Poisson-Boltzmann Analytical Gradients for Molecular Modeling Calculations. *J. Phys. Chem. B* **1999**, *103* (16), 3057-3061.(b) Marten, B.; Kim, K.; Cortis, C.; Friesner, R. A.; Murphy, R. B.; Ringnalda, M. N.; Sitkoff, D.; Honig, B., New Model for Calculation of Solvation Free Energies: Correction of Self-Consistent Reaction Field Continuum Dielectric Theory for Short-Range Hydrogen-Bonding Effects. *J. Phys. Chem.* **1996**, *100* (28), 11775-11788.(c) Edinger, S. R.; Cortis, C.; Shenkin, P. S.; Friesner, R. A., Solvation Free Energies of Peptides: Comparison of Approximate Continuum Solvation Models with Accurate Solution of the Poisson-Boltzmann Equation. *J. Phys. Chem. B* **1997**, *101* (7), 1190-1197.
23. Rashin, A. A.; Honig, B., Reevaluation of the Born model of ion hydration. *J. Phys. Chem.* **1985**, *89* (26), 5588-5593.
24. Ryu, H.; Park, J.; Kim, H. K.; Park, J. Y.; Kim, S.-T.; Baik, M.-H., Pitfalls in Computational Modeling of Chemical Reactions and How To Avoid Them. *Organometallics* **2018**, *37* (19), 3228-3239.

Blakey-Baik-Rh-AllylicCHAmination-Mechanism.pdf (3.16 MiB)

[view on ChemRxiv](#) • [download file](#)

---



# The Mechanism of Rhodium Catalyzed Allylic C–H Amination

Robert J. Harris,<sup>†</sup> Jiyong Park<sup>\*,§</sup>, Taylor A. F. Nelson,<sup>†</sup> Nafees Iqbal,<sup>\*,§</sup> Daniel C. Salgueiro,<sup>†</sup> John Bacsá,<sup>†</sup> Cora E. MacBeth,<sup>†</sup> Mu-Hyun Baik<sup>\*,§,‡</sup> and Simon B. Blakey<sup>\*,†</sup>

<sup>†</sup>Department of Chemistry, Emory University, Atlanta, GA, 30322, U.S.A.

<sup>‡</sup>Department of Chemistry, Korea Advanced Institute of Science and Technology (KAIST), Daejeon 34141, Republic of Korea

<sup>§</sup>Center for Catalytic Hydrocarbon Functionalizations, Institute for Basic Science (IBS), Daejeon 34141, Republic of Korea

## ABSTRACT

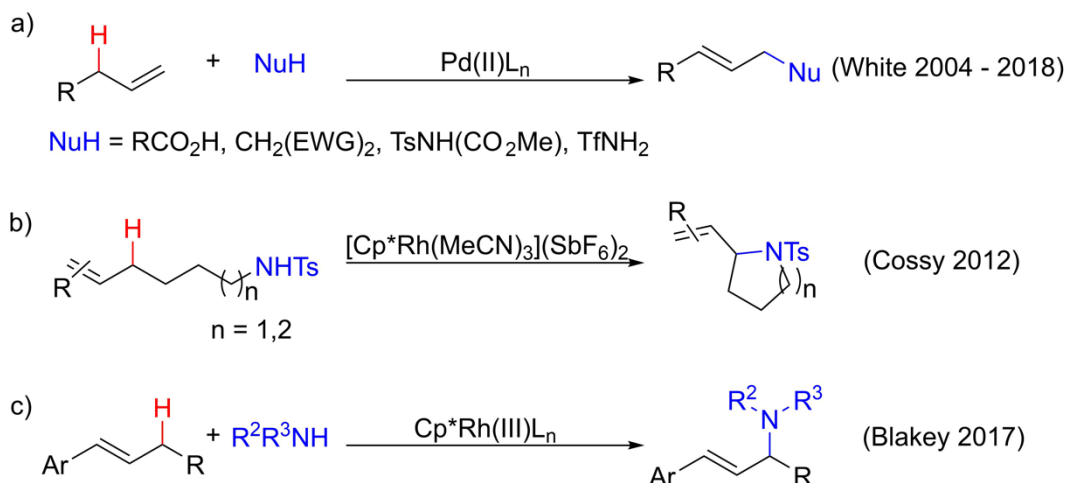
The mechanism of catalytic allylic C–H amination reactions promoted by Cp\*Rh complexes is reported. Reaction kinetics experiments, stoichiometric studies, and DFT calculations demonstrate that allylic C–H activation to generate a Cp\*Rh( $\pi$ -allyl) complex is viable under mild reaction conditions. The role of external oxidant in the catalytic cycle is elucidated. Quantum mechanical calculations, stoichiometric reactions, and cyclic voltammetry experiments support an oxidatively induced reductive elimination process of the allyl fragment with an acetate ligand. Lastly, evidences supporting the amination of an allylic acetate intermediate is presented. Both nucleophilic substitution catalyzed by Ag<sup>+</sup> that behaves as a Lewis acid catalyst and an inner-sphere amination catalyzed by Cp\*Rh are shown to be viable for the last step of the allylic amination reaction.

**Keywords:** Density Functional Theory, C–H amination, Rhodium, Allylic functionalization, Mechanism

## INTRODUCTION

Transition-metal-mediated direct activation of C(sp<sup>3</sup>)-H bonds to install C-X (X = C, N, and O) functionalities has become an indispensable method in modern synthetic strategy. Precisely controlling the regio- and diastereo-selectivities in these reactions is a key challenge that has been achieved using directing groups<sup>1</sup> or by taking advantage of the inherent reactivities of the C-H bonds.<sup>2</sup> Direct and efficient synthetic protocols that afford desired selectivities continue to be actively sought after. In 2004, White and co-workers reported the catalytic allylic C-H acetoxylation of terminal olefins in complex settings catalyzed by palladium.<sup>3</sup> In a series of reports that followed, Pd( $\pi$ -allyl) intermediates were intercepted with a variety of stabilized carbon, nitrogen, and oxygen nucleophiles (Scheme 1a).<sup>4</sup> Cossy and co-workers subsequently reported the use of Cp\*Rh to catalyze the intramolecular cyclization of aminoalkenes by allylic C-H functionalization, as illustrated in Scheme 1b.<sup>5</sup> More recently our group disclosed the intermolecular allylic C-H amination of internal aryl and alkyl alkenes with primary and secondary amines bearing only one electron withdrawing group (Scheme 1c).<sup>6</sup>

**Scheme 1.** Transition metal catalyzed allylic C-H amination with nucleophilic amines



The development of catalytic methods for C(sp<sup>3</sup>)-H functionalization has exceeded our mechanistic understanding of these transformations. In the case of rhodium catalyzed allylic C-H functionalization, Cossy suggested that a plausible mechanism would involve an allylic C-H insertion to generate a Rh( $\pi$ -allyl) complex followed by N-metallation and reductive elimination from a Rh(III) intermediate to generate the allylic amine and a Rh(I) species that would be reoxidized to Rh(III) to complete the catalytic cycle. This mechanism is in accord with reports on the rhodium catalyzed allylic substitution with phosphine and phosphite supporting ligands.<sup>7</sup> Similar catalytic reactions involving Rh(III/I) have also been proposed for C(sp<sup>2</sup>)-H bond activations that utilize cyclopentadienyl supporting ligands.<sup>8</sup> However, we note that higher oxidation states of rhodium have also been proposed in Cp\*Rh catalyzed C(sp<sup>2</sup>)-H activation.<sup>9</sup>

Providing additional complexity to the mechanistic picture, the synthesis and reactivity of several group IX  $\pi$ -allyl complexes similar to those invoked by Cossy and our group in the Cp\*Rh catalyzed allylic C-H amination have been reported. Bergman isolated and characterized the Cp\*Rh( $\pi$ -allyl) complex **I** (Figure 1a)<sup>10</sup> and Stryker

subsequently determined the structures of the *exo* and *endo* isomers of IrCp\*( $\pi$ -allyl) complex **II** (Figure 1b).<sup>10b</sup> In each case, the *exo*-isomers of the  $\pi$ -allyl complexes react with hard nucleophiles at the central carbon to generate metallocyclobutane products. Additionally, Tanaka reported the isolation and characterization of the Rh(III)Cp<sup>E</sup>( $\pi$ -allyl) complex **III** bearing a pendent tosyl amine nucleophile (Figure 1c).<sup>10c</sup> When complex **III** was treated with AgSbF<sub>6</sub> to abstract the chloride and generate a vacant coordination site for *N*-metallation, the expected cyclization product was not observed. When complex **III** was treated with both AgSbF<sub>6</sub> and Cu(OAc)<sub>2</sub>, the expected amination product was observed in 51% yield. The authors did not postulate specific roles of Cu(OAc)<sub>2</sub> in this transformation. However, Jones and coworkers have reported the use of a copper salt as an oxidant to induce reductive elimination of a C(sp<sup>2</sup>)–N(sp<sup>2</sup>) bond from a Cp\*Rh<sup>III</sup> complex.<sup>9b</sup> In 2017, Chang and Baik reported a detailed mechanistic study of a C–H arylation reaction catalyzed by Cp\*Ir, in which a strong oxidant facilitates the C–H arylation by oxidizing the metallated  $\pi$ -allyl complex via an oxidatively induced reductive elimination (Figure 1d).<sup>11</sup>

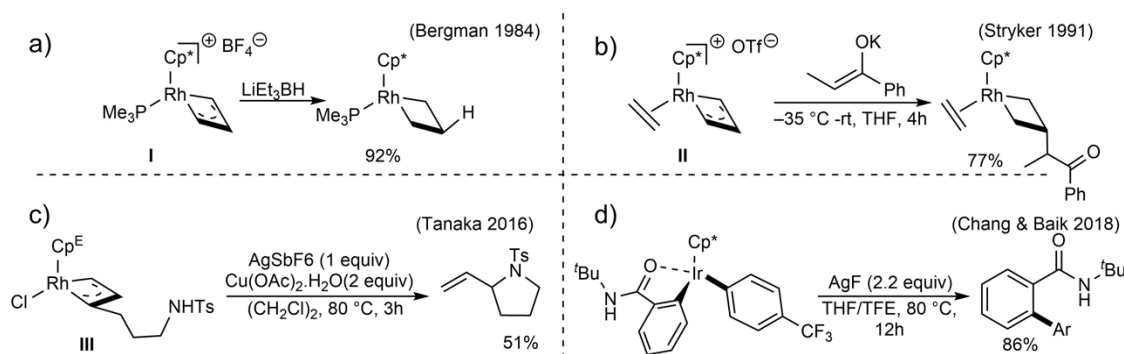
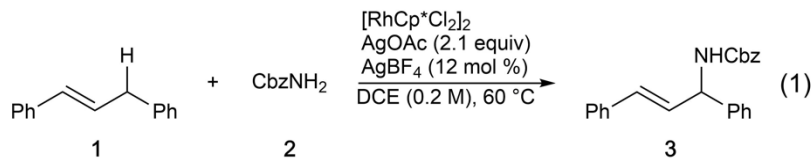


**Figure 1.** Previously reported reactions of group IX  $\pi$ -allyl complexes

The reactivity of  $\pi$ -allyl complexes (**I–III**) is largely inconsistent with the previously proposed Rh(III/I) mechanism for Cp\*Rh catalyzed allylic C–H amination. Herein, we describe a detailed study combining experimental observations including kinetic analysis, isolation and characterizations of reactivities of putative intermediates, and cyclic voltammetry measurements, that are corroborated with quantum mechanical calculations, to elucidate the mechanism of the Rh-catalyzed C(sp<sup>3</sup>)–H activations that afford allylic amination products.

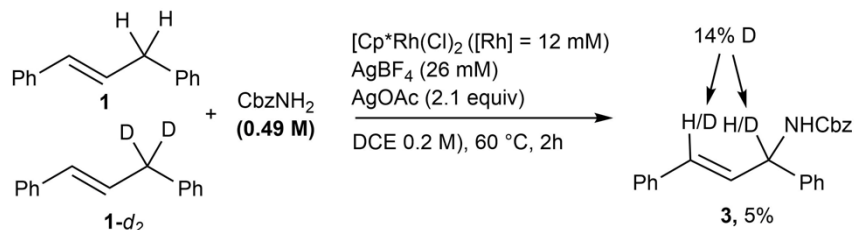
## RESULTS AND DISCUSSION

**Kinetic analysis:** To obtain experimental data to facilitate a deeper understanding of the mechanism for the rhodium catalyzed allylic C–H amination, we targeted 1,3-diphenylpropene **1** as a simple model substrate, in which complications caused by regioselectivity are not present (eq 1). We note that our initial attempt to monitor the reaction progress using *p*-toluenesulfonamide as a nucleophile was complicated due to its insolubility, leading us to choose benzyl carbamate as the nucleophile.



Analysis of initial rates of reactions of diphenylpropene **1** with benzyl carbamate **2** catalyzed by  $[\text{Cp}^*\text{RhCl}_2]_2/\text{AgBF}_4$  showed that allylic amine production was linearly dependent on the concentrations of the Rh, alkene, and carbamate with slopes of  $k_1 = 2.4 \pm 0.4 \times 10^{-4} \text{ s}^{-1}$ ,  $k_2 = 1.5 \pm 0.1 \times 10^{-5} \text{ s}^{-1}$  and  $k_3 = -5.2 \pm 0.6 \times 10^{-5} \text{ s}^{-1}$  respectively (Figures S2-S4). These data indicate the reaction is first-order in rhodium and alkene concentrations. Also an inverse rate constant for the carbamate concentration was observed, that is consistent with the carbamate nucleophile binding to the rhodium catalyst in an off cycle equilibrium (Scheme S1).

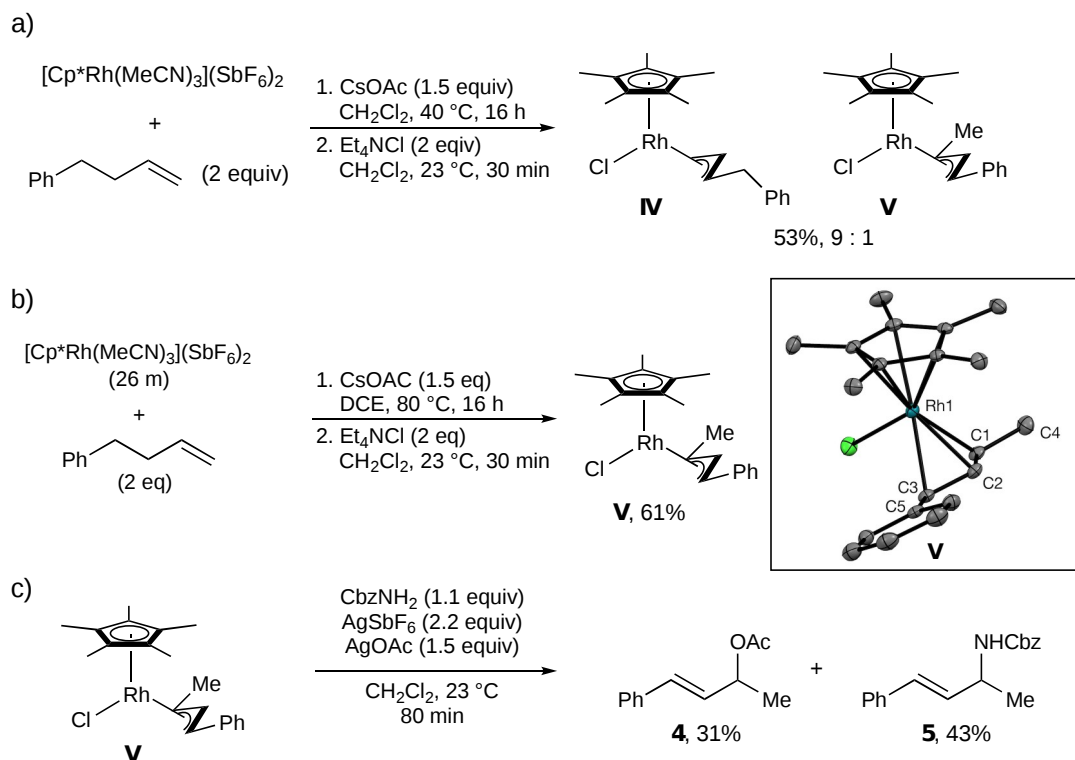
Deuterium exchange experiments provide insight into the rate determining step (RDS). A 1:1 mixture of **1** and **1-d<sub>2</sub>** (0.2 M) in DCE was treated with benzyl carbamate **2** (0.49 M),  $[\text{Cp}^*\text{RhCl}_2]_2$  ( $[\text{Rh}] = 12 \text{ mM}$ ),  $\text{AgBF}_4$  (26 mM), and  $\text{AgOAc}$  (2.1 equiv). The reaction was stopped after 2 hours (~10% conversion), and allylic amine **3** was isolated in 5% yield (Figure 2). Analysis of the  $^1\text{H}$  NMR of **3** established a 14% deuterium incorporation at both C1 and C3, which is consistent with a primary KIE of  $k_{\text{H}}/k_{\text{D}} = 2.5$ . In our original disclosure of the rhodium catalyzed allylic C–H amination, we showed that C–H cleavage was irreversible.<sup>6</sup> Taken together, these observations along with the first order dependence of rate on **1**, establish that C–H cleavage is rate-determining.<sup>11</sup>



**Figure 2.** Amination of a 1:1 mixture of **1** and **1-d<sub>2</sub>** with benzyl carbamate catalyzed by  $[\text{Cp}^*\text{RhCl}_2]_2$

### Synthesis, Characterization, and Reactivity of rhodium $\pi$ -allyl complexes

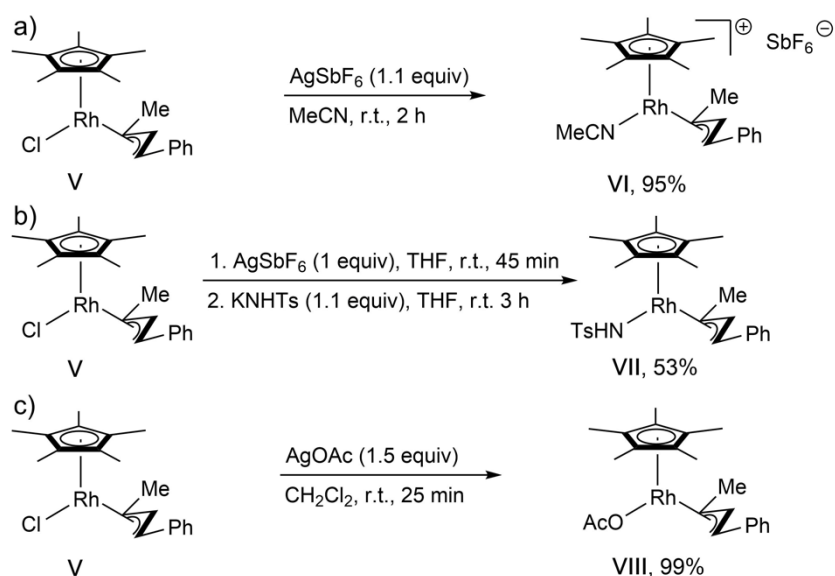
The kinetic data presented above are consistent with the notion that C–H activation step is rate limiting, and consequently overall reaction kinetics cannot be used to probe the mechanism of C–N bond formation or catalyst regeneration. In order to gain insight into this sequence in the catalytic cycle, we synthesized plausible putative intermediates in the catalytic cycle and examined their reactivities. Analogous to Tanaka's synthesis of  $\text{Cp}^*\text{Rh}(\pi\text{-allyl})$  complex **III**, we attempted to synthesize a  $\text{Rh}(\pi\text{-allyl})$  complex with a  $\text{Cp}^*$  supporting ligand. Initial attempts to make a  $\text{Cp}^*\text{Rh}(\pi\text{-allyl})$  complex starting from  $[\text{Cp}^*\text{RhCl}_2]_2$  in the presence of  $\text{AgSbF}_6$  were unsuccessful and led to a complex mixture of products. However, stirring  $[\text{Cp}^*\text{Rh}(\text{NCMe})_3](\text{SbF}_6)_2$  with cesium acetate (1.5 equiv) and 4-phenyl-1-butene (2 equiv) in  $\text{CH}_2\text{Cl}_2$  at room temperature for 16 h followed by the addition of tetraethylammonium chloride, lead to the isolation of a mixture of  $\text{Rh}(\pi\text{-allyl})$  complexes **IV** and **V** in 53% yield (9:1 ratio, Figure 3a). By using DCE as a solvent and heating the reaction to  $80^\circ\text{C}$  we were able to isolate complex **V** exclusively as the thermodynamic product in 61% yield (Figure 3b).



**Figure 3.** Synthesis and structure of  $\text{Cp}^*\text{Rh}(\pi\text{-allyl})\text{Cl}$  complex. ORTEP diagram of **V** depicted with ellipsoids shown at the 50% probability level and hydrogen atoms omitted for clarity

Complex **V** was fully characterized by  $^1\text{H}$  and  $^{13}\text{C}$  NMR spectroscopy and single crystal X-ray diffraction. The  $^1\text{H}$  NMR spectrum of **V** displayed a characteristic triplet of doublets at  $\delta = 4.55$  ppm with coupling constants  $J_{\text{HH}} = 10.7$  Hz and  $J_{\text{RH}} = 2.0$  Hz corresponding to the proton attached to the central carbon of the  $\pi$ -allyl ligand. Vapor diffusion of pentane into a concentrated ether solution of **V** at 25 °C provided crystals suitable for X-ray analysis (Figure 3b, inset). The allyl ligand of complex **V** adopts a near planar geometry with dihedral angles  $\text{C1}-\text{C2}-\text{C3}-\text{C5} = 173.8^\circ$  and  $\text{C4}-\text{C1}-\text{C2}-\text{C3} = 178.6^\circ$ . The  $\text{Rh}-\text{C1}$  and  $\text{Rh}-\text{C3}$  bond distances are approximately equal with bond lengths of 2.203(2) and 2.219(2) Å respectively while the  $\text{Rh}-\text{C2}$  bond length is significantly shorter with a bond length of 2.133(2) Å.

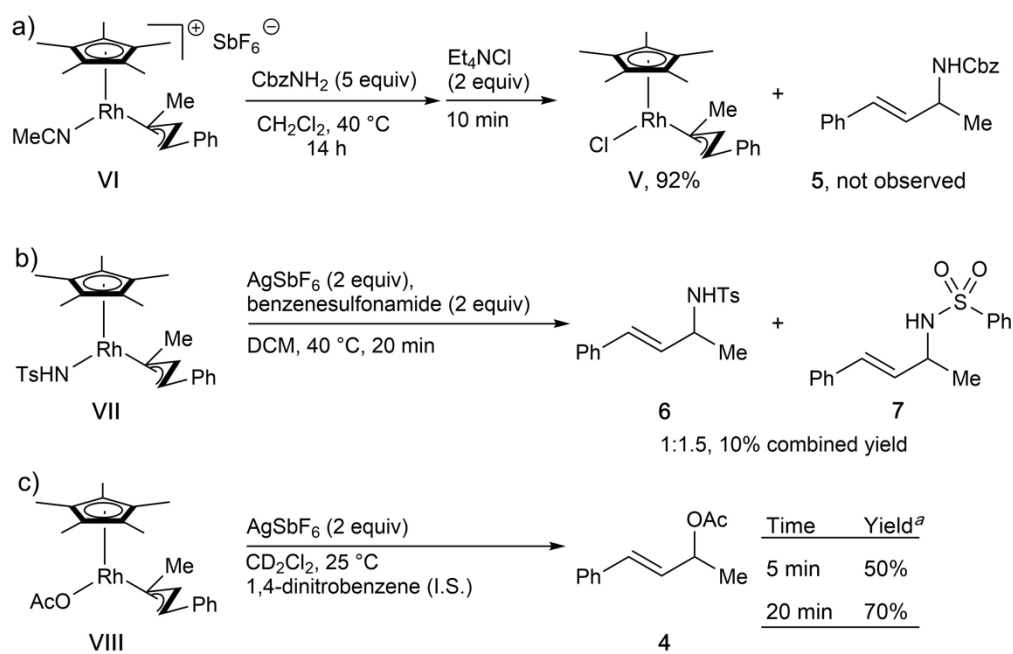
With complex **V** in hand, we began to investigate  $\text{Cp}^*\text{Rh}(\pi\text{-allyl})$  complexes' reactivity toward nucleophiles. In an initial experiment, complex **V** was treated with a single equivalent of benzyl carbamate **2** in  $\text{CH}_2\text{Cl}_2$  at 23 °C. Unsurprisingly, even after 48 h, complex **V** remained unreacted. However, when complex **V** was treated with benzylcarbamate (**2**, 1.1 equiv) in the presence of  $\text{AgSbF}_6$  (2.2 equiv, as a halide abstractor) and  $\text{AgOAc}$  (1.5 equiv) in  $\text{CH}_2\text{Cl}_2$  at 23 °C to mimic the reaction conditions that yielded aminated products, allylic acetate **4** and the expected allylic amine **5** were generated in 31% and 43% yield respectively (Figure 3c). This result suggests that while **V** is likely not a catalytically relevant species, the cationic complex generated from abstracting a chloride from **V** could be. Also the result indicate that silver additives are essential for the activation of the  $\text{Rh}(\pi\text{-allyl})$  complex **V**. Lastly, the significant quantities of allylic acetate **4** observed in the reaction lead us to consider the possibility that the amination reaction might proceed through an allylic acetate intermediate.



**Figure 4.** Synthesis of Cp<sup>\*</sup>Rh(III)(π-allyl) complexes bearing acetonitrile, tosylamine and acetate ligands

To further probe these possibilities we synthesized the cationic Cp<sup>\*</sup>Rh(π-allyl)(MeCN)(SbF<sub>6</sub>) complex **VI** (Figure 4a), the Cp<sup>\*</sup>Rh(π-allyl)(NHTs) complex **VII** (Figure 4b) and the Cp<sup>\*</sup>Rh(π-allyl)(OAc) complex **VIII** (Figure 4c). Complexes **VI**, **VII** and **VIII** were characterized by <sup>1</sup>H and <sup>13</sup>C NMR spectroscopy and **VII** and **VIII** were further characterized by single crystal X-ray diffractions (Figures S5 and S6). The isolation of complexes **VII** and **VIII** unambiguously rules out the possibility that allylic C-N or C-O bond formation by reductive elimination from these Rh(III) species is possible under the catalytic conditions (Figures S5 and S6). Furthermore, the fact that no allylic amine or allylic acetate product was observed during the synthesis of complexes suggests that outer-sphere nucleophilic attack of these nucleophiles on cationic Rh(III)(π-allyl) complexes is also not a plausible explanation for product formation in the catalytic reaction.

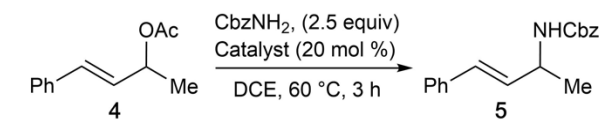
This conclusion is further supported by the observation that when cationic complex **VI** was reacted with benzylcarbamate at 40°C for 14h that did not yield allylic amine. Instead, Cp<sup>\*</sup>Rh(π-allyl)Cl complex **V** was recovered in 92% yield after a chloride quench (Figure 5a). To investigate the potential for an oxidatively induced reductive elimination mechanism to be operating, we exposed both Cp<sup>\*</sup>Rh(π-allyl)(NHTs) complex **VII** and Cp<sup>\*</sup>Rh(π-allyl)(OAc) complex **VIII** to two equivalents AgSbF<sub>6</sub>. In the reaction of Cp<sup>\*</sup>Rh(π-allyl)(NHTs) complex **VII**, two equivalents of benzensulfonamide were included that allows us to probe both an oxidatively induced inner-sphere reductive elimination, and an oxidatively induced outer-sphere nucleophilic attack. In this reaction, only 10% combined yield of allylic amine products (**6** and **7**) was observed. No rhodium(π-allyl) complexes could be recovered (Figure 5b). In contrast, when the Cp<sup>\*</sup>Rh(π-allyl)(OAc) complex **VIII** was oxidized with two equivalents AgSbF<sub>6</sub>, clean conversion to the allylic acetate product **4** was observed (Figure 5c). These observations suggest that the catalytic allylic amination reactions proceed through an allylic acetate intermediate, obtained by an oxidatively induced reductive elimination mechanism.



**Figure 5.** Reactivity of Cp<sup>\*</sup>Rh(III)(π-allyl) complexes demonstrating the feasibility of oxidatively induced reductive elimination of an allyl acetate. <sup>a</sup>Yields were determined by <sup>1</sup>H NMR analysis of the reaction mixture using 1,4-dinitrobenzene as an internal standard.

To complete our experimental investigation, we demonstrated that allylic acetate **4** is readily converted to the allylic amine **3** in the presence of the Lewis acid components present in the catalytic reactions (Table 1). Both cationic Ag(I) and cationic Rh(III) are able to promote this reaction. In the absence of either silver cation or Cp<sup>\*</sup>Rh, the allylic acetate remained unchanged. These data provide a plausible hypothesis of the pathway toward the completion of the allylic amination catalytic cycle.

**Table 1.** Reactivity of allylic acetate **4** benzyl carbamate **2** in the presence of Ag(I) or Rh(III) as a catalyst.

		
entry	Catalyst	Yield
1	AgSbF <sub>6</sub>	91%
2	AgBF <sub>4</sub>	76%
3	[Cp <sup>*</sup> RhCl <sub>2</sub> ] <sub>2</sub> /AgSbF <sub>6</sub> <sup>a</sup>	73%
4	[Cp <sup>*</sup> Rh(NCMe) <sub>3</sub> ](SbF <sub>6</sub> ) <sub>2</sub>	84%
5	none	0% <sup>b</sup>

<sup>a</sup>[Cp<sup>\*</sup>RhCl<sub>2</sub>]<sub>2</sub> (25 mM) and AgSbF<sub>6</sub> (40 mM) were stirred in DCM with benzyl carbamate (**2**) at 60 °C for 30 min before allylic acetate **6** was added to be sure that there was no Ag<sup>+</sup> in solution. <sup>b</sup>Allylic amine was not observed by <sup>1</sup>H NMR.

## Computational Investigation of the key steps in the catalytic cycle

Density functional theory (DFT) calculations were carried out to construct a catalytic mechanism incorporating the experimental observations mentioned above. Using 1,3-diphenylpropene **1** as the substrate, we compared the activation barriers of the reductive elimination from the three relevant oxidation states Rh(III), Rh(IV) and Rh(V), as illustrated in Figure 6. The reductive elimination initiated from the Rh(III) intermediate to give Rh(I) is not viable, as the computed activation barrier of 38.4 kcal/mol corresponds to an Eyring rate of  $0.6 \times 10^{-10}$  mol/day at 298 K (Figure 6a). As expected, the oxidation of the metal center to Rh(IV) lowers the activation barrier notably by more than 21 kcal/mol to 17.6 kcal/mol (Figure 6b), which suggests an acceleration of the reaction by more than  $10^{10}$  fold compared to the Rh(III) intermediate. Our calculations suggest that a second oxidation to access the Rh(V) center does not enhance the reaction rate further, as the calculated barrier increases to 19.5 kcal/mol (Figure 6c).

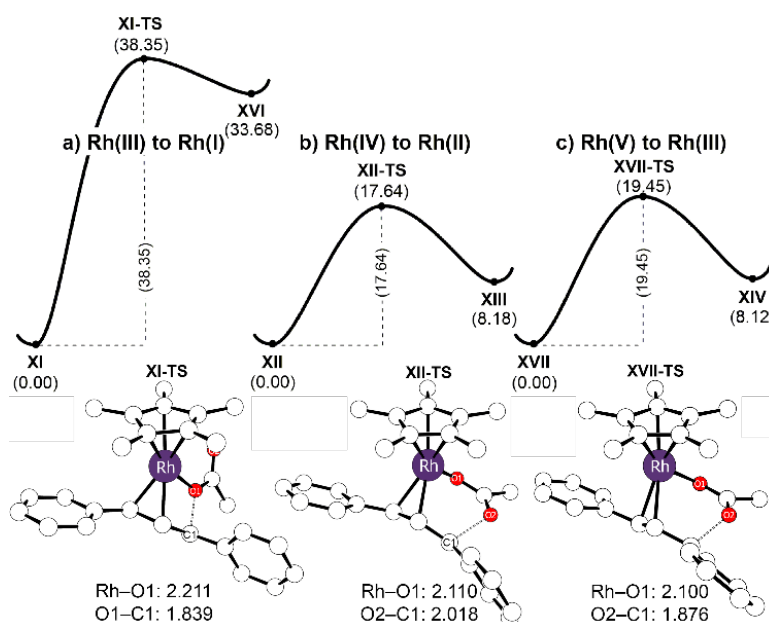


**Figure 6.** Calculated energy profiles for reductive elimination from the a) Rh(III)–, b) Rh(IV)–, and c) Rh(V)– $\pi$ -allyl intermediates, leading to the Rh(I), Rh(II), and Rh(III) products, respectively. The detailed molecular structure of each TS is shown as well. The unit of energy is kcal/mol and of bond length is Å.

A closer inspection of the transition structures reveals that the two oxygen atoms of the acetate introduce a slight variation in the transition states. During the reductive elimination from the Rh(III)-center, the O–C bond is formed by the acetate-oxygen that is directly bound to the metal, as illustrated in Figure 6a. The Rh–O bond elongates from 2.121 to 2.211 Å as the transition state **XI-TS** is traversed with the C–O distance being 1.839 Å. This bond forming event is best conceptualized by considering that the allylic fragment formally donates two electrons to the Rh-center to accomplish the reductive part of the reductive elimination step. Consequently, it becomes a positively polarized electrophile that can engage the acetate and form the C–O bond. Of course, these two processes are concerted in reality, but it is instructive to visualize them separately. When the metal is oxidized to Rh(IV) or Rh(V), it is the distal oxygen of the acetate that attacks the carbon and the Rh–O bond is mostly



maintained with the Rh–O bond lengths being 2.110 (**XII-TS**) and 2.100 Å (**XVII-TS**), respectively, as illustrated in Figures 6b and 6c. Thus, whereas the Rh(III) center carries out a classical reductive elimination, the other higher valent metal centers prefer to reductively couple the acetate with the allyl functionality without eliminating the acetate. This subtle change in mechanism is easy to understand considering that the Rh–O bond becomes much stronger in Rh(IV) and Rh(V) compared to Rh(III). As the acetate acts as a nucleophile in this step, the higher oxidation state at the metal decreases its nucleophilicity and results in a higher barrier in the Rh(V)-complex. Thus, Rh(IV) constitutes an ideal compromise between the two governing forces, namely the ability of the metal center to oxidize the allyl fragment and the nucleophilicity of the acetate.

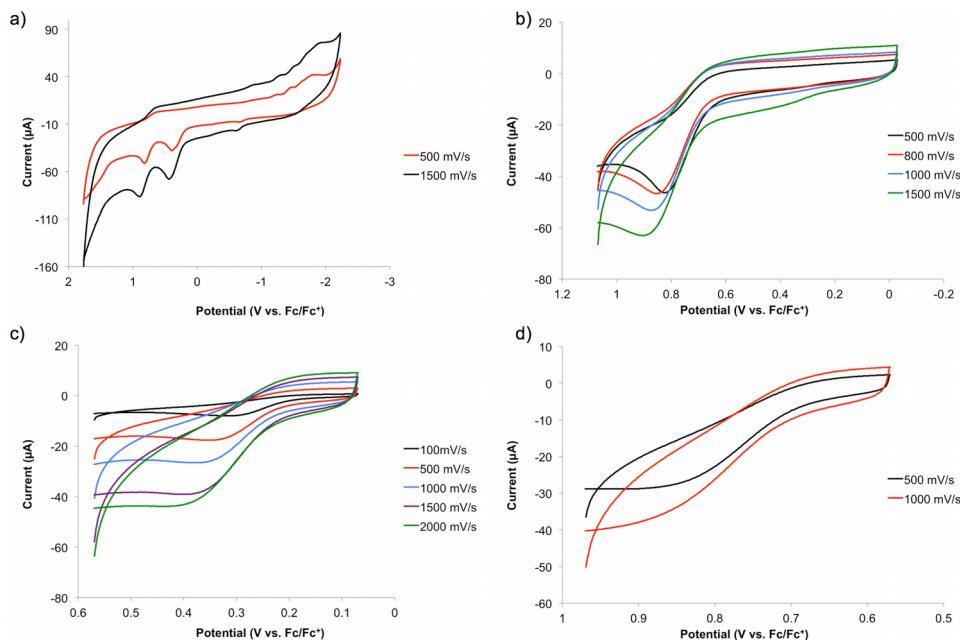


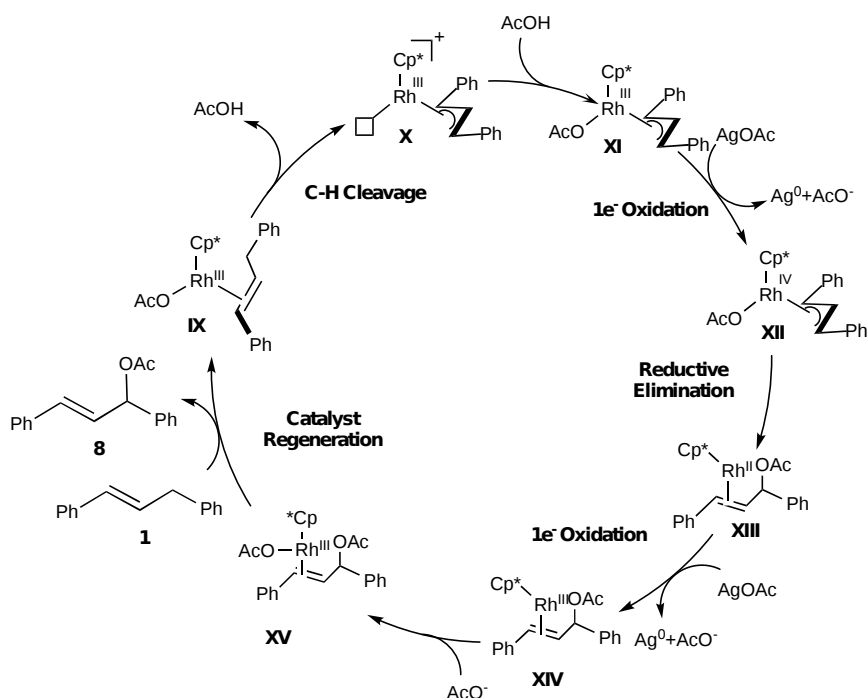
**Figure 7.** Cyclic voltammograms of rhodium acetate complex **VIII**. Voltammograms recorded in  $\text{CH}_2\text{Cl}_2$  with 0.1 M TBAPF<sub>6</sub> as the supporting electrolyte.

To test the proposed catalytic mechanism, cyclic voltammetry experiments were carried out. Complex **VIII** showed two irreversible oxidation waves, suggesting that both Rh(IV) and Rh(V) are accessible on an electrochemical time scale (Figures 7a and 7b). As is expected for an electrochemical step that is coupled with a chemical event, the peak position of both steps are scan rate dependent (Figures 7c and 7d). The first oxidation occurs at  $E_p = -0.42$  V versus Fc/Fc<sup>+</sup> which we assign to the Rh(III)/(IV) couple, and the second event occurs at  $E_p = -0.85$  V that is attributed to the Rh(IV)/(V) couple. Importantly, even at fast scan rates of 2,000 mV/s the Rh(III)/(IV) redox event is irreversible suggesting that reductive elimination from Rh(IV) is fast (Figure 7c). Given that the redox potential of Ag<sup>+</sup> in  $\text{CH}_2\text{Cl}_2$  is 0.65 V, it is unlikely that the Rh(V) complex can be accessed via chemical oxidation. Taken together, these data support a catalytic cycle that consists of the sequence Rh(III) → Rh(IV) → Rh(II) → Rh(III).

Scheme 2 summarizes the proposed mechanism of the Rh catalyzed allylic acetylation and the corresponding reaction energy profile is shown in Figure 8. The catalytic cycle begins with the coordination of the

acetate and the olefin substrates **1** to the Cp<sup>\*</sup>Rh fragment to form the initial reactant complex **IX**, which undergoes a concerted metalation deprotonation (CMD) traversing the transition **VI-TS** to activate the allylic C–H bond. The computed activation energy for this step is 26.7 kcal/mol, which is in good agreement with the experimental observation that a mildly elevated temperature is required to prepare the acetylated intermediate **XIII** (*vide supra*). Ligand exchange affords the Cp<sup>\*</sup>Rh(III)( $\pi$ -allyl)OAc complex **XI**. As discussed above, reductive elimination from this intermediate is associated with a very high barrier (Figure 6a). To push the reaction forward, one electron oxidation of Rh(III) to Rh(IV) is needed which enables the reductive elimination via **XIV-TS** with a computed barrier of 17.6 kcal/mol. Intermediate **XIII** can easily undergo an one-electron oxidation to form the Rh(III) intermediate **XIV**, which releases product **4** via ligand exchange steps.

**Scheme 2.** Proposed catalytic mechanism of the rhodium catalyzed allylic acetylation going through Rh(IV)  $\rightarrow$  Rh(II)



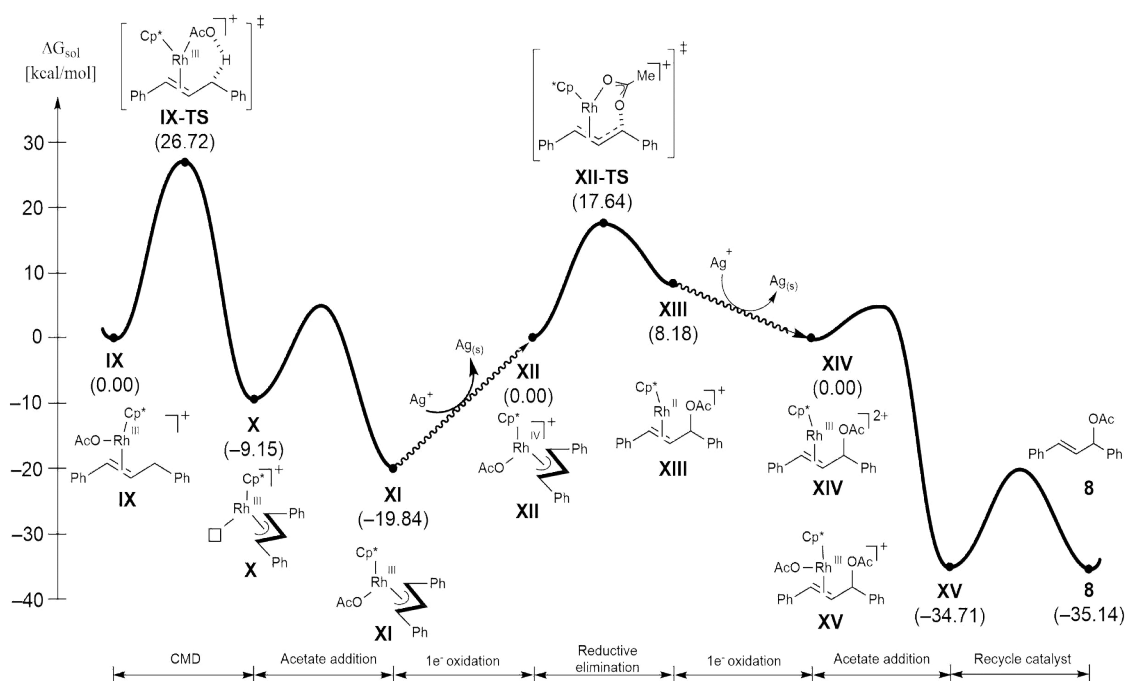
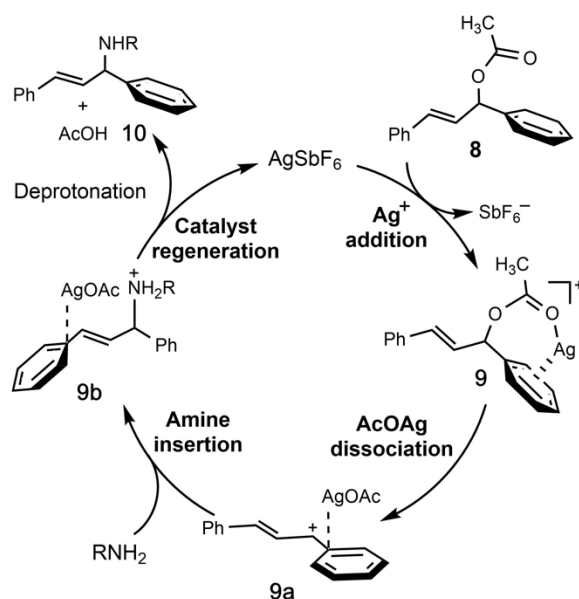


**Figure 8.** Energy profile for Rh-catalyzed allylic acetylation going through Rh (IV  $\rightarrow$  II)

**Formation of Allylic Amines** With the detailed mechanism of the intermediate allylic acetate formation in hand, we turned our attention to the role of the silver and rhodium salts in the conversion of the allylic acetate to the allylic amine product, seeking to differentiate between simple Lewis acid promoted nucleophilic substitution or a more complicated allylic substitution proceeding through additional  $\pi$ -allyl complexes. In the following, we delineate the mechanistic details of the two possible mechanistic hypotheses for the formation of allylic amine product from the allylic acetate intermediate, by means of DFT calculations.

**Scheme 3.** Proposed mechanism for  $\text{AgSbF}_6$  catalyzed allylic C–H amination from allylic acetate



Inspired by the related  $\text{AgSbF}_6$  catalyzed amination of allylic acetate,<sup>12</sup> we compiled a plausible mechanistic pathway for the amination reaction which involves an initial  $\text{Ag}^+$  addition to allylic acetate to prepare a silver coordinated allylic acetate complex, as illustrated in Scheme 3. The energy profile for the allylic amination of allylic acetate **8** catalyzed by  $\text{Ag}^+$  is depicted in Figure 9. The catalytic cycle is initiated by the addition of  $\text{Ag}^+$  to allylic acetate intermediate yielding **9**. Out of the three possible scenarios of the nucleophilic substitutions ( $\text{S}_{\text{N}}1$ ,  $\text{S}_{\text{N}}2$ , and  $\text{S}_{\text{N}}2'$ ), our DFT calculations suggested that the  $\text{S}_{\text{N}}1$  mechanism is the most plausible route for the nucleophilic substitution. The dissociation of  $\text{AgOAc}$ , facilitated by  $\text{Ag}^+$  as a Lewis acid, yields an allylic cation intermediate **9a**, associated with an activation barrier of 14.4 kcal/mol (**9-TS**). The addition of nucleophile (**9a-TS**) requires 16.7 kcal/mol of activation energy, which is predicted to be the most difficult step to activate of the amination reaction, yet is viable under the reaction condition used. In comparison, the  $\text{S}_{\text{N}}2$  and  $\text{S}_{\text{N}}2'$  reactions are much more difficult to activate with the calculated activation barriers being 23.0 and 27.6 kcal/mol, respectively. To push the reaction forward, the aminated intermediate **9b** undergoes a concerted deprotonation via traversing the transition structure **9b-TS** to produce the allylic amine product bound to a silver cation **9c**.

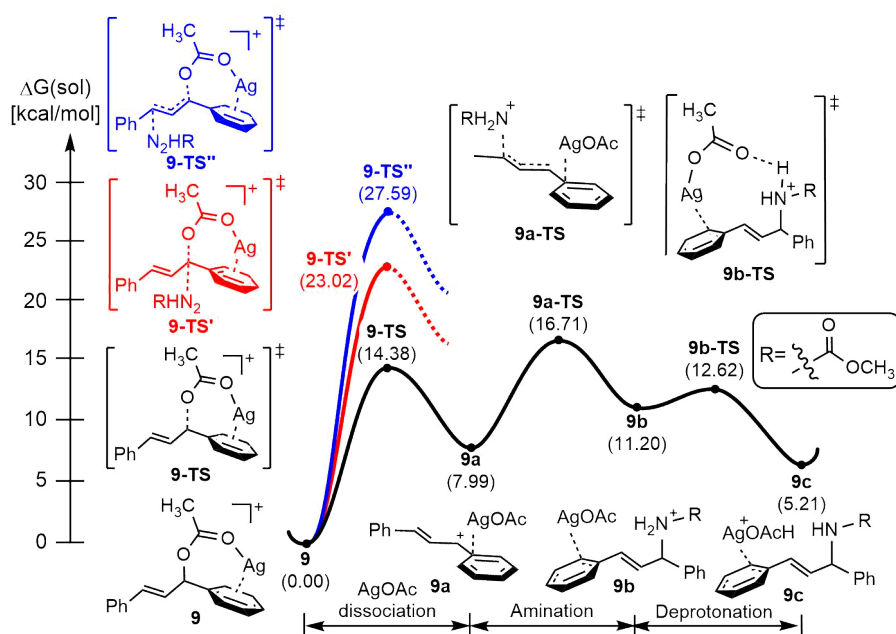
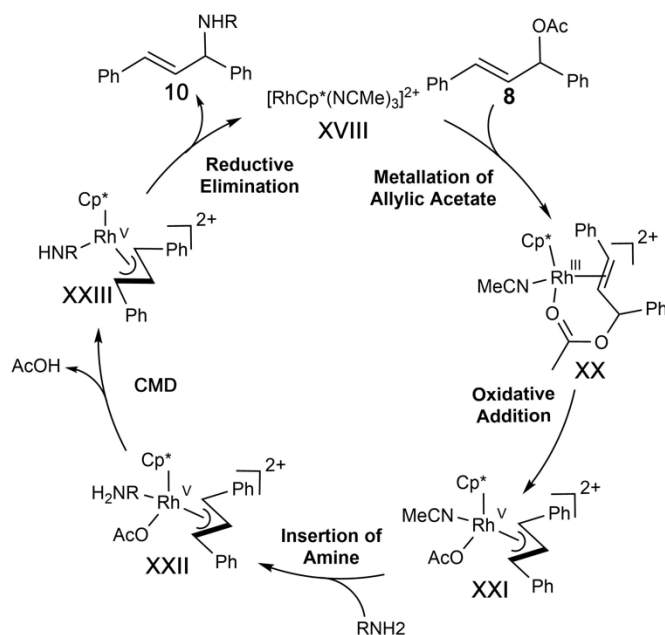


**Figure 9.** Energy profile for  $\text{AgSbF}_6$  catalyzed allylic C–H amination from allylic acetate

**Scheme 4.** Proposed mechanism of the inner-sphere Rh-catalyzed allylic C–H amination from allylic acetate



The catalytic cycle for a Cp\*Rh catalyzed allylic amination of allylic acetate via the inner-sphere mechanism is depicted schematically in Scheme 4. A complete energy profile of the inner-sphere amination is depicted in Figure 10. To reduce the computational cost, we simplified the amine source to methylcarbamate. Commencing from the active catalyst **XVIII**, an intermediate **XIX** is formed through coordination of the allylic double bond, that is 12.8 kcal/mol uphill in energy. A ligand exchange step follows to allow the acetate of the substrate to coordinate the metal center to form **XX**, that is found at 9.5 kcal/mol higher in energy from that of the active catalyst. Subsequent oxidative addition of acetate takes place to yield an intermediate **XXI** that is 15.9 kcal/mol uphill in energy, via traversing the transition state **XX-TS** with an activation barrier of 22.8 kcal/mol. After the addition of acetate, a ligand exchange step follows to replace a coordinating acetonitrile with the amine ligand (**XXII**). The amine ligand undergoes a concerted metalation and deprotonation step (CMD) with the removal of an acetic acid molecule via a transition structure (**XXII-TS**) with the activation barrier of 26.2 kcal/mol, to find an intermediate **XXIII** that is 20.1 kcal/mol uphill in energy. In the next step, Rh(V) complex undergoes the reductive elimination from Rh(V) → Rh(III) to construct a new C–N bond via traversing a transition structure **XXIII-TS** with an activation energy barrier of 27.3 kcal/mol. The reductive elimination is the most difficult step to activate throughout the inner-sphere amination pathway. The computed activation energy barrier is moderately high yet is predicted to be viable under the reaction conditions used in some of the catalytic amination reactions (60°C), as the computed Eyring rate of the activation is 0.2 mol/day at 60°C. Upon completion of the reductive elimination, ligand exchanges steps follow to yield the aminated product **10** and to regenerate the catalyst **XXIII**. We also investigated the nucleophilic substitution of acetate by amine via the outer-sphere mechanism (Scheme S4 and Figure S10), and found a computed activation energy barrier for the amination of 41.0 kcal/mol, precluding this mechanism under the reaction conditions used.

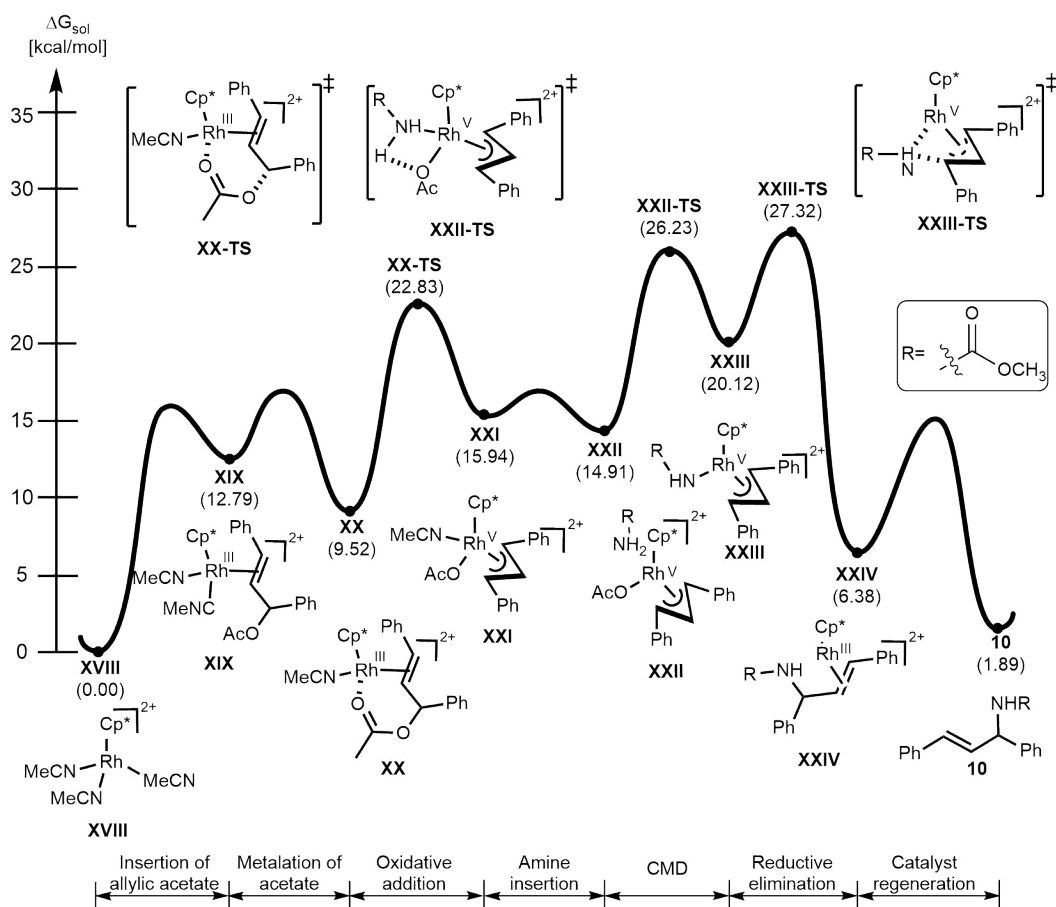


**Figure 10.** energy profile of the inner-sphere Rh-catalyzed amination of allylic acetate **4**

## CONCLUSIONS

The computational and experimental data provided a detailed picture of the rhodium-catalyzed  $\text{C}(\text{sp}^3)\text{--H}$  allylic amination. Overall, the rate-determining step of the entire catalytic cycles examined computationally was found to be the C–H activation of allylic substrate with a DFT-computed barrier of 26.8 kcal/mol. This is consistent with the experimental kinetic observations that also support C–H activation as the rate determining step in this transformation. Calculations revealed that the Rh catalyst facilitates the formation of the allylic acetate using the silver salt as an oxidizing agent via an oxidatively induced reductive elimination reaction<sup>11</sup> where the Rh(III) center of the key intermediate is first oxidized to Rh(IV). Interestingly, the two-electron oxidation to possibly access the Rh(V) analogue is not found to be helpful and we found good experimental evidence that Rh(IV) is indeed the catalytically competent species. Further experimental studies as well as DFT calculations suggested that the amination of the allylic acetate intermediate proceeds by an  $\text{S}_{\text{N}}1$  ligand exchange mechanism mediated by silver acting as a Lewis acid catalyst. Although a  $\text{Cp}^*\text{Rh}$  catalyzed pathway was calculated to be feasible under the reaction conditions, the barriers were significantly higher than those calculated for the silver promoted pathway, and are unlikely to contribute significantly to product formation. We note that this study provides insights that are likely applicable to the related rhodium catalyzed allylic etherification and arylation reactions that were recently disclosed,<sup>13</sup> but likely do not explain the allylic arylation reaction utilizing aryl boronic acids,<sup>14</sup> or the allylic

amidation processes using dioxazolone reagents.<sup>15</sup> Further studies to provide a unified mechanistic picture of this emergent field are required.

### Computational details

All calculations were constructed using computer models based on density functional theory (DFT)<sup>16</sup> implemented in the Jaguar 9.1 suite<sup>17</sup> of ab initio quantum chemistry programs. Geometry optimizations were performed using the B3LYP<sup>18</sup> functional including Grimme's D3 dispersion correction<sup>19</sup> and the 6-31G(d,p) basis set, where rhodium was represented with the Los Alamos LACVP basis set,<sup>20</sup> which incorporates effective core potentials that describes the relativistic effects (B3LYP-D3/LACVP). Upon completion of the geometry optimizations, single point SCF electronic energies of the optimized geometries were calculated using Dunning's correlation consistent triple- $\zeta$  basis set (cc-pVTZ(-f))<sup>21</sup> that includes a double set of the polarization functions. For rhodium, a modified version of LACVP, designed as LACV3P is used to match the effective core potential with triple- $\zeta$  quality was used for the single point SCF calculations (B3LYP-D3/cc-pVTZ(-f)/LACV3P). Solvation energies were evaluated using the self-consistent reaction field (SCRF)<sup>22</sup> approach based on the accurate numerical solutions of the Poisson-Boltzmann equation. For the solvation calculations, 6-31G(d,p)/LACVP basis at the optimized gas-phase geometries were used with the solvent dielectric constant of  $\epsilon = 9.08$  for the solvent medium considered (1,2-dichloroethane). It is noted that the solvation energies are contingent on the empirical parameterization of atomic radii used to generate the solute surface, wherein we used the standard set of optimized radii for H (1.150 Å), C (1.900 Å), N (1.600 Å), O (1.550 Å), Ag (1.574 Å), Sb (2.210 Å), F (1.682 Å), and Rh (1.464 Å) that are employed in the Jaguar 9.1 suite.<sup>23</sup> To confirm the proper convergence to well-defined minima (intermediates and products) or saddle points (transition structures) on the potential energy surface, vibrational frequencies based on harmonic approximation were computed with the 6-31G\*\*/LACVP basis set. The energy components were calculated by adopting the protocol given below (eqs 2–6):

$$G(\text{Sol}) = G(\text{gas}) + G(\text{solv}) \quad (2)$$

$$G(\text{gas}) = H(\text{gas}) - TS(\text{gas}) \quad (3)$$

$$H(\text{gas}) = E(\text{SCF}) + \text{ZPE} \quad (4)$$

$$\Delta E(\text{SCF}) = \Sigma E(\text{SCF}) \text{ for products} - \Sigma E(\text{SCF}) \text{ for reactants} \quad (5)$$

$$\Delta G(\text{sol}) = \Sigma G(\text{sol}) \text{ for products} - \Sigma G(\text{sol}) \text{ for reactants} \quad (6)$$

,  $G(\text{sol})$  is the Gibbs free energy in solution phase,  $G(\text{gas})$  is the Gibbs free energy in gas phase,  $G(\text{solv})$  is the free energy of solvation,  $H(\text{gas})$  is the enthalpy in gas phase,  $T$  is the temperature (298.15 K),  $S(\text{gas})$  is the entropy in gas phase, ZPE is the zero point energy, and  $E(\text{SCF})$  is the self-consistent electronic field energy calculated by the SCF procedure.<sup>24</sup>

## ASSOCIATED CONTENT

### Supporting Information

The supporting Information is available free of charge on the [ACS Publications website](#) at DOI:

## Author Information

### Corresponding Author

\*E-mail: [mbaik2805@kaist.ac.kr](mailto:mbaik2805@kaist.ac.kr)

\*E-mail: [sblakey@emory.edu](mailto:sblakey@emory.edu)

### ORCID

Mu-Hyun Baik: 0000-0002-8832-8187

Simon B. Blakey: 0000-0002-4100-8610

Jiyong Park: 0000-0002-3225-4510

Cora E. MacBeth: 0000-0003-3877-2236

Jaohn Bacsa: 0000-0001-5681-4458

### Notes

The authors declare no competing financial interest.

## ACKNOWLEDGMENT

The research was supported in part by the Institute for Basic Science (IBS-R010-DI) in Korea and by the National Science Foundation (NSF) under the CCI Center for Selective C-H Functionalization (CHE-1700982). NMR studies for this research were performed on instrumentation funded by the NSF (CHE-1531620). The X-ray analysis was done by the Emory X-ray Crystallography Facility using the Rigaku Synergy-S diffractometer, supported by the NSF (CHE-1626172).

## REFERENCES

- (a) Wang, N.-X.; Xing, Y.; Zhang, W., Advances in Transition-Metal-Catalyzed Direct  $sp^3$ -Carbon–Hydrogen Bond Functionalization. *Synlett* **2015**, 26 (15), 2088-2098.(b) Yang, X.; Shan, G.; Wang, L.; Rao, Y., Recent advances in transition metal (Pd, Ni)-catalyzed C( $sp^3$ ) H bond activation with bidentate directing groups. *Tetrahedron Lett.* **2016**, 57 (8), 819-836.(c) Saint-Denis, T. G.; Zhu, R.-Y.; Chen, G.; Wu, Q.-F.; Yu, J.-Q., Enantioselective C( $sp$ )–H bond activation by chiral transition metal catalysts. *Science* **2018**, 359 (6377).(d) Chu, J. C. K.; Rovis, T., Complementary Strategies for Directed C( $sp$ )-H Functionalization: A Comparison of Transition-Metal-Catalyzed Activation, Hydrogen Atom Transfer, and Carbene/Nitrene Transfer. *Angew. Chem. Int. Ed Engl.* **2018**, 57 (1), 62-101.
- Li, C.-J., Cross-Dehydrogenative Coupling (CDC): Exploring C–C Bond Formations beyond Functional Group Transformations. *Acc. Chem. Res.* **2009**, 42 (2), 335-344.
- Chen, M. S.; Whilte, M. C., A Sulfoxide-Promoted, Catalytic Method for the Regioselective Synthesis of Allylic Acetates from Monosubstituted Olefins via C–H Oxidation. *J. Am. Chem. Soc.* **2004**, 126 (5), 1346-1347.
- (a) Young, A. J.; White, M. C., Catalytic Intermolecular Allylic C–H Alkylation. *J. Am. Chem. Soc.* **2008**, 130 (43), 14090-14091.(b) Reed, S. A.; White, M. C., Catalytic Intermolecular Linear Allylic C–H Amination via Heterobimetallic Catalysis. *J. Am. Chem. Soc.* **2008**, 130 (11), 3316-3318.(c) Reed, S. A.; Mazzotti, A. R.; White,



- M. C., A Catalytic, Brønsted Base Strategy for Intermolecular Allylic C–H Amination. *J. Am. Chem. Soc.* **2009**, *131* (33), 11701–11706. (d) Pattillo, C. C.; Strambeanu, I. I.; Calleja, P.; Vermeulen, N. A.; Mizuno, T.; White, M. C., Aerobic Linear Allylic C–H Amination: Overcoming Benzoquinone Inhibition. *J. Am. Chem. Soc.* **2016**, *138* (4), 1265–1272. (e) Ma, R.; White, M. C., C–H to C–N Cross-Coupling of Sulfonamides with Olefins. *J. Am. Chem. Soc.* **2018**, *140* (9), 3202–3205. (f) Fraunhofer, K. J.; White, M. C., syn-1,2-Amino Alcohols via Diastereoselective Allylic C–H Amination. *J. Am. Chem. Soc.* **2007**, *129* (23), 7274–7276. (g) Chen, M. S.; Prabakaran, N.; Labenz, N. A.; White, M. C., Serial Ligand Catalysis: A Highly Selective Allylic C–H Oxidation. *J. Am. Chem. Soc.* **2005**, *127* (19), 6970–6971. (h) Campbell, A. N.; White, P. B.; Guzei, I. A.; Stahl, S. S., Allylic C–H Acetoxylation with a 4,5-Diazafluorenone-Ligated Palladium Catalyst: A Ligand-Based Strategy To Achieve Aerobic Catalytic Turnover. *J. Am. Chem. Soc.* **2010**, *132* (43), 15116–15119.
5. Cochet, T.; Bellosta, V.; Roche, D.; Ortholand, J.-Y.; Greiner, A.; Cossy, J., Rhodium(III)-catalyzed allylic C–H bond amination. Synthesis of cyclic amines from  $\omega$ -unsaturated N-sulfonylamines. *Chem. Commun.* **2012**, *48* (87), 10745.
6. Burman, J. S.; Blakey, S. B., Regioselective Intermolecular Allylic C–H Amination of Disubstituted Olefins via Rhodium/ $\pi$ -Allyl Intermediates. *Angew. Chem. Int. Ed Engl.* **2017**, *129* (44), 13854–13857.
7. (a) Leahy, D. K.; Evans, P. A., Rhodium(I)-Catalyzed Allylic Substitution Reactions and Their Applications to Target Directed Synthesis. *ChemInform* **2005**, *36* (33). (b) Evans, P. A.; Nelson, J. D., Conservation of Absolute Configuration in the Acyclic Rhodium-Catalyzed Allylic Alkylation Reaction: Evidence for an Enyl( $\sigma$ - $\pi$ ) Organorhodium Intermediate. *J. Am. Chem. Soc.* **1998**, *120* (22), 5581–5582.
8. (a) Satoh, T.; Miura, M., Oxidative coupling of aromatic substrates with alkynes and alkenes under rhodium catalysis. *Chemistry* **2010**, *16* (37), 11212–11222. (b) *Issues in Chemistry and General Chemical Research: 2011 Edition*. ScholarlyEditions: 2012; p 6580.
9. (a) Vásquez-Céspedes, S.; Wang, X.; Glorius, F., Plausible Rh(V) Intermediates in Catalytic C–H Activation Reactions. *ACS Catal.* **2017**, *8* (1), 242–257. (b) Li, L.; Brennessel, W. W.; Jones, W. D., An Efficient Low-Temperature Route to Polycyclic Isoquinoline Salt Synthesis via C–H Activation with  $[\text{Cp}^*\text{MCl}_2]_2$  (M = Rh, Ir). *J. Am. Chem. Soc.* **2008**, *130* (37), 12414–12419.
10. (a) Periana, R. A.; Bergman, R. G., Rapid intramolecular rearrangement of a hydrido(cyclopropyl)rhodium complex to a rhodacyclobutane. Independent synthesis of the metallacycle by addition of hydride to the central carbon atom of a cationic rhodium  $\pi$ -allyl complex. *J. Am. Chem. Soc.* **1984**, *106* (23), 7272–7273. (b) Wakefield, J. B.; Stryker, J. M., Metallacyclobutanes from kinetic nucleophilic addition to  $\eta^3$ -allyl ethylene complexes of iridium. Regioselectivity dependence on nucleophile and allyl orientation. *J. Am. Chem. Soc.* **1991**, *113* (18), 7057–7059. (c) Shibata, Y.; Kudo, E.; Sugiyama, H.; Uekusa, H.; Tanaka, K., Facile Generation and Isolation of  $\pi$ -Allyl Complexes from Aliphatic Alkenes and an Electron-Deficient Rh(III) Complex: Key Intermediates of Allylic C–H Functionalization. *Organometallics* **2016**, *35* (10), 1547–1552.
11. Shin, K.; Park, Y.; Baik, M.-H.; Chang, S., Iridium-catalysed arylation of C–H bonds enabled by oxidatively induced reductive elimination. *Nat. Chem.* **2017**, *10*, 218.
12. Dagar, A.; Guin, S.; Samanta, S., AgSbF<sub>6</sub>-Catalyzed Tandem Reaction of 2-Alkynylanilines with Cyclic Enynes: Efficient access to 3-Furo[3,2-c]chromenylindoles and Related Scaffolds. *Asian J. Org. Chem.* **2017**, *7* (1), 123–127.
13. (a) Nelson, T. A. F.; Blakey, S. B., Intermolecular Allylic C–H Etherification of Internal Olefins. *Angew. Chem. Int. Ed Engl.* **2018**, *130* (45), 15127–15131. (b) Lerchen, A.; Knecht, T.; Koy, M.; Ernst, J. B.; Bergander, K.; Daniliuc, C. G.; Glorius, F., Non-Directed Cross-Dehydrogenative (Hetero) arylation of Allylic C (sp<sup>3</sup>)-H bonds enabled by C–H Activation. *Angew. Chem. Int. Ed.* **2018**, *57* (46), 15248–15252.
14. Knecht, T.; Pinkert, T.; Dalton, T.; Lerchen, A.; Glorius, F., Cp\*Rh<sup>III</sup>-Catalyzed Allyl–Aryl Coupling of Olefins and Arylboron Reagents Enabled by C(sp<sup>3</sup>)-H Activation. *ACS Catal.* **2019**, *9* (2), 1253–1257.
15. (a) Lei, H.; Rovis, T., Ir-Catalyzed Intermolecular Branch-Selective Allylic C–H Amidation of Unactivated Terminal Olefins. *J. Am. Chem. Soc.* **2019**, *141* (6), 2268–2273. (b) Knecht, T.; Mondal, S.; Ye, J.-H.; Das, M.; Glorius, F., Intermolecular, Branch-Selective, and Redox-Neutral Cp\*Ir<sup>III</sup>-Catalyzed Allylic C–H Amidation. *Angew. Chem. Int. Ed Engl.* **2019**, *58* (21), 7117–7121. (c) Burman, J. S.; Harris, R. J.; B. Farr, C. M.; Bacsá, J.; Blakey, S. B., Rh(III) and Ir(III)Cp\* Complexes Provide Complementary Regioselectivity Profiles in Intermolecular Allylic C–H Amidation Reactions. *ACS Catal.* **2019**, 5474–5479.
16. Parr, R. G.; Yang, W., *Density-Functional Theory of Atoms and Molecules*. Oxford University Press: 1994.
17. Bochevarov, A. D.; Harder, E.; Hughes, T. F.; Greenwood, J. R.; Braden, D. A.; Philipp, D. M.; Rinaldo, D.; Halls, M. D.; Zhang, J.; Friesner, R. A., Jaguar: A high-performance quantum chemistry software program with strengths in life and materials sciences. *Int. J. Quantum Chem.* **2013**, *113* (18), 2110–2142.
18. (a) Becke, A. D., Density-Functional Thermochemistry 3. The Role of Exact Exchange. *J. Chem. Phys.* **1993**, *98* (7), 5648–5652. (b) Lee, C.; Yang, W.; Parr, R. G., Development of the Colle-Salvetti correlation-energy formula into a functional of the electron-density. *Phys. Rev. B* **1988**, *37* (2), 785–789.

19. Grimme, S.; Antony, J.; Ehrlich, S.; Krieg, H., A consistent and accurate ab initio parametrization of density functional dispersion correction (DFT-D) for the 94 elements H-Pu. *J. Chem. Phys.* **2010**, *132* (15).
20. (a) Hay, P. J.; Jeffrey Hay, P.; Wadt, W. R., Ab initio effective core potentials for molecular calculations. Potentials for K to Au including the outermost core orbitals. *J. Chem. Phys.* **1985**, *82* (1), 299-310.(b) Wadt, W. R.; Jeffrey Hay, P., Ab initio effective core potentials for molecular calculations. Potentials for main group elements Na to Bi. *J. Chem. Phys.* **1985**, *82* (1), 284-298.(c) Hay, P. J.; Jeffrey Hay, P.; Wadt, W. R., Ab initio effective core potentials for molecular calculations. Potentials for the transition metal atoms Sc to Hg. *J. Chem. Phys.* **1985**, *82* (1), 270-283.
21. Dunning, T. H., Gaussian basis sets for use in correlated molecular calculations. I. The atoms boron through neon and hydrogen. *J. Chem. Phys.* **1989**, *90* (2), 1007-1023.
22. (a) Friedrichs, M.; Zhou, R.; Edinger, S. R.; Friesner, R. A., Poisson-Boltzmann Analytical Gradients for Molecular Modeling Calculations. *J. Phys. Chem. B* **1999**, *103* (16), 3057-3061.(b) Marten, B.; Kim, K.; Cortis, C.; Friesner, R. A.; Murphy, R. B.; Ringnalda, M. N.; Sitkoff, D.; Honig, B., New Model for Calculation of Solvation Free Energies: Correction of Self-Consistent Reaction Field Continuum Dielectric Theory for Short-Range Hydrogen-Bonding Effects. *J. Phys. Chem.* **1996**, *100* (28), 11775-11788.(c) Edinger, S. R.; Cortis, C.; Shenkin, P. S.; Friesner, R. A., Solvation Free Energies of Peptides: Comparison of Approximate Continuum Solvation Models with Accurate Solution of the Poisson-Boltzmann Equation. *J. Phys. Chem. B* **1997**, *101* (7), 1190-1197.
23. Rashin, A. A.; Honig, B., Reevaluation of the Born model of ion hydration. *J. Phys. Chem.* **1985**, *89* (26), 5588-5593.
24. Ryu, H.; Park, J.; Kim, H. K.; Park, J. Y.; Kim, S.-T.; Baik, M.-H., Pitfalls in Computational Modeling of Chemical Reactions and How To Avoid Them. *Organometallics* **2018**, *37* (19), 3228-3239.

Blakey-Baik-Rh-AllylicCHAmination-Mechanism.docx (2.69 MiB)

[view on ChemRxiv](#) • [download file](#)

---

# Supporting Information

## The Mechanism of Rhodium Catalyzed Allylic C–H Amination

Robert J. Harris,<sup>†</sup> Jiyong Park<sup>‡,§</sup>, Taylor A. F. Nelson,<sup>†</sup> Nafees Iqbal,<sup>‡,§</sup> Daniel C. Salgueiro,<sup>†</sup> John Bacsá,<sup>†</sup>  
Cora MacBeth,<sup>†</sup> Mu–Hyun Baik<sup>\*,§,‡</sup> and Simon B. Blakey<sup>\*,†</sup>

<sup>†</sup>Department of Chemistry, Emory University, Atlanta, GA, 30322, U.S.A.

<sup>‡</sup>Department of Chemistry, Korea Advanced Institute of Science and Technology (KAIST), Daejeon 34141,  
Republic of Korea

<sup>§</sup>Center for Catalytic Hydrocarbon Functionalizations, Institute for Basic Science (IBS), Daejeon 34141,  
Republic of Korea

General Information	3
Experimental Determinations of the Rate Laws	3
<b>Table S1.</b> Initial rates for the rhodium–catalyzed allylic amination of diphenylpropene <b>1</b> with benzylcarbamate <b>2</b>	4
<b>Figure S2.</b> Rhodium concentration dependence for the rate of allylic amination of diphenylpropene ( <b>1</b> ) (0.20 M) with benzylcarbamate ( <b>2</b> ) (0.49 M) catalyzed by a mixture of [RhCp*Cl <sub>2</sub> ] <sub>2</sub> and AgBF <sub>4</sub> in the presence of AgOAc in DCE at 60 °C. A slope of $k_1 = 2.4 \pm 0.4 \times 10^{-4} \text{ s}^{-1}$ was calculated and established a first–order dependence of the rate on rhodium concentration.	5
<b>Figure S6.</b> concentration dependence for rate of allylic amination of <b>1</b> (4.9 M) with <b>2</b> catalyzed by a mixture of [RhCp*Cl <sub>2</sub> ] <sub>2</sub> and AgBF <sub>4</sub> in the presence of AgOAc in DCE at 60 °C. A plot of rate versus [ <b>2</b> ] was nearly linear with a slope of $k_3 = -5.2 \pm 0.6 \times 10^{-5} \text{ s}^{-1}$ .	7
Synthesis and Reactivity of Rhodium Complexes	8
Quantum chemical studies of the Rh catalyzed C–H amination reactions	18
<b>Scheme S2</b> Proposed mechanism for rhodium catalyzed Rh–catalyzed allylic acetylation going through Rh(III)→Rh(I)	19
<b>Figure S7.</b> Energy profile for Rh–catalyzed allylic acetylation going through Rh (III→I)	20
<b>Scheme S3</b> Proposed mechanism for rhodium catalyzed Rh–catalyzed allylic acetylation going through Rh (V)→Rh(III)	20
<b>Figure S8</b> Energy profile for Rh–catalyzed allylic acetylation going through Rh (V→III)	21
<b>Figure S9</b> Energy profile of Ag <sup>+</sup> catalyzed C–O bond activation of <b>4</b>	22
<b>Scheme S4</b> Proposed mechanism of the outer-sphere Rh-catalyzed allylic C–H amination of allylic acetate	22

**Figure S10** Complete energy profile of the outer-sphere Rh-catalyzed amination of allylic acetate 23

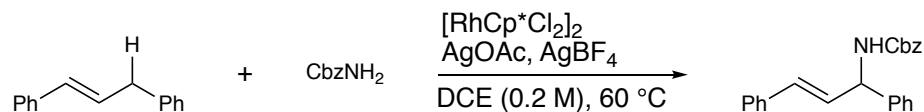
**Table S2** Computed Energy Components for Optimized Structures. Units of energies are kcal/mol, except for that of the SCF electronic energy (E(SCF)) that is in eV. 23

## General Information

Reactions were performed under a nitrogen atmosphere employing standard Schlenk and glovebox techniques using anhydrous solvents unless otherwise specified. Anhydrous tetrahydrofuran (THF), diethyl ether (Et<sub>2</sub>O), and dichloromethane (CH<sub>2</sub>Cl<sub>2</sub>) were obtained by passage through activated alumina using a *Glass Contours* solvent purification system. Anhydrous dichloroethane (CH<sub>2</sub>Cl)<sub>2</sub> was obtained by distillation over calcium hydride and stored over 4 Å molecular sieves. All other reagents were obtained from commercial suppliers and used as received. Analytical thin layer chromatography (TLC) was performed on precoated aluminum backed Silicycle SiliaPure® 0.25 mm silica gel 60 plates. Visualization was accomplished with UV light, ethanolic *p*-anisaldehyde, or aqueous potassium permanganate. Flash column chromatography was performed employing 200-400 mesh silica gel (EM) on a Biotage Isolera One flash chromatography system. NMR spectra were obtained on a Varian spectrometer at 25 °C operating at 400 MHz for <sup>1</sup>H NMR, 125 MHz for <sup>13</sup>C NMR, and 376 MHz for <sup>19</sup>F CDCl<sub>3</sub> unless noted otherwise; <sup>13</sup>C NMR was referenced relative to CDCl<sub>3</sub> (δ = 77.0), <sup>1</sup>H NMR was referenced relative to residual CHCl<sub>3</sub> (δ = 7.26) for CDCl<sub>3</sub> and CHDCl<sub>2</sub> (δ = 5.32) for CD<sub>2</sub>Cl<sub>2</sub>, and <sup>19</sup>F was reported unreference. Chemical shifts (δ values) were reported in parts per million (ppm) and coupling constants (*J* values) in Hz. Multiplicity is indicated using the following abbreviations: s = singlet, d = doublet, t = triplet, q = quartet, qn = quintet, hep = heptet, m = multiplet, b = broad signal). Infrared (IR) spectra were recorded using Thermo Electron Corporation Nicolet 380 FT-IR spectrometer. High resolution mass spectra were obtained using a Thermo Electron Corporation Finigan LTQFTMS (at the Mass Spectrometry Facility, Emory University). All gas chromatograph spectra were taken on an Agilent Technologies 6850 series gas chromatograph equipped with a flame ionization detector and with a HP-1 column (30 m wide bore 0.32mm x 0.25 μm) manufactured by J&W.

## Experimental Determinations of the Rate Laws

### Representative procedure for initial rate kinetic experiments



In a nitrogen filled glove box, benzyl carbamate (194 mg, 1.28 mmol) and silver acetate (180 mg, 1.08 mmol) were added to a 7 mL reaction vial equipped with a magnetic stir bar. Silver tetrafluoroborate (40 mg, 0.2 mmol) and [RhCp\*Cl<sub>2</sub>]<sub>2</sub> (96 mg, 0.3 mmol) were added to two separate 4 mL vials. All three vials were fitted with septum caps and removed from the glove box. Nonane (internal standard, 134.6 mg, 1.05 mmol) was added to a 10 mL volumetric flask followed by the addition of distilled 1,2-dichloroethane to create 0.105 M solution. 2.3 mL of the resulting solution was added to the 7mL reaction vial containing benzyl carbamate and silver acetate. 1 mL of the solution containing the internal standard was added to each of the 4 mL vials containing silver tetrafluoroborate and [RhCp\*Cl<sub>2</sub>]<sub>2</sub> to create stock solutions of silver tetrafluoroborate (0.2 M) and the rhodium catalyst (0.3 M). 1,3-diphenyl propene (0.1 mL, 0.51 mmol) was added via syringe to the 7 mL reaction vial followed by 0.1mL from each of the stock solutions of silver tetrafluoroborate (0.02 mmol) and [RhCp\*Cl<sub>2</sub>]<sub>2</sub> (0.03 mmol). The reaction vial was then placed in a heating block at 60 °C. Placing the vial in the heating block was considered the t=0 time point for kinetic analysis. Reaction progress was monitored by

removing an aliquot of the reaction mixture (~50  $\mu$ L). Each aliquot was taken using a fresh syringe (1mL) and a clean reusable needle. Each sample was worked up by filtering through diatomaceous silica using ethyl acetate as the eluent and then analyzed by gas chromatography equipped with a flame ionization detector.

**Table S1.** Initial rates for the rhodium–catalyzed allylic amination of diphenylpropene **1** with benzylcarbamate **2**

Reaction scheme: Diphenylpropene **1** + Benzylcarbamate **2**  $\xrightarrow[\text{DCE (0.2 M), 60 } ^\circ\text{C}]{[\text{RhCp}^*\text{Cl}_2]_2, \text{AgOAc (2.1 equiv)}, \text{AgBF}_4 \text{ (12 mol \%)}]}$  Product **3**

entry	[Rh] (mM)	[ <b>1</b> ] (M)	[CbzNH <sub>2</sub> ] (M)	Rate (10 <sup>6</sup> × Ms <sup>-1</sup> ) <sup>a</sup>
1	12	0.20	0.49	2.1 ± 0.2
2	12 <sup>b</sup>	0.20	0.49	3.2 ± 0.2
3	12	0.20	0.49	2.3 ± 0.3
4	4 <sup>b</sup>	0.20	0.49	1.2 ± 0.1
5	8	0.20	0.49	1.9 ± 0.2
6	16	0.20	0.49	4.2 ± 0.5
7	12	0.10	0.49	0.34 ± 0.04
8	12	0.40	0.49	4.2 ± 0.3
9	12	0.40	0.49	5.4 ± 0.2
10	12	0.50	0.49	7.7 ± 0.9
11	12	0.50	0.49	6.5 ± 0.2
12	12	0.20	0.25	4.7 ± 0.8
13	12	0.20	0.25	4.5 ± 0.2
14	12	0.20	0.40	3.5 ± 0.4
15	12	0.20	0.74	1.0 ± 0.1
16	12	0.20	0.79	0.91 ± 0.05
17	12	0.20	0.99	0.44 ± 0.09
18	12	0.20	1.1	0.31 ± 0.03

<sup>a</sup>Errors represent 1 standard deviation obtained by least square analysis and do not reflect systematic experimental errors <sup>b</sup>4 mol % AgBF<sub>4</sub> was used.

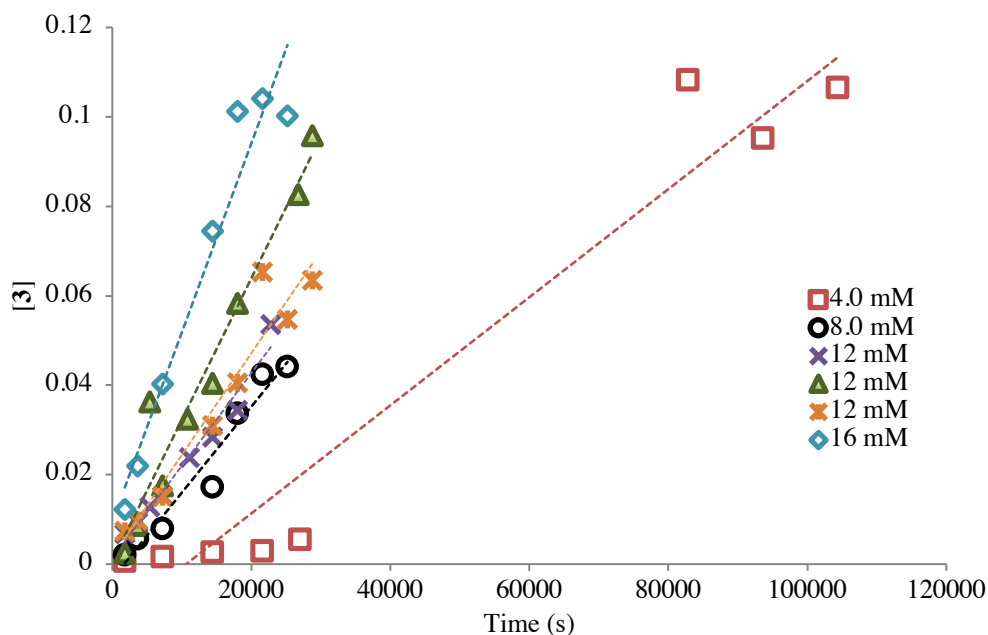


**Figure S1.** Initial rate plots for the allylic amination of diphenylpropene (**1**) (0.20 M) with benzyl carbamate (**2**) (0.50M) catalyzed by a mixture of  $[\text{RhCp}^*\text{Cl}_2]_2$  ( $[\text{Rh}] = 4.0\text{--}16\text{ mM}$ ) and  $\text{AgBF}_4$  (24 mM) in the presence of  $\text{AgOAc}$  (0.42 M). For  $[\text{Rh}] = 4.0$  and  $8.0\text{ mM}$  a reduced amount of  $\text{AgBF}_4$  (8.0 mM) was used; however, since the abstraction of  $\text{Cl}^-$  is much faster than the oxidation of Rh, the excess  $\text{AgOAc}$  can also serve to abstract the  $\text{Cl}^-$  once a small amount of acetic acid has been generated.

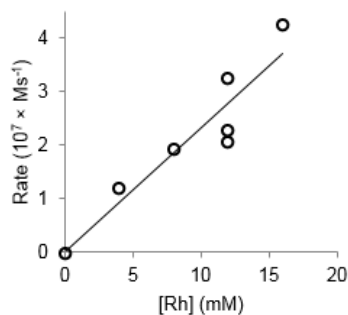


**Figure S2.** Rhodium concentration dependence for the rate of allylic amination of diphenylpropene (**1**) (0.20 M) with benzylcarbamate (**2**) (0.49 M) catalyzed by a mixture of  $[\text{RhCp}^*\text{Cl}_2]_2$  and  $\text{AgBF}_4$  in the presence of  $\text{AgOAc}$  in DCE at  $60\text{ }^\circ\text{C}$ . A slope of  $k_1 = 2.4 \pm 0.4 \times 10^{-4}\text{ s}^{-1}$  was calculated and established a first-order dependence of the rate on rhodium concentration.



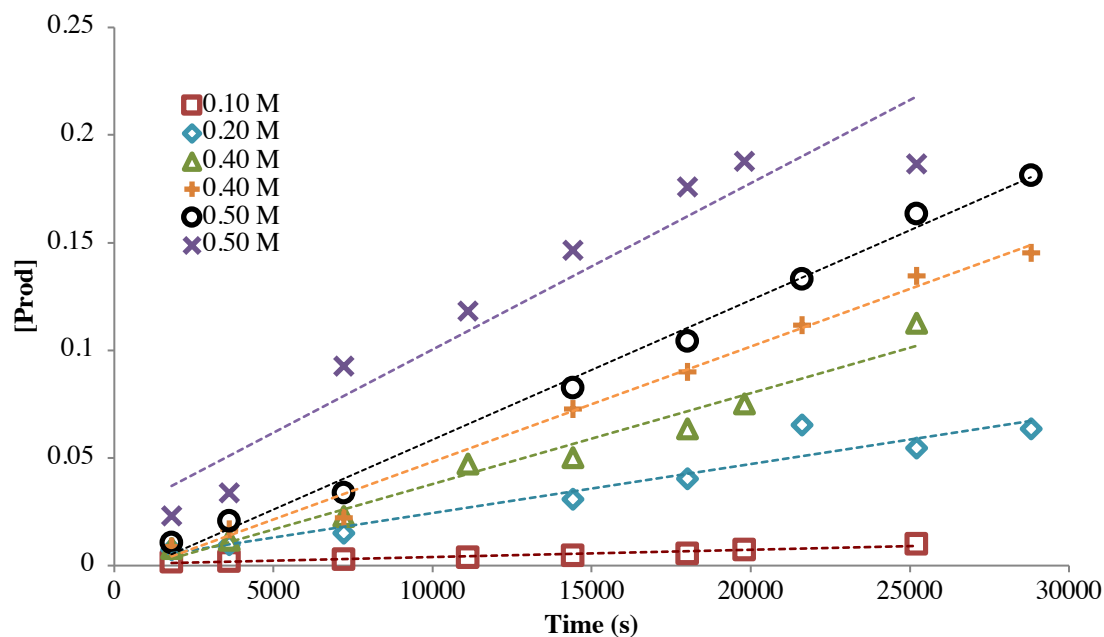


**Figure S3.** Initial rate plots for the allylic amination of diphenylpropene (**1**) (0.10 – 0.50 M) with benzyl carbamate (**2**) (0.49M) catalyzed by a mixture of  $[\text{RhCp}^*\text{Cl}_2]_2$  ( $[\text{Rh}] = 12 \text{ mM}$ ) and  $\text{AgBF}_4$  (24 mM) in the presence of  $\text{AgOAc}$  (0.42 M).

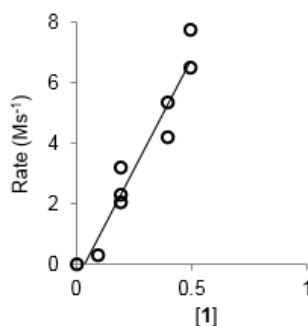


**Figure S4.** Concentration dependence for the rate of allylic amination of diphenylpropene (**1**) with benzylcarbamate (**2**) (0.49 M) catalyzed by a mixture of  $[\text{RhCp}^*\text{Cl}_2]_2$  and  $\text{AgBF}_4$  in the presence of  $\text{AgOAc}$  in DCE at 60 °C. A plot of rate versus  $[\mathbf{1}]$  was linear with a slope of  $k_2 = 1.5 \pm 0.1 \times 10^{-5} \text{ s}^{-1}$ .

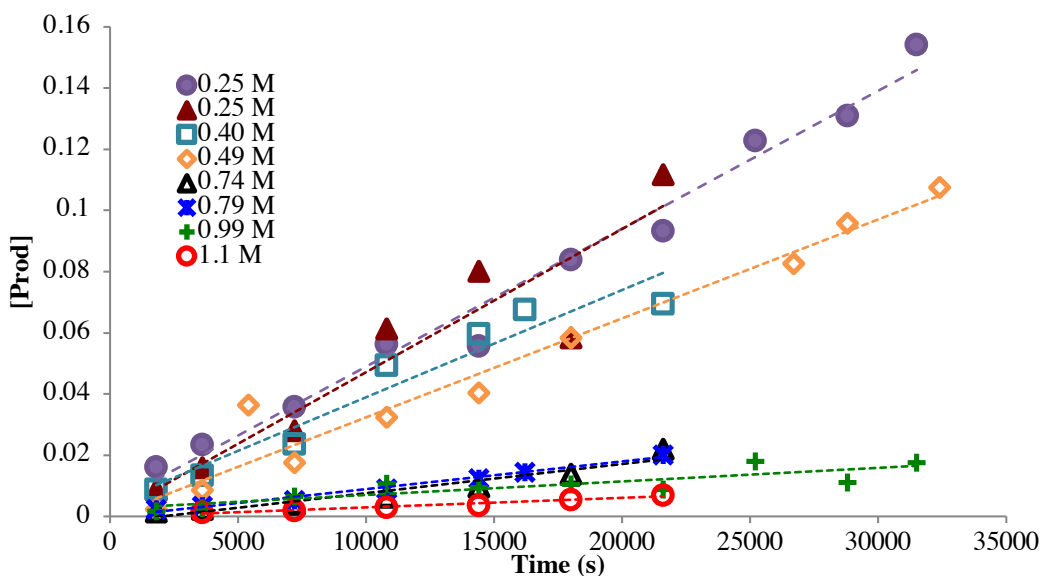


**Figure S5.** Initial rate plots for the allylic amination of diphenylpropene (**1**) (0.20 M) with benzyl carbamate (**2**) (0.25 – 1.1 M) catalyzed by a mixture of  $[\text{RhCp}^*\text{Cl}_2]_2$  ( $[\text{Rh}] = 12 \text{ mM}$ ) and  $\text{AgBF}_4$  (24 mM) in the presence of  $\text{AgOAc}$  (0.42 M). For  $[\text{CbzNH}_2] = 0.49 \text{ M}$  a reduced amount of  $\text{AgBF}_4$  (8.0 mM) was used; however, since the abstraction of  $\text{Cl}^-$  is much faster than the oxidation of Rh, the excess  $\text{AgOAc}$  can also serve to abstract the  $\text{Cl}^-$  once a small amount of acetic acid has been generated.

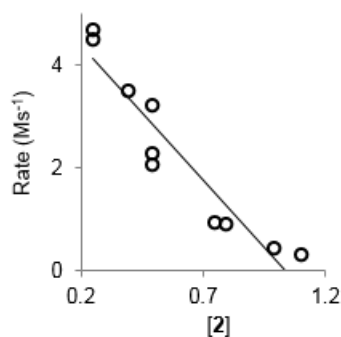
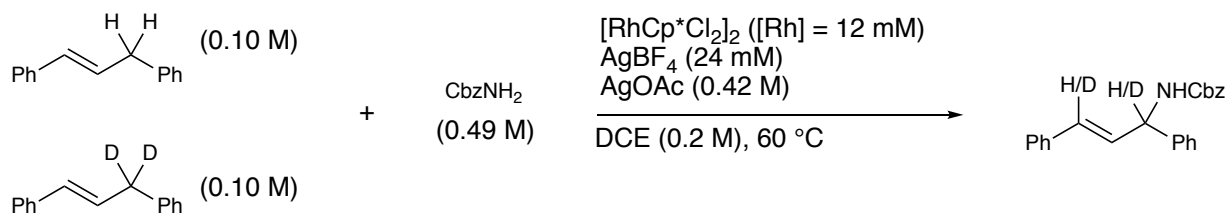


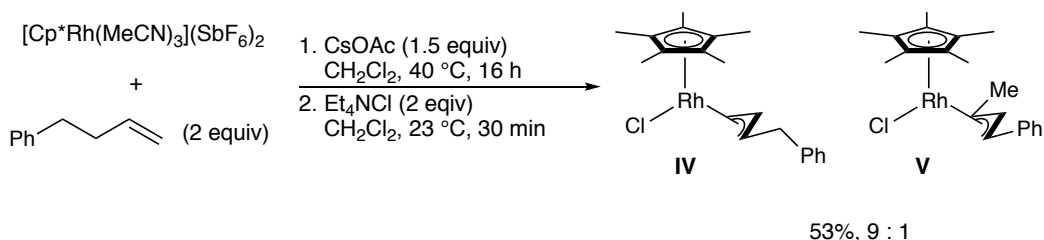
**Figure S6.** concentration dependence for rate of allylic amination of **1** (4.9 M) with **2** catalyzed by a mixture of  $[\text{RhCp}^*\text{Cl}_2]_2$  and  $\text{AgBF}_4$  in the presence of  $\text{AgOAc}$  in DCE at 60 °C. A plot of rate versus  $[\mathbf{2}]$  was nearly linear with a slope of  $k_3 = -5.2 \pm 0.6 \times 10^{-5} \text{ s}^{-1}$ .

## Determination of KIE



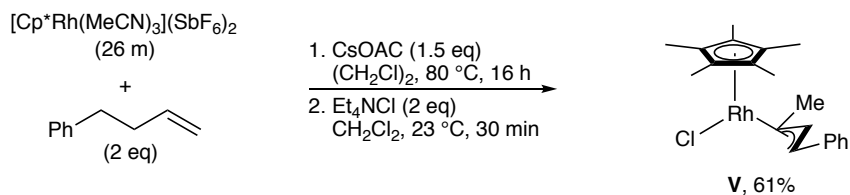
In a nitrogen filled glove box, [RhCp\*Cl<sub>2</sub>]<sub>2</sub> (9.9 mg, 0.016 mmol), Silver tetrafluoroborate (12 mg, 0.069 mmol), benzyl carbamate (194.5 mg, 1.29 mmol), and silver acetate (180 mg, 1.10 mmol) were added to a 7 mL reaction vial equipped with a magnetic stir bar. The vial was fitted with a septum cap and removed from the glove box. In a separate vial, 100  $\mu$ L each of diphenylpropene (**1**) and **1- $d_2$**  were added. A <sup>1</sup>H NMR of the resulting mixture of **1** and **1- $d_2$**  was obtained to determine a 1.05:1 mixture of **1**:**1- $d_2$** . Dichloroethane (2.6 mL) and the mixture of diphenylpropene (101.2 mg) were added to the reaction vial via syringe and the resulting mixture was mixed thoroughly and stirred at 60 °C for 2 h. After 2 h the reaction was stopped by filtering through silica gel and eluting with EtOAc.

## Synthesis and Reactivity of Rhodium Complexes



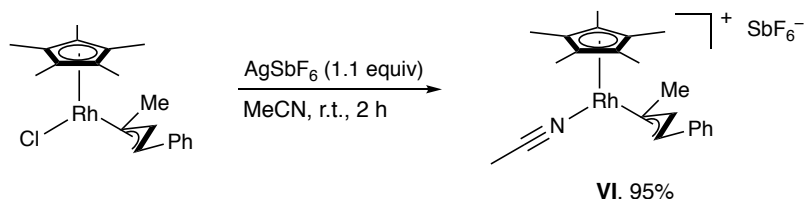
### Chloro-( $\eta^3$ -1-benzylallyl)-( $\eta^5$ -pentamethylcyclopentadienyl)-rhodium, (**IV**).

[Cp\*Rh(MeCN)<sub>3</sub>](SbF<sub>6</sub>)<sub>2</sub> (650 mg, 0.78 mmol) and CsOAc (243 mg, 1.27 mmol) were added to a 100 mL oven-dried round bottom flask charged with a magnetic stir bar in a glove box. The flask was capped with a rubber septum and removed from the glovebox. Dichloromethane (30 mL) and 1-phenylbutene (250  $\mu$ L, 1.66 mmol) were added via syringe, and the reaction was stirred at 40 °C for 16 h. After 16 h, the reaction was cooled to room temperature. NEt<sub>4</sub>Cl (300 mg, 1.81 mmol) was dissolved in dichloromethane (3 mL) and the resulting solution was added to the reaction via syringe and allowed to stir for 30 min. The reaction mixture was then filtered through celite, eluted with dichloromethane, and concentrated under reduce pressure. The resulting solid was chromatographed (Hexanes-EtOAc = 9:1 to 7:3) to give **IV** and **V** as a red solid in a 9:1 ratio (53%). The two isomers could be separated by column chromatography to yield **IV** cleanly. <sup>1</sup>H NMR (CDCl<sub>3</sub>, 400 MHz):  $\delta$  7.37 (d,  $J$  = 7.5 Hz, 2H), 7.30 (t,  $J$  = 7.6 Hz, 2H), 7.20 (t,  $J$  = 7.3 Hz, 1H), 4.08 (tdd,  $J$  = 10.9, 6.9, 2.0 Hz, 1H), 3.67 (td,  $J$  = 9.6, 6.0 Hz, 1H), 3.35-3.27 (m, 2H), 3.05-2.96 (m, 2H), 1.71 (s, 14H). HRMS (ESI): calcd (found) for C<sub>20</sub>H<sub>26</sub>ClRh (M<sup>+</sup>): 404.07781 (404.07783).



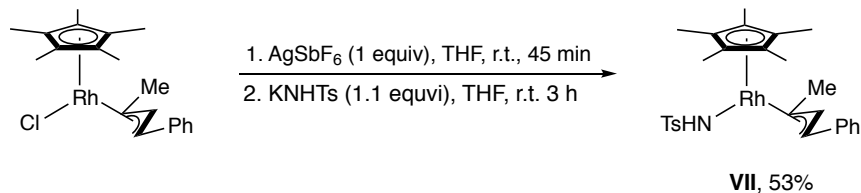
**Chloro-( $\eta^3$ -1-methyl-3-phenylallyl)-( $\eta^5$ -pentamethylcyclopentadienyl)-rhodium, (V).**

$[\text{Cp}^*\text{Rh}(\text{MeCN})_3](\text{SbF}_6)_2$  (650 mg, 0.78 mmol) and  $\text{CsOAc}$  (243 mg, 1.27 mmol) were added to a 100 mL oven-dried round bottom flask charged with a magnetic stir bar in a glove box. The flask was capped with a rubber septum and removed from the glovebox. Dichloroethane (30 mL) and 1-phenylbutene (250  $\mu\text{L}$ , 1.66 mmol) were added via syringe, and the reaction was stirred at 80 °C for 16 h. After 16 h, the reaction was cooled to room temperature.  $\text{NEt}_4\text{Cl}$  (300 mg, 1.81 mmol) was dissolved in dichloromethane (3 mL) and the resulting solution was added to the reaction via syringe and allowed to stir for 30 min. The reaction mixture was then filtered through celite, eluted with dichloromethane, and concentrated under reduce pressure. The resulting solid was chromatographed (Hexanes-EtOAc = 9:1 to 7:3) to give **I** as a red solid (61%).  $^1\text{H}$  NMR ( $\text{CDCl}_3$ , 400 MHz):  $\delta$  7.33-7.29 (m, 4 H), 7.22-7.16, (m, 1 H), 4.67 (d,  $J = 10.7$ , 1 H), 4.55 (td,  $J_{\text{HH}} = 11.1$  Hz,  $J_{\text{RhH}} = 2.0$ , 1 H), 3.73(dq,  $J = 10.7$ , 6.3 Hz, 1 H), 1.69 (d,  $J = 6.3$  Hz, 3 H), 1.35 (s, 15 H).  $^{13}\text{C}\{^1\text{H}\}$  NMR ( $\text{CDCl}_3$ , 125 MHz):  $\delta$  139.0, 128.7, 126.1, 126.0, 97.8 (d,  $J_{\text{RhC}} = 6.8$  Hz), 89.0 (d,  $J_{\text{RhC}} = 6.3$  Hz), 77.3 (d,  $J_{\text{RhC}} = 7.3$  Hz), 58.4 (d,  $J_{\text{RhC}} = 10.9$  Hz), 8.6. HRMS (ESI): calcd (found) for  $\text{C}_{20}\text{H}_{26}\text{ClRh}$  ( $\text{M}^+$ ): 404.07781 (404.07783).



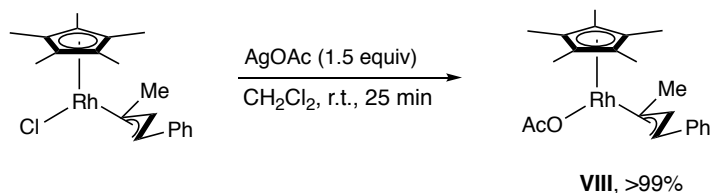
**[( $\eta^3$ -1-methyl-3-phenylallyl)-( $\eta^5$ -pentamethylcyclopentadienyl)-rhodium acetonitrile] hexafluoroanimonate, (VI).**

Complex **V** (87.5 mg, 0.22 mmol) and  $\text{AgSbF}_6$  (83 mg, 0.24 mmol) were suspended in MeCN inside a glovebox. The reaction was capped, removed from box, and stirred at room temperature for 2h. The resulting mixture was filtered through celite, eluted with  $\text{CH}_2\text{Cl}_2$ , and concentrated under reduced pressure. The resulting solid was crystalized by layer hexanes on top of dichloromethane. The supernant was decanted, and the solids were washed with hexanes (x 3). The resulting solids were redissolved in dichloromethane and filtered through celite to remove any remaining silver. The resulting yellow-orange solution was concentrated under reduced pressure to afford a yellow-orange solid.  $^1\text{H}$  NMR ( $\text{CDCl}_3$ , 400MHz):  $\delta$  7.39 (t,  $J = 7.7$  Hz, 2 H), 7.31-7.29 (m, 3 H), 4.61 (td,  $J_{\text{HH}} = 11.0$  Hz,  $J_{\text{RhH}} = 1.6$ , 1 H), 4.24 (d,  $J = 11.2$ , 1 H), 3.42(dq,  $J = 11.2$ , 5.8 Hz, 1 H), 2.48 (s, 3 H), 1.76 (d,  $J = 6.3$  Hz, 2 H), 1.38 (s, 15 H).  $^{13}\text{C}\{^1\text{H}\}$  ( $\text{CDCl}_3$ , 125 MHz):  $\delta$  137.0, 129.3, 127.4, 126.7, 124.8 (d,  $J_{\text{RhC}} = 7.6$  Hz), 99.6(d,  $J_{\text{RhC}} = 6.5$  Hz), 90.6 (d,  $J_{\text{RhC}} = 5.7$  Hz), 75.5 (d,  $J_{\text{RhC}} = 7.0$  Hz), 72.0 (d,  $J_{\text{RhC}} = 8.5$  Hz), 18.1, 8.2, 3.4. HRMS (ESI): calcd (found) for  $\text{C}_{22}\text{H}_{29}\text{NRh}$  ( $\text{M}-\text{SbF}_6$ ): 410.13550 (410.13517).



**[( $\eta^3$ -1-methyl-3-phenylallyl)-( $\eta^5$ -pentamethylcyclopentadienyl)-rhodium tosylamide], (**VII**).**

Complex **V** (202.4 mg, 0.5 mmol) and  $\text{AgSbF}_6$  (171.8 mg, 0.5 mmol) were suspended in THF (15 mL) inside a glovebox. The reaction was stirred for 45 min at room temperature. Potassium tosylamide (KNHTs, 106.7 mg, 0.55 mmol) was added the reaction as a solid. The reaction was capped, removed from box, and stirred at room temperature for 3 hours. The resulting mixture was filtered through celite, eluted with  $\text{CH}_2\text{Cl}_2$ , and concentrated under reduced pressure. The resulting solid was redissolved in 2 mL  $\text{CH}_2\text{Cl}_2$ . 6 ml of hexanes were added to the DCM solution and concentrated under reduced pressure until solids began to crash out. The solids were collected via vacuum filtration and resulted in a 10:1 mixture of the product (**VII**) : starting material (**V**). This mixture was further purified by dissolving in  $\text{Et}_2\text{O}$  and concentrating until solids began to precipitate. The resulting  $\text{Et}_2\text{O}$  suspension was and further **VII** precipitated. The solids were collected by vacuum filtration and washed with pentane to afford **VII** as an orange powder in 53% yield (145 mg).  $^1\text{H}$  NMR ( $\text{CDCl}_3$ , 400MHz):  $\delta$  7.64 (d,  $J$  = 8.2 Hz, 2H), 7.41 (d,  $J$  = 7.3 Hz, 2H), 7.29 (t,  $J$  = 7.7 Hz, 2H), 7.17(t,  $J$  = 7.4 Hz, 1H), 7.10 (d,  $J$  = 7.9 Hz, 2H), 4.45 (td,  $J_{\text{HH}}$  = 10.6 Hz,  $J_{\text{RhH}}$  = 1.8 Hz, 1H), 4.32 (d,  $J$  = 11.1 Hz, 1H), 3.20 (dq,  $J$  = 10.9, 5.7 Hz, 1H), 2.30 (s, 3H), 1.63 (d,  $J$  = 6.4 Hz, 3H), 1.38 (s, 15H).  $^{13}\text{C}\{^1\text{H}\}$  NMR ( $\text{CDCl}_3$ , 125 MHz):  $\delta$  146.67, 139.70, 139.65, 128.79, 128.69, 126.61, 125.96, 125.44, 97.52 (d,  $J_{\text{RhC}}$  = 5.9 Hz), 89.32 (d,  $J_{\text{RhC}}$  = 6.2 Hz), 72.40 (d,  $J_{\text{RhC}}$  = 8.6 Hz), 69.68 (d,  $J_{\text{RhC}}$  = 9.6 Hz), 21.22, 18.32, 8.60. HRMS (ESI): calcd (found) for  $\text{C}_{27}\text{H}_{35}\text{O}_2\text{NRhS}$  ( $\text{MH}^+$ ): 540.14435 (540.14417).

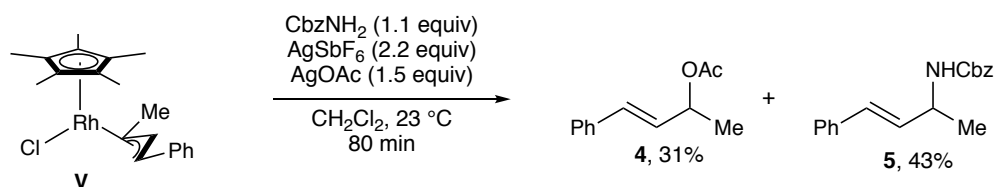


**[( $\eta^3$ -1-methyl-3-phenylallyl)-( $\eta^5$ -pentamethylcyclopentadienyl)-rhodium acetate], (**VII**).**

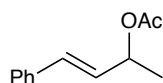
Complex **V** (100 mg, 0.25 mmol) and  $\text{AgOAc}$  (61.8, 0.37 mmol) were suspended in  $\text{CH}_2\text{Cl}_2$  (10 mL) inside a glovebox. The reaction was capped, removed from the glove box, and stirred at room temperature for 25 min. The resulting mixture was filtered through celite, eluted with  $\text{CH}_2\text{Cl}_2$ , and concentrated under reduced pressure to afford complex **VIII** as a red powder in quantitative yield (105.3 mg)  $^1\text{H}$  NMR ( $\text{CDCl}_3$ , 400MHz):  $\delta$  7.56 (d,  $J$  = 7.5 Hz, 2H), 7.30 (t,  $J$  = 7.5 Hz, 2H), 7.17 (t,  $J$  = 7.4 Hz, 1H), 4.58 (t,  $J$  = 10.8 Hz, 1H), 4.24 (d,  $J$  = 11.2 Hz, 1H), 3.04 (dq,  $J$  = 11.1, 5.7 Hz, 1H), 1.96 (s, 3H), 1.78 (d,  $J$  = 6.3 Hz, 3H), 1.31 (s, 15H).  $^{13}\text{C}\{^1\text{H}\}$  NMR ( $\text{CDCl}_3$ , 125 MHz):  $\delta$  176.6, 139.8, 128.4, 127.1, 125.9, 96.4 (d,  $J_{\text{RhC}}$  = 6.8 Hz), 90.6 (d,  $J_{\text{RhC}}$  = 6.4 Hz), 76.0 (d,  $J_{\text{RhC}}$  = 8.7 Hz), 74.0 (d,  $J_{\text{RhC}}$  = 9.5 Hz), 25.7, 18.3, 8.4. HRMS (ESI): calcd (found) for  $\text{C}_{22}\text{H}_{329}\text{O}_2\text{NRh}$  ( $\text{M}^+$ ): 428.12226 (428.12275).

## VII. Reactivity of Rhodium $\pi$ -allyl complexes

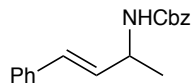
Reactions of Complex **V** with a halide abstractor, silver oxidant, and base



Complex **V** (20.4 mg, 0.05 mmol),  $\text{CbzNH}_2$  (8.8 mg, 0.058 mmol),  $\text{AgSbF}_6$  (38.8 mg, 0.11 mmol), and  $\text{AgOAc}$  (13.9 mg, 0.08 mmol) were dissolved in  $\text{CH}_2\text{Cl}_2$  (2 mL) under  $\text{N}_2$  and stirred at room temperature for 80 min. The reaction was monitored by TLC for consumption of **V**. After consumption of **V** was observed (80 min), the reaction was filtered through celite, eluted with  $\text{CH}_2\text{Cl}_2$ , and concentrated under reduced pressure. The remaining residue was purified by column chromatography (Hexanes:EtOAc, 10:0 to 8:2) to afford allylic acetate **4** in 31% yield and allylic carbamate **5** in 43% yield.

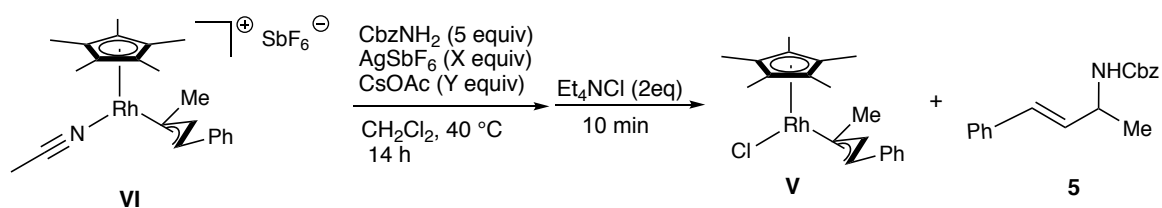


**Allylic acetate (4):**  $^1\text{H}$  NMR ( $\text{CDCl}_3$ , 400 MHz):  $\delta$  7.38 (d,  $J = 7.6$  Hz, 2H), 7.32 (t,  $J = 7.4$  Hz, 2H), 7.27-7.24 (m, 1H), 6.60 (d,  $J = 15.9$  Hz, 1H), 6.19 (dd,  $J = 16.0, 6.8$  Hz, 1H), 5.52 (quintet,  $J = 6.6$  Hz, 1H), 2.08 (s, 3H), 1.41 (d,  $J = 6.5$  Hz, 4H).<sup>8</sup>



**Allylic carbamate (5):**  $^1\text{H}$  NMR ( $\text{CDCl}_3$ , 400 MHz):  $\delta$  7.37-7.28 (m, 9H), 7.25-7.21 (m, 1H), 6.51 (d,  $J = 16.0$  Hz, 1H), 6.16 (dd,  $J = 15.0, 5.8$  Hz, 1H), 5.13 (3, 2H), 4.77 (bs, 1H), 4.49 (bs, 1H), 1.34 (d,  $J = 6.8$  Hz, 4H).<sup>9</sup>

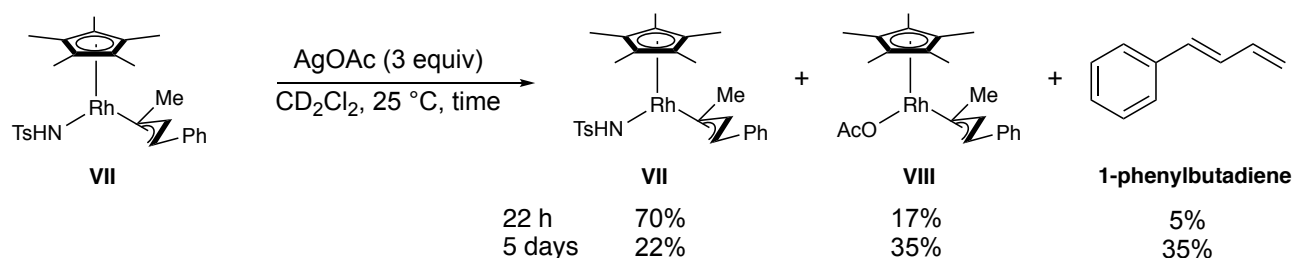
**Reactions of Complex VI** in the presence and absence of AgSbF<sub>6</sub> and CsOAc.



Complex **VI** (33.3 mg, 0.05 mmol), CbzNH<sub>2</sub> (37.8 mg, 0.25 mmol), AgSbF<sub>6</sub> (0–34.7 mg, 0–0.1 mmol), and CsOAc (0–19.2 mg, 0–0.1 mmol) were dissolved in CH<sub>2</sub>Cl<sub>2</sub> (2 mL) under N<sub>2</sub> and stirred at 40 °C. The reaction was monitored by TLC by removing small aliquots with a microliter syringe, adding the aliquot to a solution of NEt<sub>4</sub>Cl, and monitoring for the chloro-complex **V**. In all cases, reactions were not complete with in 2 h and were left overnight for 14 h at which point the reactions were quenched with NEt<sub>4</sub>Cl, filtered through celite, eluted with CH<sub>2</sub>Cl<sub>2</sub>, and concentrated under reduced pressure. The remaining residue was purified by column chromatography (Hexanes:EtOAc, 10:0 to 8:2) to afford allylic carbamate **5** and/or chloro-complex **V**.

entry	AgSbF <sub>6</sub> (equiv)	CsOAc (equiv)	% yield <b>V</b>	% yield <b>5</b>
1	0	0	92%	0%
2	2	0	0%	7%
3	0	2	30%	0%
4	2	2	0%	29%

**Reactions of Complex VII in the presence of a silver oxidant.**



Complex **VII** (8.3 mg, 0.015) and AgOAc (7.5 mg, 0.045 mmol) were added to an NMR tube and the tube was capped with a septum in a glovebox. CD<sub>2</sub>Cl<sub>2</sub> (0.6 mL) and a solution of dinitrobenzene in CD<sub>2</sub>Cl<sub>2</sub> (internal standard, 0.32 M, 20  $\mu$ L, 0.006 mmol) were added to the NMR tube via syringe. A <sup>1</sup>H NMR spectrum was acquired immediately and treated as t=0. After 22 h, 1-phenylbutadiene was observed in 5% yield, acetate complex **VIII** was observed in 17% yield, and 70% of complex **VII** remained unreacted. After 5 days, 1-phenylbutadiene was observed in 35% yield, acetate complex **VIII** was observed in 35% yield, and 22% of complex **VII** remained unreacted.

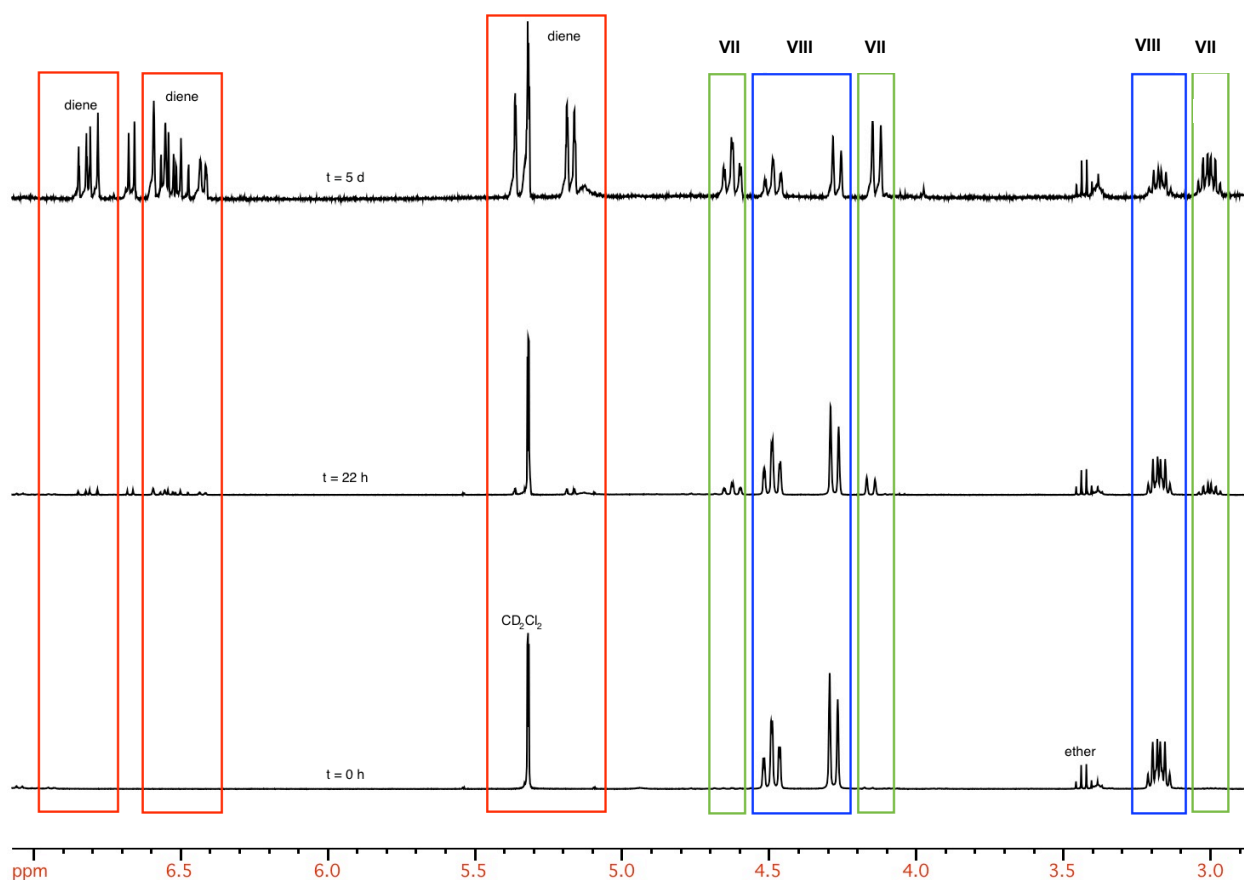
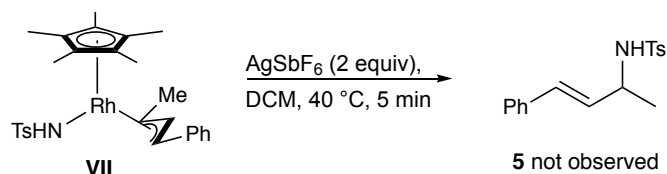


**Figure S7.** <sup>1</sup>H-NMR spectra of the reaction between complex **VII** (24 mM) and AgOAc (72 mM).





Complex **VII** (27.0 mg, 0.05 mmol) and AgSbF<sub>6</sub> (37.8 mg, 0.11 mmol) were dissolved in CH<sub>2</sub>Cl<sub>2</sub> (2.0 mL) under N<sub>2</sub> and stirred at 40 °C. The reaction was monitored by TLC by removing small aliquots with a microliter syringe, diluting with CH<sub>2</sub>Cl<sub>2</sub>, washing with 1 N HCl (aq) and monitoring for the chloro-complex **IX**. After 5 min, complex **IX** was not observed by TLC. The reaction was filtered through celite and concentrated under reduced pressure. Allylic amine **5** was not observed by crude <sup>1</sup>H NMR.

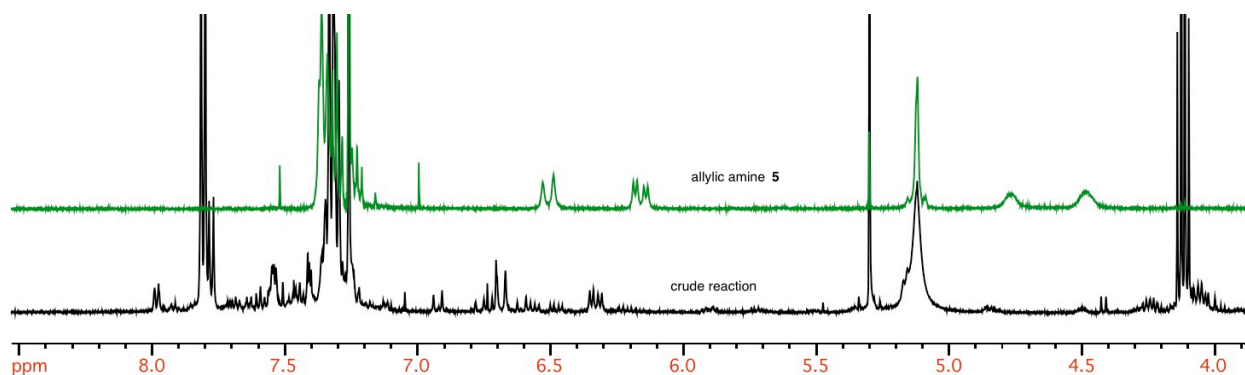
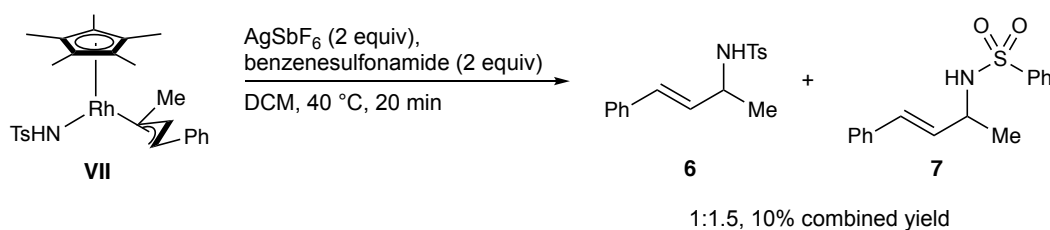
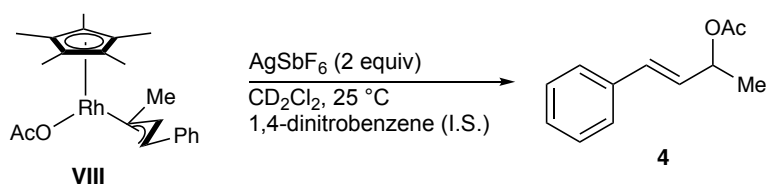


**Figure S8.** <sup>1</sup>H-NMR spectrum of the crude reaction mixture between complex **XII** (25 mM) and AgSbF<sub>6</sub> (55 mM) with a <sup>1</sup>H-NMR spectrum of an authentic sample of allylic amine **5** overlaid.



Complex **VII** (26.7 mg, 0.05 mmol), AgSbF<sub>6</sub> (38.1 mg, 0.11 mmol), and benzenesulfonamide (17.1, 0.11 mmol) were dissolved in CH<sub>2</sub>Cl<sub>2</sub> (2.0 mL) under N<sub>2</sub> and stirred at 40 °C. The reaction was monitored by TLC by removing small aliquots with a microliter syringe, diluting with CH<sub>2</sub>Cl<sub>2</sub>, washing with 1 N HCl (aq) and monitoring for the chloro-complex **V**. After 20 min, complex **V** was not observed by TLC. The reaction was filtered through celite and concentrated under reduced pressure. The residue was purified by column chromatography (Hexanes:EtOAc, 10:0 to 8:2) to afford allylic sulfonamides **5** and **7** in a 1:1.5 ratio and a combined 10% yield.

**Reaction of Complex VIII** in the presence of an oxidant.



Time	Yield
5 min	50%
20 min	70%

Complex **VIII** (6.7 mg, 0.016 mmol) and AgOAc (11.9 mg, 0.035 mmol) were added to an NMR tube and the tube was capped with a septum in a glovebox.  $\text{CD}_2\text{Cl}_2$  (0.6 mL) and a solution of dinitrobenzene in  $\text{CD}_2\text{Cl}_2$  (internal standard, 0.32 M, 20  $\mu\text{L}$ , 0.006 mmol) were added to the NMR tube via syringe. A  $^1\text{H}$  NMR spectrum was acquired after 5 min allylic acetate **4** was observed in 50% yield. After 20 min, full consumption of complex **VIII** was observed and allylic acetate **4** was observed in 70% yield.

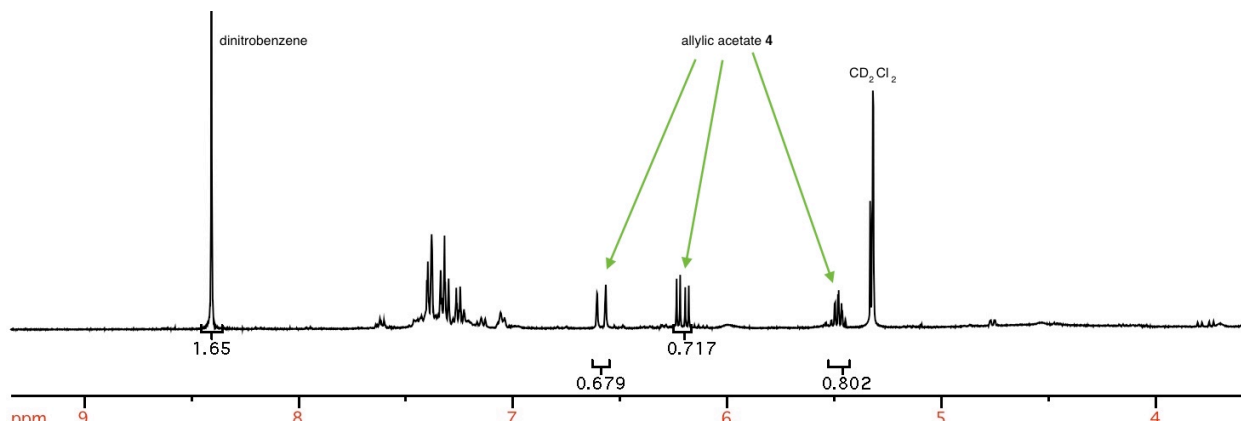
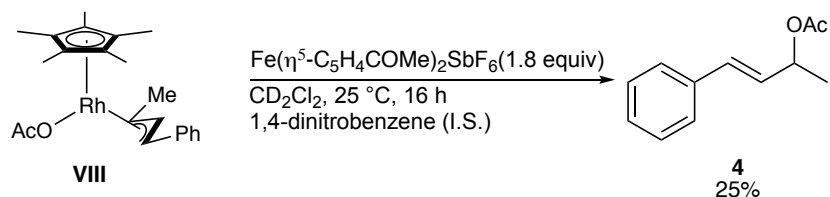


**Figure S9.**  $^1\text{H}$ -NMR spectrum of the reaction between complex **VIII** (26 mM) and  $\text{AgSbF}_6$  (56 mM) after 20 min at room temperature.



Complex **VIII** (7.7 mg, 0.018 mmol) and  $\text{Fe}(\eta^5\text{-C}_5\text{H}_4\text{COMe})_2\text{SbF}_6$  (16.4 mg, 0.032 mmol) were added to an NMR tube and the tube was capped with a septum in a glovebox. Dinitrobenzene (5.1 mg, 0.03 mmol) was dissolve in  $\text{CD}_2\text{Cl}_2$  (2.8 mL) resulting in a 11 mM solution. 0.6 mL of the resulting solution were added to the NMR tube via syringe. A  $^1\text{H}$  NMR spectra at 5 min and 1 h were broadened due to the paramagnetic ferrocenium salt. After 16 H, the ferrocenium was completely consumed, and allylic acetate **4** was observed in 25% NMR yield.

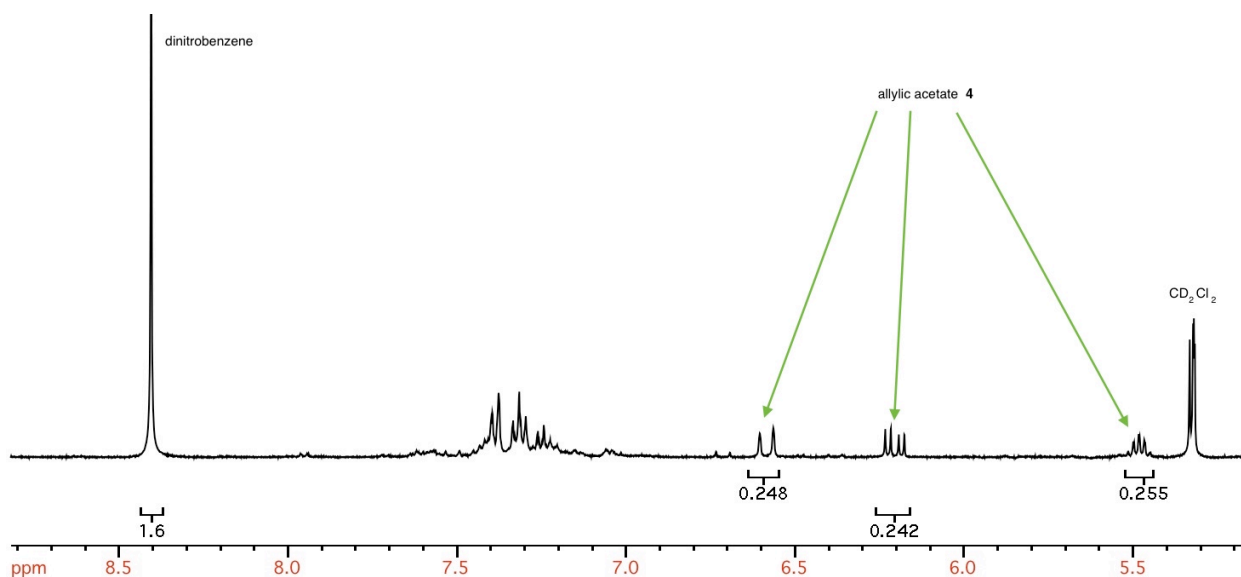
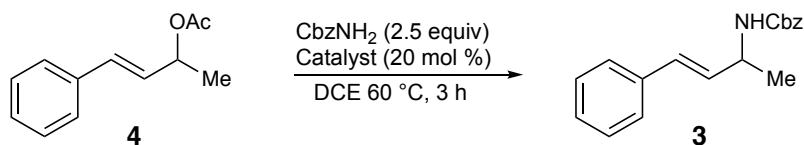


**Figure S10.**  $^1\text{H}$ -NMR spectrum of the reaction between complex **VIII** (30 mM) and  $\text{Fe}(\eta^5\text{-C}_5\text{H}_4\text{COMe})_2\text{SbF}_6$  (53 mM) after 16 h at room temperature.

### VIII. Reactivity of allylic acetate **4**



Benzyl carbamate (75.6 mg, 0.5 mmol) and the catalyst (0.04 mmol) were added to a vial equipped with a stir bar and capped with a septum in side a glove box. The vial was removed from the box, dichloroethane (1 mL) was added via syringe and the vial was heated to 60 °C for five minutes. After equilibration, the allylic acetate **4** (37.5  $\mu$ L, d = 1.02 g/mL, 0.2 mmol) was added via syringe, and the reaction was monitored by TLC. After 100 min, starting material was still present in all cases, but a new spot was observed for all reactions with a catalyst present. After 3 h, no discernable change was noticed by TLC from the 100 min time point. The reactions were stopped by filtering through celite and concentrating under reduced pressure. Crude <sup>1</sup>H NMR showed no conversion for the reaction with no catalyst, and complete consumption of the allylic acetate for all reactions with a catalyst present. The reaction mixture was purified by column chromatography (Hexanes:EtOAc, 10:0 to 8:2) to afford the allylic carbamate **3**.

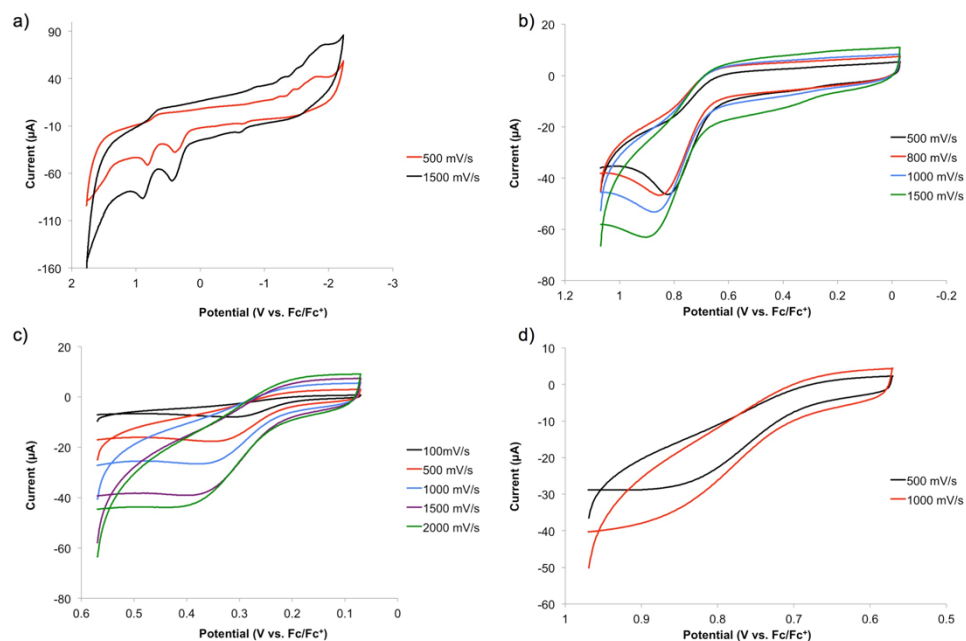
entry	Catalyst	Yield of <b>3</b>
1	–	0%
2	AgSbF <sub>6</sub>	91%
3	AgBF <sub>4</sub>	76%
4	[RhCp*Cl <sub>2</sub> ] <sub>2</sub> /AgSbF <sub>6</sub> <sup>a</sup>	73%
5	[RhCp*(NCMe) <sub>3</sub> ](SbF <sub>6</sub> ) <sub>2</sub>	84%

<sup>a</sup>A mixture of [RhCp\*Cl<sub>2</sub>]<sub>2</sub> (0.022 mmol) and AgSF<sub>6</sub> (0.04 mmol) was stirred in DCE for 30 min before the addition of **4**.

### Cyclic Voltammetry of XIII

#### General procedure for Cyclic Voltammetry Experiments

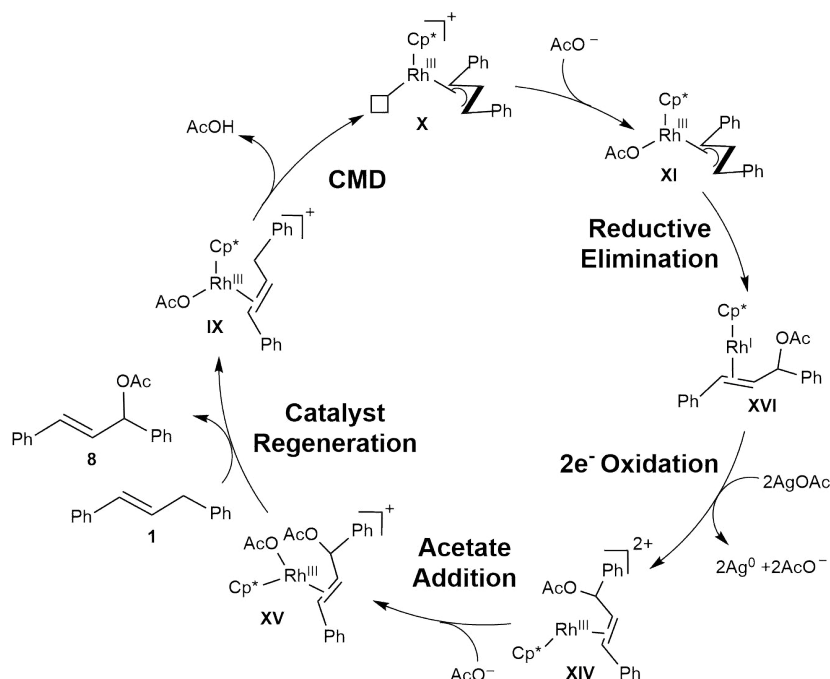
Cyclic voltammetry of **VIII** was performed in a 3-electrode cell consisting of a 3mm glassy carbon disc working electrode, a Ag/Ag<sup>+</sup> reference electrode with a Ag wire in a fritted chamber containing a solution of AgNO<sub>3</sub> (0.01 M) and *n*Bu<sub>4</sub>PF<sub>6</sub> (0.1 M) in CH<sub>2</sub>Cl<sub>2</sub> and a Pt wire counter electrode at room temperature inside a N<sub>2</sub> filled glovebox. A solution of **VIII** (0.001 M) and *n*Bu<sub>4</sub>PF<sub>6</sub> (0.1 M) in CH<sub>2</sub>Cl<sub>2</sub> was added to the electrochemical cell. Cyclic voltammetry scans were taken at selected scan rates (100 mV/s to 2000 mV/s) in the selected potential window. The cyclic voltammograms of **VIII** were referenced to Fc/Fc<sup>+</sup> redox couple (Note: The redox potentials reported in this manuscript are determined using Fc/Fc<sup>+</sup> as an external standard.)



**Figure S2.** Cyclic voltammogram of **XIII** recorded at room temperature in  $\text{CH}_2\text{Cl}_2$  (0.10 M  $n\text{-Bu}_4\text{NPF}_6$ ). a) and b) Two irreversible electrochemical responses are observed  $E^1_{1/2} = \sim 0.42$  V and  $E^2_{1/2} = \sim 0.85$  V. c) Scan rate dependence of  $E^1_{1/2}$ . d) Scan rate dependence of  $E^2_{1/2}$ .

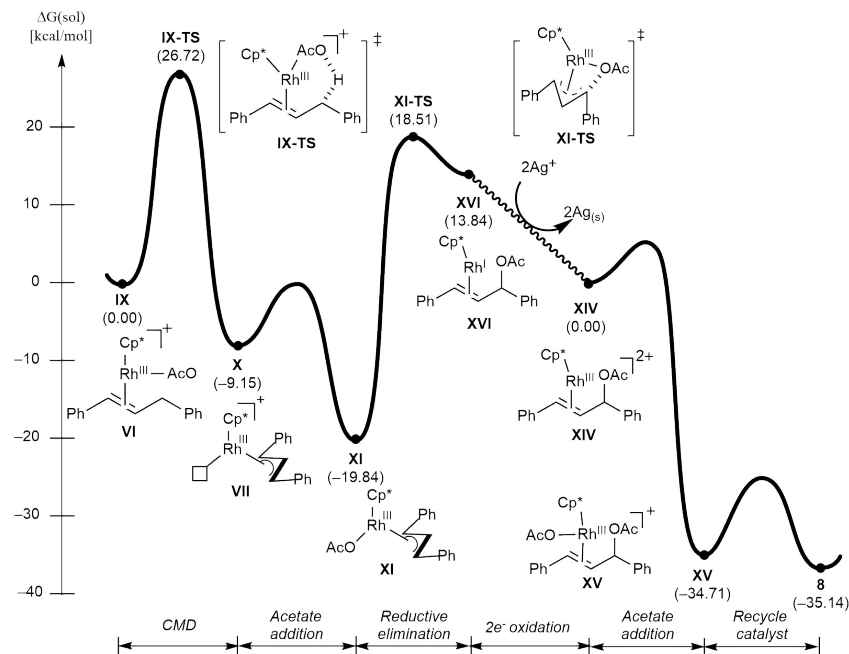
## Quantum chemical studies of the Rh-catalyzed C–H amination reactions

The mechanism of oxidatively-induced rhodium-catalyzed  $\text{C}(\text{sp}^3)\text{--H}$  allylic amination via  $\text{Rh}(\text{IV})$  to  $\text{Rh}(\text{II})$  intermediates is described in the main text. Herein, we outline catalytic routes of allylic C–H acetylation reactions that were thought after. Scheme S2 summarizes the proposed catalytic mechanism that involves the reductive elimination from  $\text{Rh}(\text{III}) \rightarrow \text{Rh}(\text{I})$ . The catalytic cycle is identical to that of the  $\text{Rh}(\text{IV}) \rightarrow \text{Rh}(\text{II})$  until **XI** as described in the main text, then undergoes a reductive elimination step from  $\text{Rh}(\text{III}) \rightarrow \text{Rh}(\text{I})$ . Subsequently, a two electron oxidation step oxidizes the metal center back to  $\text{Rh}(\text{III})$ . Later a ligand exchange step releases the allylic acetate product **8** and regenerate the catalyst.



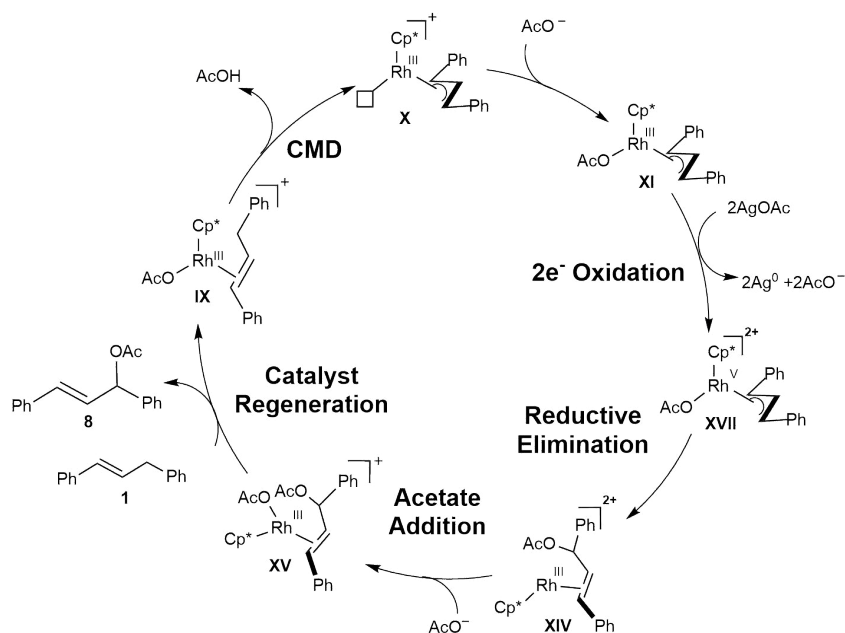
**Scheme S2** Proposed mechanism for rhodium catalyzed allylic acetylation going through Rh(III)→Rh(I)

Figure S7 renders the computed reaction energy profile of the catalytic route shown in Scheme S3. Initially, a concerted metalation and deprotonation (CMD) step activates a C-H bond of the allyl substrate **1** to afford an intermediate **XI** (Figure 8). A reductive elimination (RE) installs a new C-O bond between the pendant acetate and the substrate to yield an intermediate **XVI**, that is energetically uphill by 33.78 kcal/mol from that of **XI** and is associated with transition state **XI-TS** via step barrier of 38.35 kcal/mol. The findings indicate the reductive elimination is the limiting step of the catalytic turnover, which is not viable even at an elevated temperature. After much thoughts, we also concluded that after completion of the reductive elimination, two equivalents of silver cations oxidize the metal center from Rh(I) to Rh(III), that produces an intermediate **XIV**, that is required to proceed forward the catalytic cycle. Lastly, an additional acetate coordinates the metal center to yield an intermediate **XV**, that is energetic downhill to -34.71 kcal/mol. The coordination of the acetate also enables ligand exchange to release the product **8**.



**Figure S7** Energy profile for Rh-catalyzed allylic acetylation going through Rh (III→I)

Scheme S3 summarizes the catalytic cycle that involves the reductive elimination from Rh(V)→Rh(III). The catalytic cycle is identical to that of the Rh(IV)→Rh(II) until **XI** as described in the main text, then a two electron oxidation induced by silver cations results in a highly oxidized metal center Rh(V). Reductive elimination installs a new C-O bond between the pendant acetate and the allylic substrate. Finally ligand exchange steps yield the product **8** and reinstate the catalytic cycle.



**Scheme S3** Proposed mechanism for rhodium catalyzed allylic acetylation going through Rh (V)→Rh(III)

Figure S8 shows the computed reaction energy profile of the catalytic route that involves the reductive elimination that passes through Rh(V)→Rh(III). Initially, CMD mediated by the pendant acetate affords a metalated intermediate **XI**. Then a two electrons ( $2e^-$ ) oxidation follows when two silver cations ( $2Ag^+$ ) deprives of two electrons ( $2e^-$ ) from Rh(III) to increase the oxidation to Rh(V) (**XVII**). A reductive elimination installs a new C-O bond while reducing the metal center from Rh(V) to Rh(III), to produce **XIV**, whose activation energy is 19.45 kcal/mol, suggesting that the reductive elimination is viable at room temperature. Upon completion of the reductive elimination, ligand exchange steps follow to yield the product **8** and regenerate the catalyst **IX**.

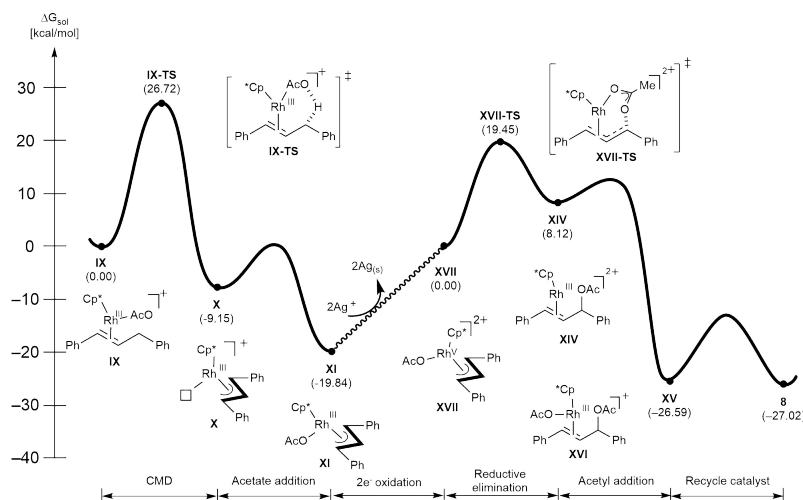


**Figure S8** Energy profile for Rh-catalyzed allylic acetylation going through Rh (V→III)

The mechanistic details of  $Ag^+$  catalyzed amination of allylic acetate is described in the main text. The catalytic cycle begins with the association of silver cation ( $Ag^+$ ) as a Lewis acid with  $\pi$ - orbitals of the allylic double bond. We found there are two possibilities for the association, either with the phenyl group or with the allylic double bond to generate the intermediates. As shown in Figure S9, the insertion of silver cation with the phenyl group **9** activates the liberation of the acetate group to initiate the nucleophilic substitution via the  $S_N1$  mechanism with the activation energy of 14.4 kcal/mol. The insertion with the allylic double bond **9a'** is energetically more difficult by 4.3 kcal/mol than that of **9**, and the activation energy for the nucleophilic substitution is computed as 16.3 kcal/mol (**9a'-TS**), that is 1.9 kcal/mol higher in energy than that of the insertion to the phenyl group. As such, we concluded that the intermediate with silver cation inserted to the phenyl group (**9**) constitutes the major route for the activation of the allylic amination observed from the experiments.



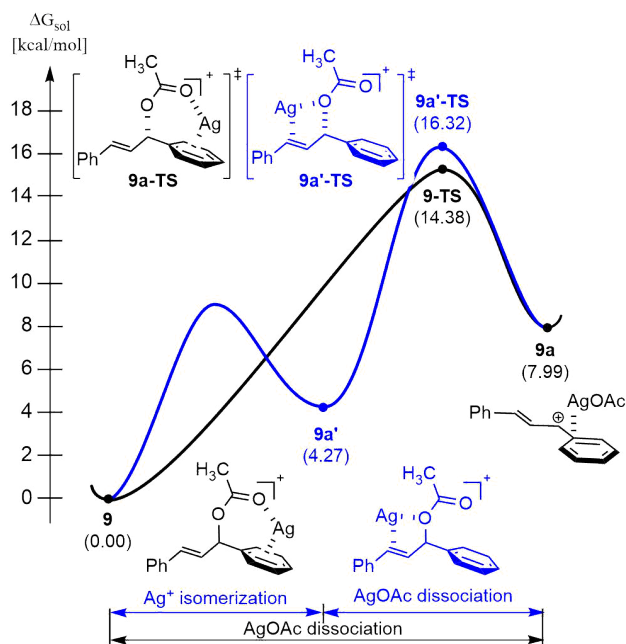
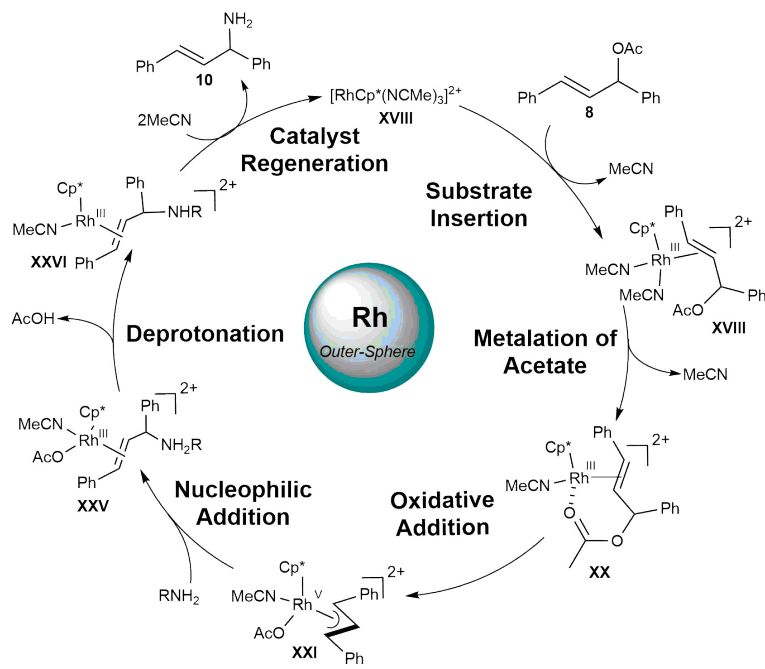


**Figure S9** Energy profile of  $\text{Ag}^+$  catalyzed C–O bond activation of **9**

**Scheme S4** Proposed mechanism of the outer-sphere Rh-catalyzed allylic C–H amination of allylic acetate



The mechanistic details of the Rh-catalyzed allylic C–H amination via the outer-sphere amination route catalyzed by the Cp\*Rh complex is explained. Scheme S4 summarizes the proposed catalytic cycle via the outer-sphere amination mechanism. Figure S14 summarized computed reaction energy profile of the outer-sphere amination of the allylic acetate substrate **8**. Here we considered methylcarbamate as the amine source, in lieu of benzylcarbamate to reduce the computational cost. The first half of the pathway is identical to that of the inner-sphere amination pathway (Scheme 4 and Figure 10) till the formation of C–H activated intermediate **XXI**. To push the reaction forward, the activated intermediate reacts with the amine nucleophile, to yield a Rh-allylamine complex **XXV**. Here the outer-sphere amine attacks the allylic carbon of the intermediate **XXI**, that is associated with an activation barrier of 41.04 kcal/mol by traversing the corresponding transition state **XXI-TS**. The computed activation energy is too high to overcome at 60 °C, negating the hypothesis that the C–N functionalization proceeds via the outer sphere nucleophilic addition mechanism.

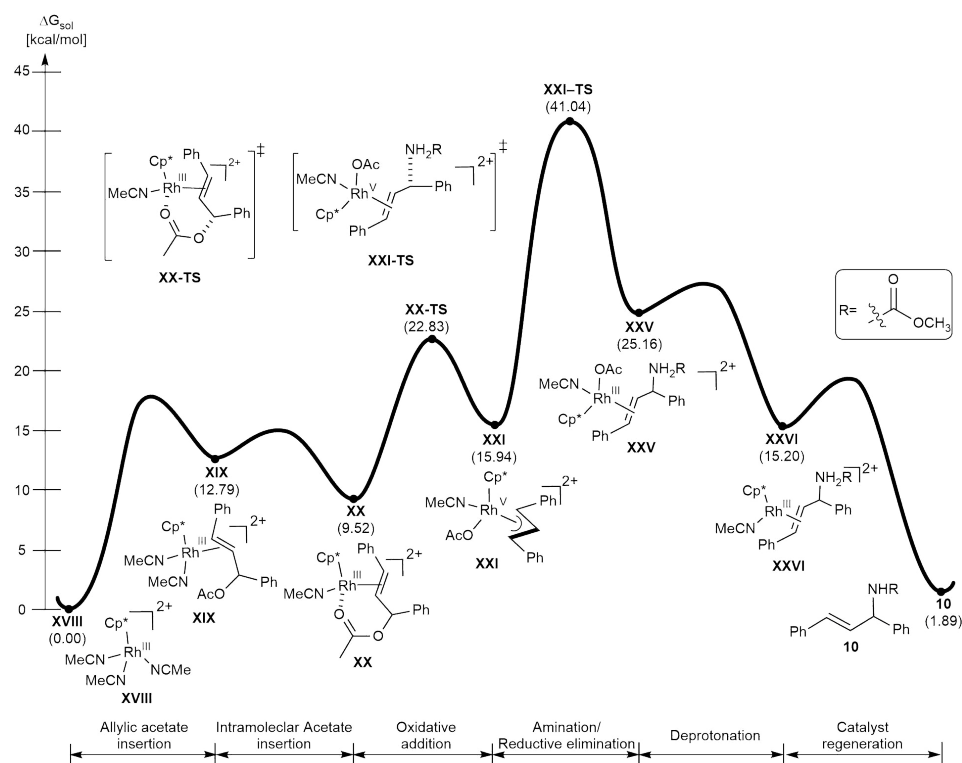


**Figure S10** Complete energy profile of the outer-sphere Rh-catalyzed amination of allylic acetate

**Table S2** Computed Energy Components for Optimized Structures. Units of energies are kcal/mol, except for that of the SCF electronic energy (E(SCF)) which is in eV

Structure	E(SCF)	ZPE	–TS(gas)	G(sol <sub>v</sub> )
<b>IX</b>	–35604.434	327.27	–61.65	–40.61
<b>IX-TS</b>	–35603.277	323.62	–58.73	–39.79

<b>X</b>	−29367.596	286.44	−53.39	−40.14
<b>XI</b>	−35593.844	319.46	−57.80	−9.82
<b>XI-TS</b>	−35592.086	318.44	−59.33	−9.46
<b>XVI</b>	−35592.328	319.36	−59.84	−8.96
<b>XVII</b>	−35578.605	319.64	−62.98	−125.12
<b>XVII-TS</b>	−35577.813	319.55	−59.56	−127.26
<b>XIV</b>	−35578.152	320.09	−59.34	−131.54
<b>XII</b>	−35587.594	319.21	−61.98	−38.36
<b>XII-TS</b>	−35586.871	318.91	−61.34	−37.74
<b>XIII</b>	−35587.343	320.32	−61.05	−38.01
<b>XIV</b>	−35578.158	320.17	−59.07	−131.34
<b>XV</b>	−41807.813	353.42	−66.27	−42.67
<b>1</b>	−15788.563	152.89	−34.77	−4.97
<b>10</b>	−23498.688	190.62	−43.84	−11.62
<b>8</b>	−21991.794	179.28	−42.25	−6.74
<b>9</b>	−25953.041	179.82	−45.35	−55.80
<b>9a'</b>	−25952.594	179.61	−43.94	−62.96
<b>9-TS</b>	−25952.574	178.54	−45.14	−51.12
<b>9a'-TS</b>	−25952.140	178.53	−45.53	−58.71
<b>9-TS'</b>	−33695.821	230.58	−56.83	−61.54
<b>9-TS''</b>	−33695.795	230.21	−55.13	−58.90
<b>9a</b>	−25952.618	178.36	−46.08	−55.37
<b>9a-TS</b>	−33696.574	230.17	−54.55	−51.84
<b>9b</b>	−33696.858	230.95	−55.23	−51.41
<b>9b-TS</b>	−33696.809	228.96	−54.14	−50.23
<b>9c</b>	−33696.676	230.78	−56.35	−60.32
<b>XVIII</b>	−24429.648	228.30	−57.68	−129.21
<b>XIX</b>	−42807.883	380.24	−73.77	−123.33
<b>XX</b>	−39193.441	350.30	−66.12	−123.33
<b>XX-TS</b>	−39192.871	349.45	−66.21	−122.04
<b>XXI</b>	−39193.039	349.48	−69.45	−121.84
<b>XXII</b>	−43322.438	371.21	−73.86	−124.01
<b>XXII-TS</b>	−43322.004	369.19	−69.75	−69.75

<b>XXIII</b>	-37085.129	330.74	-63.67	-123.59
<b>XXIII-TS</b>	-37084.871	330.69	-61.58	-124.38
<b>XXIV</b>	-37085.738	332.29	-61.90	-126.60
<b>XXI-TS</b>	-46936.375	401.29	-76.15	-118.50
<b>XXV</b>	-46936.918	401.81	-75.15	-123.38
<b>XXVI</b>	-40700.313	362.40	-67.10	-123.38
<b>AcOH</b>	-6236.252	38.89	-20.45	-7.75
<b>AcO<sup>-</sup></b>	-6220.611	30.17	-20.58	-68.71
<b>MeCN</b>	-3613.766	28.48	-17.93	-7.32

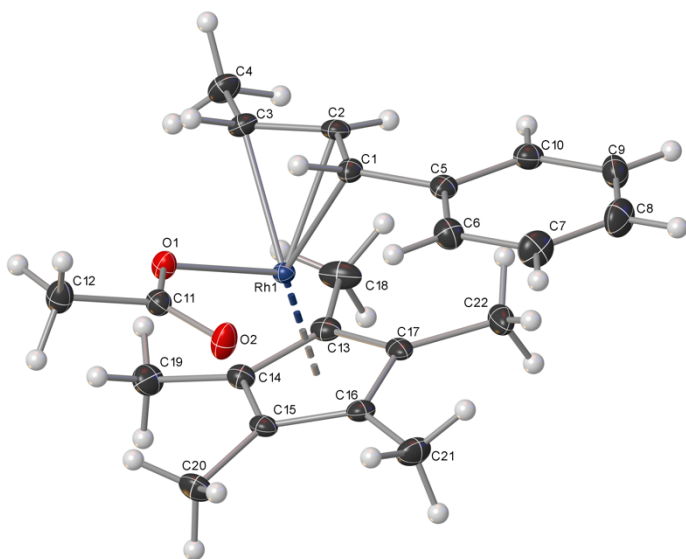


# X-ray Crystal Structure Reports

## RhCp<sup>\*</sup>- $\pi$ -allyl-acetate (VIII)

CCDC 1918703

### Crystal Data and Experimental



**Experimental.** Single orange prism shaped crystals of **Rh-pi-allyl-complex** were obtained by vapor diffusion of pentane into the ether solution. A suitable crystal 0.13×0.08×0.03 mm<sup>3</sup> was selected and mounted on a suitable support on an XtaLAB Synergy, Dualflex, HyPix diffractometer. The crystal was cooled to  $T = 100(2)$  K during data collection. The structure was solved with the **ShelXT** (Sheldrick, 2015) structure solution program using the Intrinsic Phasing solution method and by using **Olex2** (Dolomanov et al., 2009) as the graphical interface. The model was refined with version 2018/3 of **ShelXL-2014** (Sheldrick, 2015) using Least Squares minimisation.

**Crystal Data.** C<sub>22</sub>H<sub>29</sub>O<sub>2</sub>Rh,  $M_r = 428.36$ , monoclinic,  $P2_1/c$  (No. 14),  $a = 7.2611(2)$  Å,  $b = 14.6975(3)$  Å,  $c = 18.0948(5)$  Å,  $\beta = 95.564(2)^\circ$ ,  $\alpha = \gamma = 90^\circ$ ,  $V = 1921.98(8)$  Å<sup>3</sup>,  $T = 100(2)$  K,  $Z = 4$ ,  $Z' = 1$ ,  $\mu(\text{MoK}\alpha) = 0.900$ , 36145 reflections measured, 5883 unique ( $R_{\text{int}} = 0.0581$ ) which were used in all calculations. The final  $wR_2$  was 0.0649 (all data) and  $R_1$  was 0.0280 ( $I > 2\sigma(I)$ ).

Compound	Rh-pi-allyl-complex
Formula	C <sub>22</sub> H <sub>29</sub> O <sub>2</sub> Rh
$D_{\text{calc.}} / \text{g cm}^{-3}$	1.480
$\mu / \text{mm}^{-1}$	0.900
Formula Weight	428.36
Colour	orange
Shape	prism
Size/mm <sup>3</sup>	0.13×0.08×0.03
$T/\text{K}$	100(2)
Crystal System	monoclinic
Space Group	$P2_1/c$
$a/\text{\AA}$	7.2611(2)
$b/\text{\AA}$	14.6975(3)
$c/\text{\AA}$	18.0948(5)
$\alpha/^\circ$	90
$\beta/^\circ$	95.564(2)
$\gamma/^\circ$	90
$V/\text{\AA}^3$	1921.98(8)
$Z$	4
$Z'$	1
Wavelength/Å	0.71073
Radiation type	MoK $\alpha$
$\theta_{\text{min}}/^\circ$	1.788
$\theta_{\text{max}}/^\circ$	30.508
Measured Refl.	36145
Independent Refl.	5883
Reflections with $I > 2\sigma(I)$	4968
$R_{\text{int}}$	0.0581
Parameters	243
Restraints	3
Largest Peak	0.555
Deepest Hole	-0.410
GooF	1.049
$wR_2$ (all data)	0.0649
$wR_2$	0.0624
$R_1$ (all data)	0.0371
$R_1$	0.0280

## Structure Quality Indicators

Reflections:	d min (Mo)	0.70	I/ $\sigma$	24.8	R <sub>int</sub>	5.81%	complete 100% (IUCr)	100%
Refinement:	Shift	0.001	Max Peak	0.6	Min Peak	-0.4	GooF	1.049

A orange prism shaped crystal with dimensions 0.13×0.08×0.03 mm<sup>3</sup> was mounted on a suitable support. Data were collected using an XtaLAB Synergy, Dualflex, HyPix diffractometer equipped with an Oxford Cryosystems low-temperature device, operating at  $T = 100(2)$  K.

Data were measured using  $\omega$  scans of 0.5° per frame for 10.0 s using MoK $\alpha$  radiation (micro-focus sealed X-ray tube, 50 kV, 1.0 mA). The total number of runs and images was based on the strategy calculation from the program **CrysAlisPro** (Rigaku, V1.171.39.43c, 2018). The maximum resolution that was achieved was  $\theta = 30.508^\circ$ .

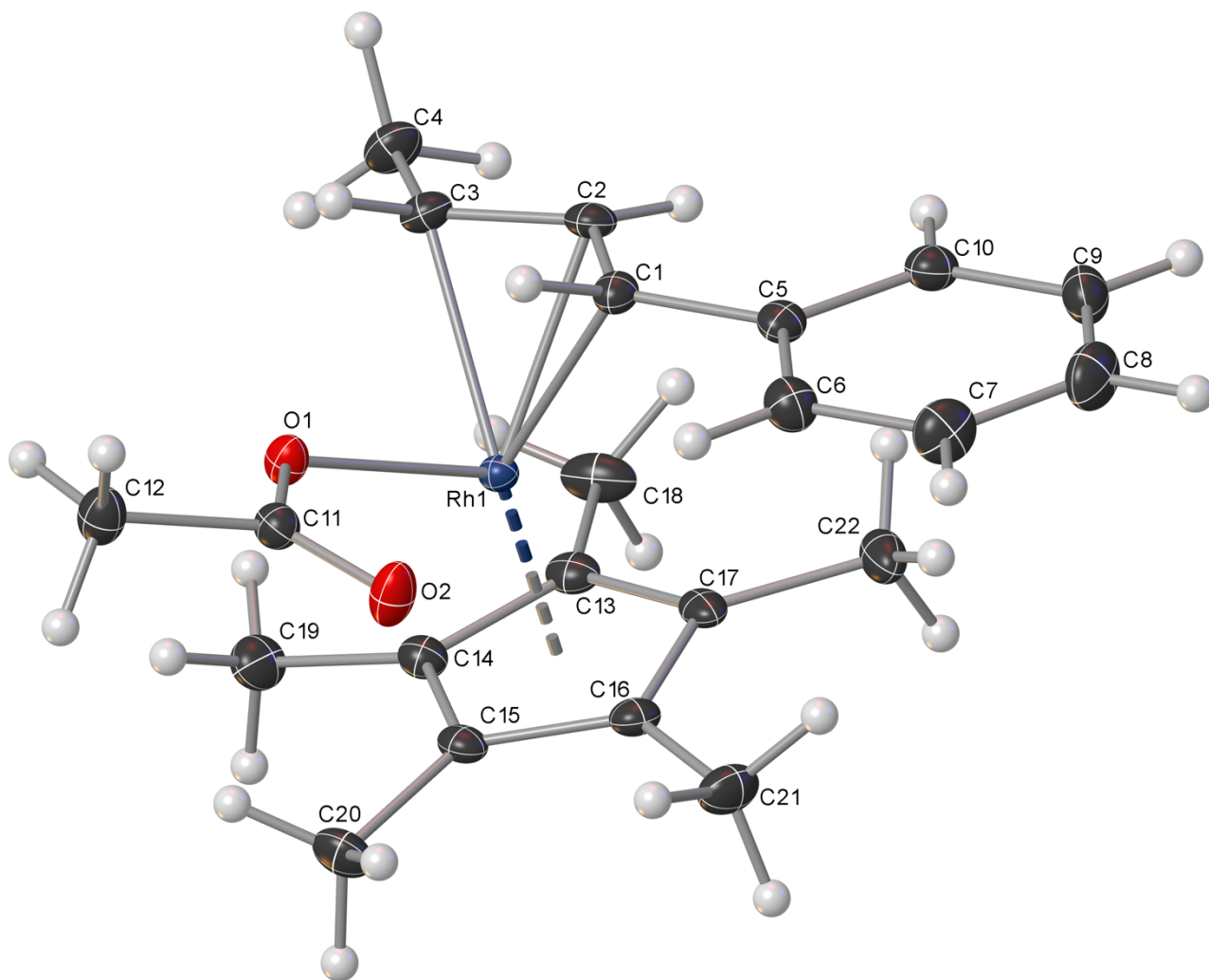
The diffraction patterns were indexed using **CrysAlisPro** (Rigaku, V1.171.39.43c, 2018) and the unit cells were refined using **CrysAlisPro** (Rigaku, V1.171.39.43c, 2018) on 18003 reflections, 50 % of the observed reflections. Data reduction, scaling and absorption corrections were performed using **CrysAlisPro** (Rigaku, V1.171.39.43c, 2018) and CrysAlisPro 1.171.39.43c (Rigaku Oxford Diffraction, 2018). A numerical absorption correction based on Gaussian integration over a multifaceted crystal model was used. An empirical absorption correction using spherical harmonics as implemented in SCALE3 ABSPACK was also used. The final completeness is 100.00% out to 30.508° in  $\theta$ . The absorption coefficient  $\mu$  of this material is 0.900 mm<sup>-1</sup> at this wavelength ( $\lambda = 0.711\text{\AA}$ ) and the minimum and maximum transmissions are 0.855 and 1.000.

The structure was solved and the space group  $P2_1/c$  (# 14) determined by the **ShelXT** (Sheldrick, 2015) structure solution program using Intrinsic Phasing and refined by Least Squares using version 2018/3 of **ShelXL-2014** (Sheldrick, 2015). All non-hydrogen atoms were refined anisotropically. Hydrogen atom positions were calculated geometrically and refined using the riding model.

There is a single molecule in the asymmetric unit, which is represented by the reported sum formula. In other words: Z is 4 and Z' is 1.

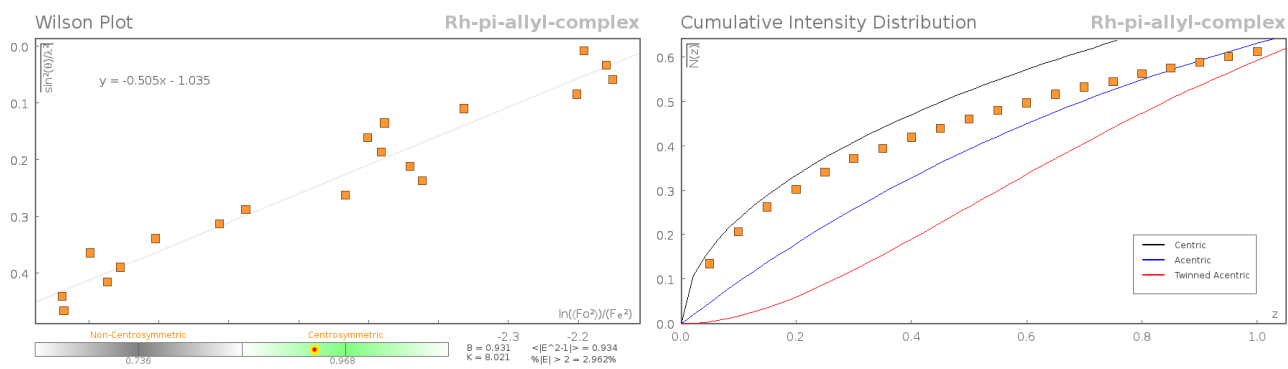
## Images of the Crystal on the Diffractometer



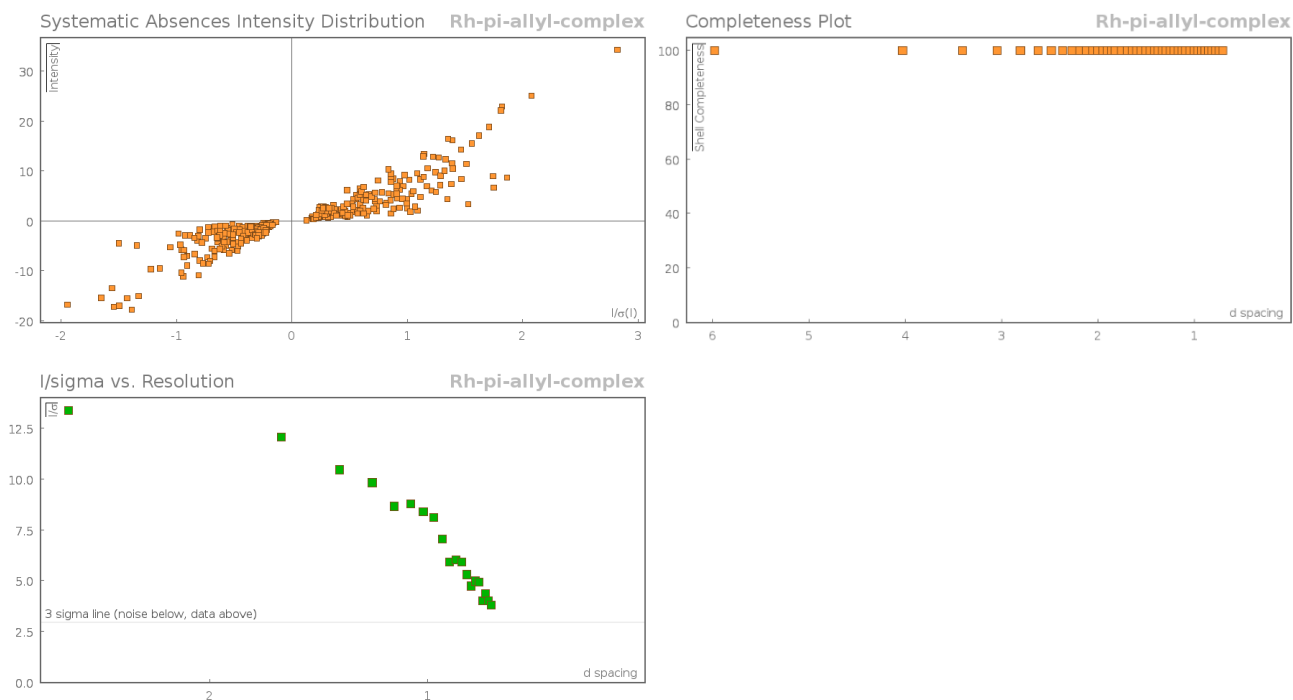


**Figure 1:**

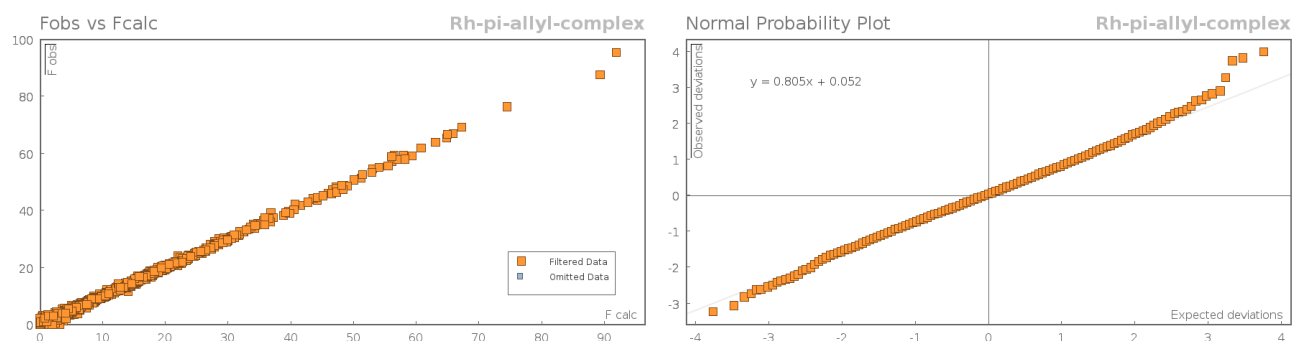
## Data Plots: Diffraction Data







## Data Plots: Refinement and Data



## Reflection Statistics

Total reflections (after filtering)	36810	Unique reflections	5883
Completeness	1.0	Mean $I/\sigma$	17.87
$hkl_{\max}$ collected	(10, 20, 25)	$hkl_{\min}$ collected	(-10, -20, -25)
$hkl_{\max}$ used	(10, 20, 25)	$hkl_{\min}$ used	(-10, 0, 0)
Lim $d_{\max}$ collected	100.0	Lim $d_{\min}$ collected	0.36
$d_{\max}$ used	11.39	$d_{\min}$ used	0.7
Friedel pairs	7871	Friedel pairs merged	1
Inconsistent equivalents	0	$R_{\text{int}}$	0.0581
$R_{\text{sigma}}$	0.0403	Intensity transformed	0
Omitted reflections	0	Omitted by user (OMIT hkl)	0
Multiplicity	(8654, 6755, 2932, 840, 249, 111, 52, 20, 5, 1)	Maximum multiplicity	18
Removed systematic absences	665	Filtered off (Shel/OMIT)	0

**Table 1:** Fractional Atomic Coordinates ( $\times 10^4$ ) and Equivalent Isotropic Displacement Parameters ( $\text{\AA}^2 \times 10^3$ ) for **Rh-pi-allyl-complex**.  $U_{eq}$  is defined as 1/3 of the trace of the orthogonalised  $U_{ij}$ .

Atom	x	y	z	$U_{eq}$
Rh1	3584.1(2)	3831.9(2)	1862.0(2)	10.23(4)
O1	4843.6(17)	4695.9(8)	1128.6(7)	14.7(2)

Atom	x	y	z	$U_{eq}$
O2	5749.0(19)	5820.5(9)	1925.4(7)	21.1(3)
C11	5549(2)	5482.8(11)	1299.9(10)	14.6(3)
C2	5612(2)	2780.6(11)	2043.1(10)	14.8(3)
C3	5030(2)	2784.3(11)	1276.5(10)	15.1(3)
C1	6400(2)	3579.4(12)	2379.4(10)	13.9(3)
C14	619(2)	3960.5(11)	1501.2(10)	13.8(3)
C17	1717(2)	3563.0(12)	2706.1(10)	15.4(3)
C5	6904(2)	3684.8(12)	3180.0(10)	14.8(3)
C13	914(2)	3216.2(11)	2003.6(10)	15.0(3)
C15	1258(2)	4768.3(11)	1905.2(10)	14.0(3)
C16	1893(2)	4528.5(11)	2646.4(10)	14.8(3)
C10	6794(2)	2973.8(12)	3684.7(10)	17.8(4)
C9	7328(3)	3099.9(13)	4434.2(10)	21.6(4)
C22	2076(3)	3013.5(14)	3399.8(11)	22.5(4)
C6	7562(3)	4530.2(12)	3451.7(11)	19.5(4)
C19	-247(3)	3936.8(13)	721.2(11)	21.1(4)
C12	6136(3)	6002.4(12)	636.7(10)	19.5(4)
C21	2609(3)	5166.0(13)	3253.1(11)	21.8(4)
C8	7978(3)	3937.4(14)	4695.0(11)	25.9(4)
C4	4074(3)	1979.8(12)	900.1(11)	20.1(4)
C18	338(3)	2252.1(12)	1862.1(12)	23.2(4)
C7	8083(3)	4651.2(14)	4200.3(11)	24.5(4)
C20	1149(3)	5708.9(12)	1595.5(11)	20.7(4)

**Table 2:** Anisotropic Displacement Parameters ( $\times 10^4$ ) **Rh-pi-allyl-complex**. The anisotropic displacement factor exponent takes the form:  $-2\pi^2[h^2a^{*2} \times U_{11} + \dots + 2hka^* \times b^* \times U_{12}]$

Atom	$U_{11}$	$U_{22}$	$U_{33}$	$U_{23}$	$U_{13}$	$U_{12}$
Rh1	9.60(7)	9.61(6)	11.67(7)	0.25(5)	2.07(4)	0.07(4)
O1	18.5(6)	12.4(6)	13.7(6)	0.3(4)	3.3(5)	-2.8(5)
O2	31.5(8)	18.4(6)	13.7(6)	-1.8(5)	3.6(5)	-5.7(5)
C11	13.4(8)	15.1(8)	15.6(8)	1.8(6)	2.2(6)	-0.2(6)
C2	11.9(8)	13.7(8)	19.2(9)	0.1(6)	3.3(6)	3.9(6)
C3	14.5(8)	14.3(8)	17.2(9)	-2.9(6)	5.4(7)	0.3(6)
C1	10.8(7)	17.0(8)	14.0(8)	0.0(6)	2.0(6)	1.0(6)
C14	10.3(7)	13.7(8)	17.4(8)	0.3(6)	1.1(6)	-0.6(6)
C17	9.9(7)	18.2(8)	19.1(9)	4.8(7)	5.8(6)	3.9(6)
C5	9.9(7)	18.6(9)	15.7(8)	-0.6(6)	0.1(6)	1.9(6)
C13	9.6(7)	14.9(8)	21.2(9)	0.6(6)	4.4(6)	-0.3(6)
C15	9.7(7)	13.7(8)	18.8(9)	1.8(6)	2.6(6)	2.3(6)
C16	11.5(8)	16.0(8)	17.1(8)	-1.8(6)	3.1(6)	2.6(6)
C10	16.0(8)	18.3(8)	19.2(9)	-0.9(7)	1.6(7)	2.7(6)
C9	20.5(9)	27.1(10)	16.9(9)	5.7(7)	1.0(7)	1.9(7)
C22	17.9(9)	29.6(10)	20.9(10)	10.6(8)	6.8(7)	5.3(7)
C6	17.4(9)	20.5(9)	20.4(9)	1.3(7)	0.7(7)	-1.2(7)
C19	17.7(9)	25.4(10)	19.4(9)	-1.3(7)	-2.3(7)	1.4(7)
C12	25.7(10)	16.2(8)	16.8(9)	0.7(7)	3.7(7)	-3.3(7)
C21	20.4(9)	24.7(9)	20.3(9)	-8.0(7)	1.5(7)	2.6(7)
C8	24.3(10)	36.6(11)	15.9(9)	-3.1(8)	-3.0(8)	-1.9(8)
C4	23.0(9)	18.1(9)	19.8(9)	-5.5(7)	4.7(7)	-0.8(7)
C18	15.5(9)	13.3(8)	41.9(12)	-0.1(8)	7.7(8)	-2.8(7)
C7	22.8(10)	26.7(10)	23.3(10)	-5.8(8)	-1.9(8)	-5.2(8)
C20	21.1(9)	12.8(8)	27.9(10)	3.2(7)	1.1(8)	2.5(7)

**Table 3:** Bond Lengths in Å for **Rh-pi-allyl-complex**.

Atom	Atom	Length/Å	Atom	Atom	Length/Å
Rh1	O1	2.1084(12)	Rh1	C2	2.1379(16)

Atom	Atom	Length/Å
Rh1	C3	2.1935(17)
Rh1	C1	2.1963(17)
Rh1	C14	2.1966(17)
Rh1	C17	2.1743(17)
Rh1	C13	2.1772(16)
Rh1	C15	2.1860(16)
Rh1	C16	2.2155(17)
O1	C11	1.290(2)
O2	C11	1.232(2)
C11	C12	1.518(2)
C2	C3	1.410(3)
C2	C1	1.417(2)
C3	C4	1.501(2)
C1	C5	1.468(2)
C14	C13	1.425(2)

Atom	Atom	Length/Å
C14	C15	1.447(2)
C14	C19	1.489(3)
C17	C13	1.440(3)
C17	C16	1.430(2)
C17	C22	1.494(2)
C5	C10	1.395(2)
C5	C6	1.403(2)
C13	C18	1.493(2)
C15	C16	1.420(2)
C15	C20	1.491(2)
C16	C21	1.498(2)
C10	C9	1.386(3)
C9	C8	1.385(3)
C6	C7	1.382(3)
C8	C7	1.386(3)

**Table 4:** Bond Angles in ° for Rh-pi-allyl-complex.

Atom	Atom	Atom	Angle/°
O1	Rh1	C2	101.38(6)
O1	Rh1	C3	82.04(6)
O1	Rh1	C1	85.83(6)
O1	Rh1	C14	103.51(6)
O1	Rh1	C17	152.83(6)
O1	Rh1	C13	140.35(6)
O1	Rh1	C15	91.55(5)
O1	Rh1	C16	115.22(6)
C2	Rh1	C3	37.98(7)
C2	Rh1	C1	38.14(6)
C2	Rh1	C14	138.46(6)
C2	Rh1	C17	103.18(7)
C2	Rh1	C13	106.83(6)
C2	Rh1	C15	166.59(7)
C2	Rh1	C16	130.71(7)
C3	Rh1	C1	67.53(6)
C3	Rh1	C14	114.72(7)
C3	Rh1	C16	162.71(7)
C1	Rh1	C14	170.55(6)
C1	Rh1	C16	110.85(6)
C14	Rh1	C16	64.05(6)
C17	Rh1	C3	124.88(7)
C17	Rh1	C1	106.73(6)
C17	Rh1	C14	64.19(7)
C17	Rh1	C13	38.64(7)
C17	Rh1	C15	63.44(6)
C17	Rh1	C16	38.00(6)
C13	Rh1	C3	103.80(6)
C13	Rh1	C1	133.04(6)
C13	Rh1	C14	38.03(6)
C13	Rh1	C15	63.74(6)
C13	Rh1	C16	63.99(6)
C15	Rh1	C3	150.10(7)
C15	Rh1	C1	141.42(6)
C15	Rh1	C14	38.56(6)
C15	Rh1	C16	37.63(6)
C11	O1	Rh1	125.09(11)

Atom	Atom	Atom	Angle/°
O1	C11	C12	113.36(15)
O2	C11	O1	126.21(16)
O2	C11	C12	120.43(15)
C3	C2	Rh1	73.15(10)
C3	C2	C1	119.28(16)
C1	C2	Rh1	73.16(10)
C2	C3	Rh1	68.87(9)
C2	C3	C4	121.64(16)
C4	C3	Rh1	123.38(12)
C2	C1	Rh1	68.69(9)
C2	C1	C5	124.26(16)
C5	C1	Rh1	122.39(12)
C13	C14	Rh1	70.25(10)
C13	C14	C15	106.65(15)
C13	C14	C19	127.60(15)
C15	C14	Rh1	70.33(9)
C15	C14	C19	125.70(15)
C19	C14	Rh1	126.27(13)
C13	C17	Rh1	70.79(10)
C13	C17	C22	124.97(16)
C16	C17	Rh1	72.56(10)
C16	C17	C13	108.43(15)
C16	C17	C22	126.19(17)
C22	C17	Rh1	128.23(12)
C10	C5	C1	122.85(16)
C10	C5	C6	118.24(17)
C6	C5	C1	118.89(16)
C14	C13	Rh1	71.72(10)
C14	C13	C17	108.33(15)
C14	C13	C18	126.66(17)
C17	C13	Rh1	70.57(9)
C17	C13	C18	124.78(16)
C18	C13	Rh1	127.76(12)
C14	C15	Rh1	71.12(9)
C14	C15	C20	124.63(16)
C16	C15	Rh1	72.31(9)
C16	C15	C14	109.41(14)

Atom	Atom	Atom	Angle/°	Atom	Atom	Atom	Angle/°
C16	C15	C20	125.86(16)	C21	C16	Rh1	125.73(12)
C20	C15	Rh1	125.68(12)	C9	C10	C5	120.79(17)
C17	C16	Rh1	69.44(9)	C8	C9	C10	120.39(18)
C17	C16	C21	126.35(16)	C7	C6	C5	120.59(17)
C15	C16	Rh1	70.06(10)	C9	C8	C7	119.41(18)
C15	C16	C17	107.14(15)	C6	C7	C8	120.57(18)
C15	C16	C21	126.51(16)				

**Table 5:** Hydrogen Fractional Atomic Coordinates ( $\times 10^4$ ) and Equivalent Isotropic Displacement Parameters ( $\text{\AA}^2 \times 10^3$ ) for **Rh-pi-allyl-complex**.  $U_{eq}$  is defined as 1/3 of the trace of the orthogonalised  $U_{ij}$ .

Atom	x	y	z	$U_{eq}$
H10	6356.85	2408.59	3516.36	21
H9	7248.09	2619.23	4763.86	26
H22A	2530.65	2423.78	3279.53	34
H22B	946.69	2946.87	3630.05	34
H22C	2980.21	3316.79	3735.45	34
H6	7648.59	5013.51	3125.11	23
H19A	394.01	4348.9	423.84	32
H19B	-1521.57	4115.24	708.83	32
H19C	-172.26	3331.04	527.98	32
H12A	5882.29	5642.37	195.94	29
H12B	7437.86	6129.61	712.5	29
H12C	5460.9	6563.7	582.33	29
H21A	3449.98	4846.97	3604.44	33
H21B	1592.98	5396.78	3499.25	33
H21C	3243.4	5662.79	3044.42	33
H8	8341.52	4020.17	5197.55	31
H4A	3492.57	1626.93	1258.77	30
H4B	4964.57	1610.54	679.81	30
H4C	3153.42	2187.39	521	30
H18A	289.32	2127.15	1339.82	35
H18B	-862.66	2156.22	2028.73	35
H18C	1216.44	1852.7	2126.75	35
H7	8508.08	5216.41	4373.62	29
H20A	2034.43	6089.8	1876.49	31
H20B	-72.71	5947.2	1624.42	31
H20C	1415.95	5695.43	1086.29	31
H1	7030(30)	3967(11)	2067(10)	16(3)
H3	5670(20)	3161(12)	960(10)	16(3)
H2	5210(30)	2307(11)	2346(10)	16(3)

## Citations

CrysAlisPro Software System, Rigaku Oxford Diffraction, (2018).

O.V. Dolomanov and L.J. Bourhis and R.J. Gildea and J.A.K. Howard and H. Puschmann, Olex2: A complete structure solution, refinement and analysis program, *J. Appl. Cryst.*, (2009), **42**, 339-341.

Sheldrick, G.M., Crystal structure refinement with ShelXL, *Acta Cryst.*, (2015), **C27**, 3-8.

Sheldrick, G.M., ShelXT-Integrated space-group and crystal-structure determination, *Acta Cryst.*, (2015), **A71**, 3-8.

```

#=====
# PLATON/CHECK-( 70414) versus check.def version of 310314 for Entry: rh-pi-al
# Data: Rh-pi-allyl-complex.cif - Type: CIF Bond Precision C-C = 0.0026 A
# Refl: Rh-pi-allyl-complex.fcf - Type: LIST4 Temp = 100 K
# X-Ray Nref/Npar = 24.2
# Cell 7.2611(2) 14.6975(3) 18.0948(5) 90 95.564(2) 90
# Wavelength 0.71073 Volume Reported 1921.98(8) Calculated 1921.98(8)
# SpaceGroup from Symmetry P 21/c Hall: -P 2ybc monoclinic
# Reported P 1 21/c 1 -P 2ybc monoclinic
# MoietyFormula C22 H29 O2 Rh
# Reported C22 H29 O2 Rh
# SumFormula C22 H29 O2 Rh
# Reported C22 H29 O2 Rh
# Mr = 428.36[Calc], 428.36[Rep]
# Dx,gcm-3 = 1.480[Calc], 1.480[Rep]
# Z = 4[Calc], 4[Rep]
# Mu (mm-1) = 0.900[Calc], 0.900[Rep]
# F000 = 888.0[Calc], 888.0[Rep] or F000' = 883.82[Calc]
# Reported T Limits: Tmin=0.855 Tmax=1.000 AbsCorr=GAUSSIAN
# Calculated T Limits: Tmin=0.915 Tmin'=0.887 Tmax=0.972
# Reported Hmax= 10, Kmax= 20, Lmax= 25, Nref= 5883 , Th(max)= 30.508
# Obs in FCF Hmax= 10, Kmax= 20, Lmax= 25, Nref= 5883[ 5883], Th(max)= 30.508
# Calculated Hmax= 10, Kmax= 20, Lmax= 25, Nref= 5883 , Ratio = 1.000
# Reported Rho(min) = -0.41, Rho(max) = 0.56 e/Ang**3 (From CIF)
# Calculated Rho(min) = -0.42, Rho(max) = 0.60 e/Ang**3 (From CIF+FCF data)
# w=1/[sigma**2(Fo**2)+(0.0269P)**2+ 0.4570P], P=(Fo**2+2*Fc**2)/3
# R= 0.0280( 4968), wR2= 0.0649( 5883), S = 1.049 (From CIF+FCF data)
# R= 0.0280( 4968), wR2= 0.0649( 5883), S = 1.049 (From FCF data only)
# R= 0.0280( 4968), wR2= 0.0649( 5883), S = 1.049, Npar= 243
#=====

```

For Documentation: <http://http://www.platonsoft.nl/CIF-VALIDATION.pdf>

```

#=====

```

>>> The Following Improvement and Query ALERTS were generated - (Acta-Mode) <<<

```

#=====

```

Format: alert-number\_ALERT\_alert-type\_alert-level text

```

761_ALERT_1_C CIF Contains no X-H Bonds ..... Please Check
762_ALERT_1_C CIF Contains no X-Y-H or H-Y-H Angles ..... Please Check
906_ALERT_3_C Large K value in the Analysis of Variance ..... 2.018 Check
#=====
002_ALERT_2_G Number of Distance or Angle Restraints on AtSite 6 Note
008_ALERT_5_G No _iucr_refine_reflections_details in the CIF Please Do !
164_ALERT_4_G Nr. of Refined C-H H-Atoms in Heavy-Atom Struct. 3 Note
380_ALERT_4_G Incorrectly? Oriented X(sp2)-Methyl Moiety ..... C4 Check
380_ALERT_4_G Incorrectly? Oriented X(sp2)-Methyl Moiety ..... C12 Check
760_ALERT_1_G CIF Contains no Torsion Angles ..... ? Info
795_ALERT_4_G C-Atom in CIF Coordinate List out of Sequence .. C2 Note
802_ALERT_4_G CIF Input Record(s) with more than 80 Characters ! Info
860_ALERT_3_G Number of Least-Squares Restraints ..... 3 Note
#=====

```

#### ALERT\_Level and ALERT\_Type Summary

```

=====

```

3 ALERT\_Level\_C = Check. Ensure it is Not caused by an Omission or Oversight  
9 ALERT\_Level\_G = General Info/Check that it is not Something Unexpected

3 ALERT\_Type\_1 CIF Construction/Syntax Error, Inconsistent or Missing Data.  
1 ALERT\_Type\_2 Indicator that the Structure Model may be Wrong or Deficient.  
2 ALERT\_Type\_3 Indicator that the Structure Quality may be Low.  
5 ALERT\_Type\_4 Improvement, Methodology, Query or Suggestion.  
1 ALERT\_Type\_5 Informative Message, Check.

```

#=====

```

1 Missing Experimental Info Issue(s) (Out of 54 Tests) - 98 % Satisfied

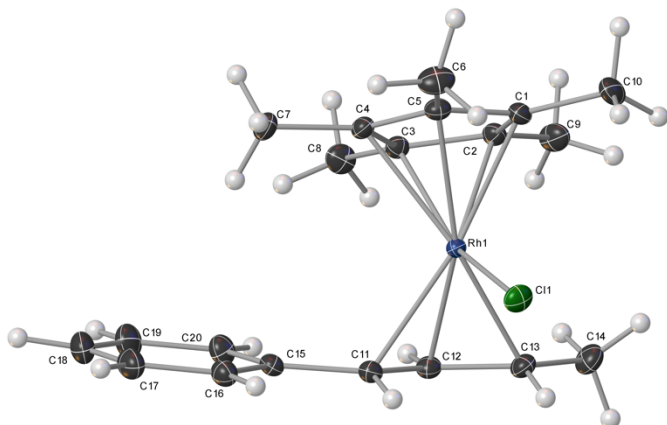
0	Experimental Data Related Issue(s)	(Out of 28 Tests)	-	100 % Satisfied
6	Structural Model Related Issue(s)	(Out of 117 Tests)	-	95 % Satisfied
5	Unresolved or to be Checked Issue(s)	(Out of 223 Tests)	-	98 % Satisfied

#=====

# RhCp<sup>\*</sup>- $\pi$ -allyl-Cl (V)

CCDC 1899790

## Crystal Data and Experimental



**Experimental.** Single orange block-shaped crystals of **Rh-p-allyl-Cl** were recrystallised from a mixture of DCM and pentane by vapor diffusion. A suitable crystal 0.37×0.32×0.28 mm<sup>3</sup> was selected and mounted on a loop with paratone oil on an XtaLAB Synergy-S diffractometer. The crystal was kept at a steady  $T = 100.02(10)$  K during data collection. The structure was solved with the **ShelXT** (Sheldrick, 2015) structure solution program using the Intrinsic Phasing solution method and by using **Olex2** (Dolomanov et al., 2009) as the graphical interface. The model was refined with version 2018/3 of **ShelXL** (Sheldrick, 2015) using Least Squares minimisation.

**Crystal Data.** C<sub>20</sub>H<sub>26</sub>ClRh,  $M_r = 404.77$ , monoclinic,  $P2_1/c$  (No. 14),  $a = 7.4511(10)$  Å,  $b = 12.8249(10)$  Å,  $c = 18.6937(10)$  Å,  $\beta = 94.110(10)^\circ$ ,  $\alpha = \gamma = 90^\circ$ ,  $V = 1781.8(3)$  Å<sup>3</sup>,  $T = 100.02(10)$  K,  $Z = 4$ ,  $Z' = 1$ ,  $\mu(\text{MoK}\alpha) = 1.103$  mm<sup>-1</sup>, 119524 reflections measured, 15581 unique ( $R_{\text{int}} = 0.0215$ ) which were used in all calculations. The final  $wR_2$  was 0.0482 (all data) and  $R_1$  was 0.0201 ( $I > 2\sigma(I)$ ).

Compound	Rh-p-allyl-Cl
Formula	C <sub>20</sub> H <sub>26</sub> ClRh
$D_{\text{calc.}} / \text{g cm}^{-3}$	1.509
$\mu / \text{mm}^{-1}$	1.103
Formula Weight	404.77
Colour	orange
Shape	block
Size/mm <sup>3</sup>	0.37×0.32×0.28
$T/\text{K}$	100.02(10)
Crystal System	monoclinic
Space Group	$P2_1/c$
$a/\text{\AA}$	7.4511(10)
$b/\text{\AA}$	12.8249(10)
$c/\text{\AA}$	18.6937(10)
$\alpha/^\circ$	90
$\beta/^\circ$	94.110(10)
$\gamma/^\circ$	90
$V/\text{\AA}^3$	1781.8(3)
$Z$	4
$Z'$	1
Wavelength/Å	0.71073
Radiation type	MoK $\alpha$
$\Theta_{\text{min}}/^\circ$	1.927
$\Theta_{\text{max}}/^\circ$	46.218
Measured Refl.	119524
Independent Refl.	15581
Reflections with $I > 2\sigma(I)$	14700
$R_{\text{int}}$	0.0215
Parameters	284
Restraints	317
Largest Peak	1.343
Deepest Hole	-1.100
GooF	1.197
$wR_2$ (all data)	0.0482
$wR_2$	0.0477
$R_1$ (all data)	0.0221
$R_1$	0.0201

## Structure Quality Indicators

Reflections:	d min (Mo)	0.49	I/ $\sigma$	88.7	Rint	2.15%	complete 98% (IUCr)	100%
Refinement:	Shift	-0.010	Max Peak	1.3	Min Peak	-1.1	Goof	1.197

An orange block-shaped crystal with dimensions 0.37×0.32×0.28 mm<sup>3</sup> was mounted on a loop with paratone oil. Data were collected using an XtaLAB Synergy, Dualflex, HyPix diffractometer equipped with an Oxford Cryosystems low-temperature device operating at  $T = 100.02(10)$  K.

Data were measured using  $\omega$  scans using MoK $\alpha$  radiation. The total number of runs and images was based on the strategy calculation from the program **CrysAlisPro** (Rigaku, V1.171.40.37a, 2019). The maximum resolution that was achieved was  $\theta = 46.218^\circ$  (0.49 Å).

The diffraction pattern was indexed. The total number of runs and images was based on the strategy calculation from the program **CrysAlisPro** (Rigaku, V1.171.40.37a, 2019) and the unit cell was refined using **CrysAlisPro** on 85788 reflections, 72% of the observed reflections.

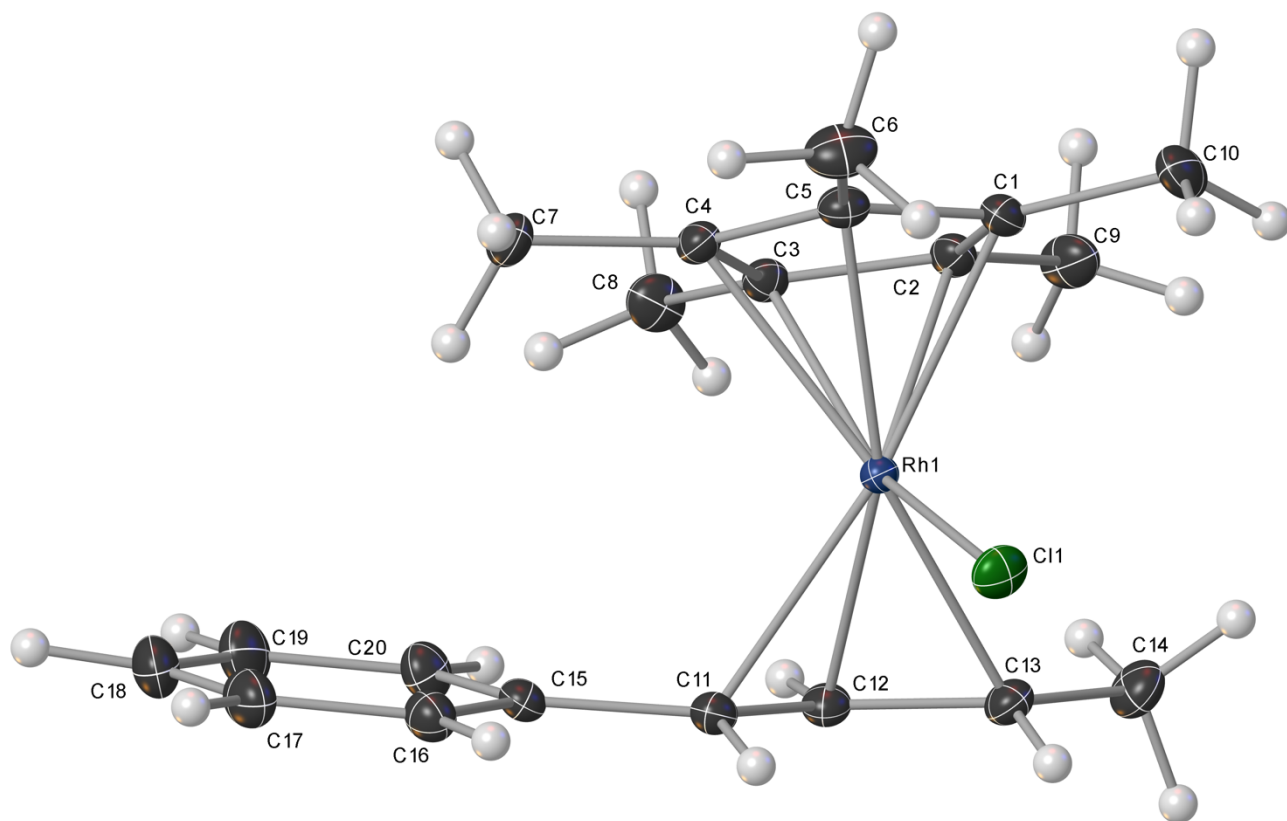
Data reduction, scaling and absorption corrections were performed using **CrysAlisPro** (Rigaku, V1.171.40.37a, 2019). The final completeness is 100.00 % out to 46.218° in  $\theta$ . A numerical absorption correction based on Gaussian integration over a multifaceted crystal model was performed using **CrysAlisPro** (Rigaku, V1.171.40.37a, 2019). An empirical absorption correction using spherical harmonics as implemented in SCALE3 ABSPACK in **CrysAlisPro** (Rigaku, V1.171.40.37a, 2019) was also applied. The absorption coefficient  $\mu$  of this material is 1.103 mm<sup>-1</sup> at this wavelength ( $\lambda = 0.711\text{Å}$ ) and the minimum and maximum transmissions are 0.564 and 1.000.

The structure was solved and the space group  $P2_1/c$  (# 14) determined by the **ShelXT** (Sheldrick, 2015) structure solution program using Intrinsic Phasing and refined by Least Squares using version 2018/3 of **ShelXL** (Sheldrick, 2015). All non-hydrogen atoms were refined anisotropically. All hydrogen atom positions were located from the electron density maps and refined using restraints.

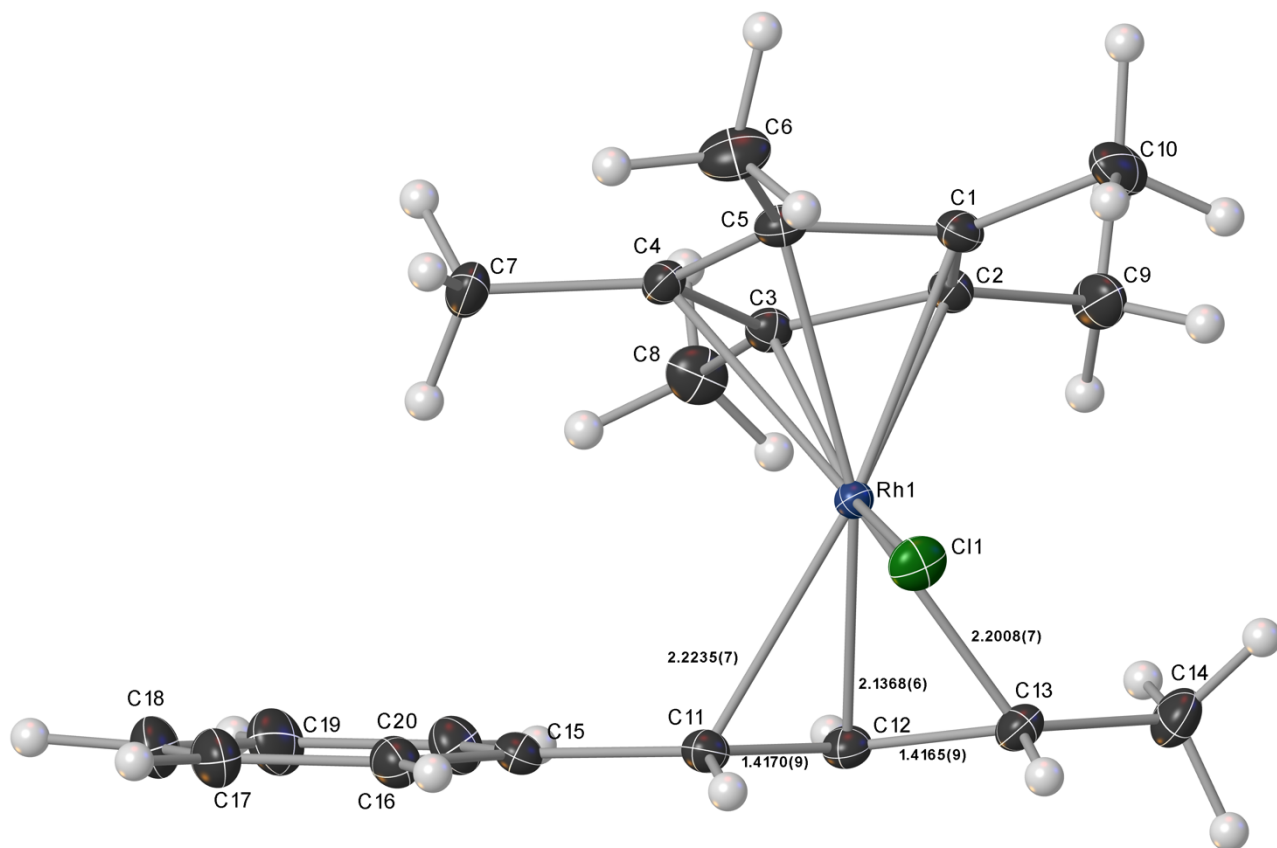
### Images of the Crystal on the Diffractometer





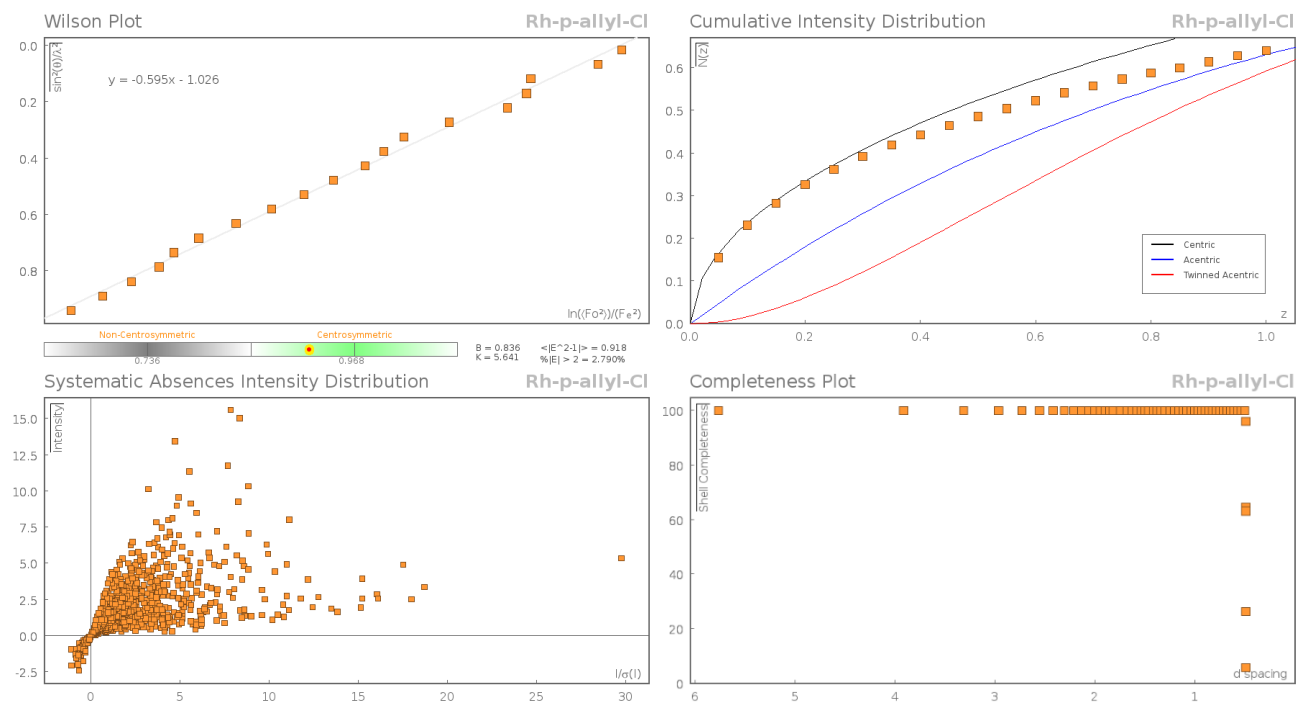


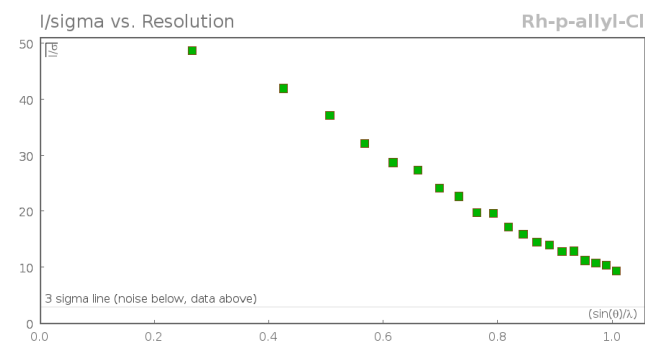
**Figure 1:** Thermal ellipsoid representation of the molecular structure.



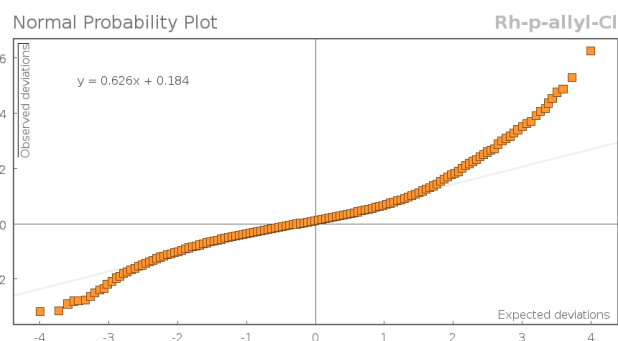
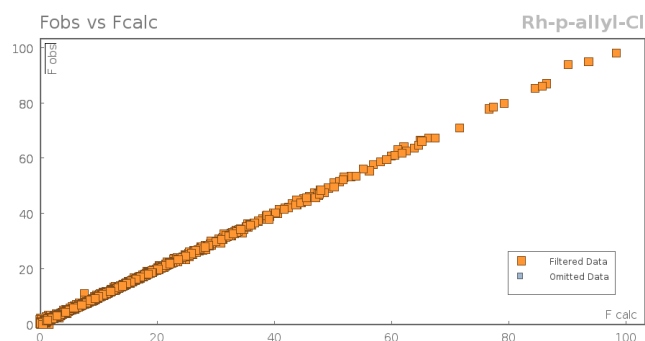
**Figure 2:**

## Data Plots: Diffraction Data





## Data Plots: Refinement and Data



## Reflection Statistics

Total reflections (after filtering)	121235	Unique reflections	15581
Completeness	0.997	Mean $I/\sigma$	57.92
$hkl_{\max}$ collected	(15, 25, 37)	$hkl_{\min}$ collected	(-15, -26, -37)
$hkl_{\max}$ used	(15, 26, 37)	$hkl_{\min}$ used	(-15, 0, 0)
Lim $d_{\max}$ collected	100.0	Lim $d_{\min}$ collected	0.36
$d_{\max}$ used	12.82	$d_{\min}$ used	0.49
Friedel pairs	22515	Friedel pairs merged	1
Inconsistent equivalents	2	$R_{\text{int}}$	0.0215
$R_{\text{sigma}}$	0.0113	Intensity transformed	0
Omitted reflections	0	Omitted by user (OMIT hkl)	0
Multiplicity	(17090, 17005, 9592, 5123, 2113, 964, 511, 103, 13)	Maximum multiplicity	21
Removed systematic absences	1711	Filtered off (Shel/OMIT)	0

**Table 1:** Fractional Atomic Coordinates ( $\times 10^4$ ) and Equivalent Isotropic Displacement Parameters ( $\text{\AA}^2 \times 10^3$ ) for Rh-p-allyl-Cl.  $U_{eq}$  is defined as 1/3 of the trace of the orthogonalised  $U_{ij}$ .

Atom	x	y	z	$U_{eq}$
Rh1	5419.0(2)	8666.3(2)	1743.9(2)	9.52(1)
Cl1	3969.0(2)	10355.2(2)	1616.0(2)	17.35(3)
C1	8193.1(8)	9251.4(5)	1765.4(4)	14.39(8)
C2	8224.6(8)	8236.7(5)	2065.5(3)	13.69(8)
C3	7469.4(8)	7528.6(5)	1520.5(3)	12.77(8)
C4	7092.3(8)	8109.3(5)	864.8(3)	13.00(8)
C5	7492.9(8)	9166.2(5)	1016.8(3)	14.17(8)
C6	7417.0(12)	10056.7(6)	501.7(5)	22.90(13)
C7	6428.2(10)	7654.8(6)	157.7(4)	19.22(11)
C8	7454.8(11)	6367.3(5)	1577.7(5)	19.63(11)
C9	8989.2(10)	7927.6(7)	2796.1(4)	20.67(12)
C10	8891.3(11)	10234.4(6)	2110.2(5)	22.98(13)
C11	2716.2(8)	7938.7(5)	1561.9(3)	13.92(8)

Atom	x	y	z	$U_{eq}$
C12	3573.9(9)	7666.3(5)	2237.1(3)	14.51(8)
C13	4019.0(9)	8476.8(5)	2733.2(3)	15.32(9)
C14	4965.5(11)	8261.7(7)	3452.6(4)	20.60(11)
C15	2321.7(8)	7213.5(5)	963.1(3)	14.32(8)
C16	1421.4(10)	7606.1(6)	337.5(4)	17.75(10)
C17	1058.5(12)	6982.1(7)	-263.1(4)	23.05(13)
C18	1571.4(12)	5938.6(7)	-247.6(5)	25.34(14)
C19	2435.6(13)	5530.9(6)	374.5(5)	24.68(14)
C20	2808.1(11)	6156.6(5)	976.5(4)	19.25(11)

**Table 2:** Anisotropic Displacement Parameters ( $\times 10^4$ ) **Rh-p-allyl-Cl**. The anisotropic displacement factor exponent takes the form:  $-2\pi^2[h^2a^{*2} \times U_{11} + \dots + 2hka^* \times b^* \times U_{12}]$

Atom	$U_{11}$	$U_{22}$	$U_{33}$	$U_{23}$	$U_{13}$	$U_{12}$
Rh1	9.36(1)	9.68(1)	9.62(1)	-0.32(1)	1.29(1)	-0.06(1)
Cl1	19.64(6)	12.10(5)	20.69(6)	0.24(4)	4.23(5)	3.33(4)
C1	11.76(19)	14.7(2)	16.9(2)	-2.33(16)	2.17(16)	-2.43(15)
C2	11.08(18)	16.8(2)	13.01(19)	-0.54(16)	-0.10(15)	0.55(15)
C3	11.81(18)	12.56(18)	13.98(19)	-0.10(14)	1.26(15)	1.28(14)
C4	12.66(19)	15.13(19)	11.37(18)	-0.83(15)	2.07(14)	0.82(15)
C5	13.3(2)	14.37(19)	15.2(2)	1.90(16)	3.70(16)	-0.51(15)
C6	24.4(3)	20.6(3)	24.6(3)	9.2(2)	8.3(2)	0.5(2)
C7	18.9(3)	25.8(3)	13.1(2)	-5.0(2)	1.49(18)	0.8(2)
C8	20.2(3)	12.9(2)	25.7(3)	0.8(2)	1.3(2)	3.00(19)
C9	15.5(2)	30.9(3)	15.1(2)	1.8(2)	-2.49(18)	3.2(2)
C10	18.4(3)	19.7(3)	31.1(4)	-8.9(2)	3.5(2)	-6.5(2)
C11	11.95(19)	14.64(19)	15.3(2)	-0.84(16)	1.89(15)	-0.96(15)
C12	14.6(2)	15.2(2)	14.1(2)	0.68(16)	3.72(16)	-2.28(16)
C13	16.1(2)	17.4(2)	12.90(19)	-0.57(16)	3.97(16)	0.33(17)
C14	24.4(3)	25.2(3)	12.5(2)	-0.1(2)	3.4(2)	1.3(2)
C15	12.14(19)	15.2(2)	15.7(2)	-0.77(16)	1.59(16)	-3.11(15)
C16	16.9(2)	19.9(2)	16.2(2)	0.31(18)	0.07(18)	-2.02(19)
C17	21.5(3)	30.4(3)	16.9(3)	-2.7(2)	-1.1(2)	-4.2(3)
C18	25.3(3)	28.0(3)	22.6(3)	-9.2(3)	1.2(2)	-7.6(3)
C19	28.0(4)	17.7(3)	28.2(3)	-6.4(2)	0.8(3)	-4.2(2)
C20	20.9(3)	14.6(2)	22.0(3)	-1.71(19)	-0.3(2)	-2.40(19)

**Table 3:** Bond Lengths in Å for **Rh-p-allyl-Cl**.

Atom	Atom	Length/Å	Atom	Atom	Length/Å
Rh1	Cl1	2.4247(2)	C3	C8	1.4933(9)
Rh1	C1	2.1967(7)	C4	C5	1.4125(9)
Rh1	C2	2.2034(7)	C4	C7	1.4960(9)
Rh1	C3	2.1746(6)	C5	C6	1.4923(9)
Rh1	C4	2.2494(6)	C11	C12	1.4170(9)
Rh1	C5	2.2244(6)	C11	C15	1.4686(9)
Rh1	C11	2.2235(7)	C12	C13	1.4165(9)
Rh1	C12	2.1368(6)	C13	C14	1.4988(10)
Rh1	C13	2.2008(7)	C15	C16	1.3996(10)
C1	C2	1.4166(9)	C15	C20	1.4028(10)
C1	C5	1.4621(9)	C16	C17	1.3894(11)
C1	C10	1.4924(9)	C17	C18	1.3915(14)
C2	C3	1.4482(8)	C18	C19	1.3904(14)
C2	C9	1.4950(9)	C19	C20	1.3937(11)
C3	C4	1.4446(8)			

**Table 4:** Bond Angles in ° for **Rh-p-allyl-Cl**.

Atom	Atom	Atom	Angle/°	Atom	Atom	Atom	Angle/°
C1	Rh1	Cl1	96.237(19)	C5	C1	C10	124.46(6)
C1	Rh1	C2	37.56(2)	C10	C1	Rh1	126.51(5)
C1	Rh1	C4	63.37(2)	C1	C2	Rh1	70.96(3)
C1	Rh1	C5	38.62(2)	C1	C2	C3	107.63(5)
C1	Rh1	C11	170.72(2)	C1	C2	C9	126.85(6)
C1	Rh1	C13	121.63(3)	C3	C2	Rh1	69.61(3)
C2	Rh1	Cl1	131.115(17)	C3	C2	C9	125.43(6)
C2	Rh1	C4	63.59(2)	C9	C2	Rh1	127.41(5)
C2	Rh1	C5	63.36(2)	C2	C3	Rh1	71.76(3)
C2	Rh1	C11	140.18(2)	C2	C3	C8	125.42(6)
C3	Rh1	Cl1	153.463(17)	C4	C3	Rh1	73.77(3)
C3	Rh1	C1	63.87(2)	C4	C3	C2	108.41(5)
C3	Rh1	C2	38.63(2)	C4	C3	C8	124.95(6)
C3	Rh1	C4	38.07(2)	C8	C3	Rh1	130.29(5)
C3	Rh1	C5	63.10(2)	C3	C4	Rh1	68.16(3)
C3	Rh1	C11	109.27(2)	C3	C4	C7	125.51(6)
C3	Rh1	C13	117.98(2)	C5	C4	Rh1	70.64(3)
C4	Rh1	Cl1	118.558(16)	C5	C4	C3	107.37(5)
C5	Rh1	Cl1	90.366(18)	C5	C4	C7	127.12(6)
C5	Rh1	C4	36.80(2)	C7	C4	Rh1	127.14(5)
C11	Rh1	Cl1	88.140(18)	C1	C5	Rh1	69.67(3)
C11	Rh1	C4	107.35(2)	C1	C5	C6	123.70(6)
C11	Rh1	C5	133.53(2)	C4	C5	Rh1	72.56(3)
C12	Rh1	Cl1	106.43(2)	C4	C5	C1	108.67(5)
C12	Rh1	C1	146.18(3)	C4	C5	C6	127.36(6)
C12	Rh1	C2	111.06(3)	C6	C5	Rh1	128.25(5)
C12	Rh1	C3	99.37(3)	C12	C11	Rh1	67.75(4)
C12	Rh1	C4	122.14(2)	C12	C11	C15	125.14(6)
C12	Rh1	C5	158.94(2)	C15	C11	Rh1	120.80(4)
C12	Rh1	C11	37.86(2)	C11	C12	Rh1	74.39(4)
C12	Rh1	C13	38.08(2)	C13	C12	Rh1	73.40(4)
C13	Rh1	Cl1	86.953(19)	C13	C12	C11	118.15(6)
C13	Rh1	C2	103.93(3)	C12	C13	Rh1	68.51(3)
C13	Rh1	C4	154.13(2)	C12	C13	C14	121.70(6)
C13	Rh1	C5	159.58(2)	C14	C13	Rh1	123.61(5)
C13	Rh1	C11	66.65(3)	C16	C15	C11	117.83(6)
C2	C1	Rh1	71.48(3)	C16	C15	C20	118.05(6)
C2	C1	C5	107.76(5)	C20	C15	C11	124.12(6)
C2	C1	C10	127.56(7)	C17	C16	C15	121.46(7)
C5	C1	Rh1	71.72(4)	C16	C17	C18	119.99(8)
				C19	C18	C17	119.29(7)
				C18	C19	C20	120.81(8)
				C19	C20	C15	120.38(7)

**Table 5:** Torsion Angles in ° for **Rh-p-allyl-Cl**.

Atom	Atom	Atom	Atom	Angle/°
Rh1	C1	C2	C3	60.24(4)
Rh1	C1	C2	C9	-122.99(7)
Rh1	C1	C5	C4	-62.45(4)
Rh1	C1	C5	C6	123.12(7)
Rh1	C2	C3	C4	65.17(4)
Rh1	C2	C3	C8	-126.95(7)
Rh1	C3	C4	C5	60.03(4)

Atom	Atom	Atom	Atom	Angle/°
Rh1	C3	C4	C7	-120.87(6)
Rh1	C4	C5	C1	60.62(4)
Rh1	C4	C5	C6	-125.21(7)
Rh1	C11	C12	C13	60.93(5)
Rh1	C11	C15	C16	-98.52(6)
Rh1	C11	C15	C20	80.74(8)
Rh1	C12	C13	C14	-117.13(6)
C1	C2	C3	Rh1	-61.10(4)
C1	C2	C3	C4	4.07(7)
C1	C2	C3	C8	171.95(6)
C2	C1	C5	Rh1	62.80(4)
C2	C1	C5	C4	0.35(7)
C2	C1	C5	C6	-174.09(6)
C2	C3	C4	Rh1	-63.87(4)
C2	C3	C4	C5	-3.84(7)
C2	C3	C4	C7	175.26(6)
C3	C4	C5	Rh1	-58.46(4)
C3	C4	C5	C1	2.16(7)
C3	C4	C5	C6	176.33(7)
C5	C1	C2	Rh1	-62.95(4)
C5	C1	C2	C3	-2.71(7)
C5	C1	C2	C9	174.06(6)
C7	C4	C5	Rh1	122.45(7)
C7	C4	C5	C1	-176.93(6)
C7	C4	C5	C6	-2.75(11)
C8	C3	C4	Rh1	128.18(7)
C8	C3	C4	C5	-171.79(6)
C8	C3	C4	C7	7.32(10)
C9	C2	C3	Rh1	122.07(6)
C9	C2	C3	C4	-172.76(6)
C9	C2	C3	C8	-4.88(10)
C10	C1	C2	Rh1	122.27(7)
C10	C1	C2	C3	-177.49(6)
C10	C1	C2	C9	-0.72(11)
C10	C1	C5	Rh1	-122.22(7)
C10	C1	C5	C4	175.33(6)
C10	C1	C5	C6	0.90(10)
C11	C12	C13	Rh1	-61.45(5)
C11	C12	C13	C14	-178.57(6)
C11	C15	C16	C17	177.50(7)
C11	C15	C20	C19	-177.76(7)
C12	C11	C15	C16	178.34(6)
C12	C11	C15	C20	-2.40(10)
C15	C11	C12	Rh1	112.86(6)
C15	C11	C12	C13	173.79(6)
C15	C16	C17	C18	0.87(12)
C16	C15	C20	C19	1.50(11)
C16	C17	C18	C19	0.40(13)
C17	C18	C19	C20	-0.69(14)
C18	C19	C20	C15	-0.27(13)
C20	C15	C16	C17	-1.81(11)

**Table 6:** Hydrogen Fractional Atomic Coordinates ( $\times 10^4$ ) and Equivalent Isotropic Displacement Parameters ( $\text{\AA}^2 \times 10^3$ ) for **Rh-p-allyl-Cl**.  $U_{eq}$  is defined as 1/3 of the trace of the orthogonalised  $U_{ij}$ .

Atom	x	y	z	$U_{eq}$
H9A	8395(14)	7338(6)	2988(6)	33.2(10)
H8A	7185(15)	6142(10)	2047(3)	33.2(10)
H10A	8915(15)	10203(10)	2623(2)	33.2(10)
H9B	8863(16)	8509(6)	3111(6)	33.2(10)
H8B	6596(12)	6062(10)	1233(5)	33.2(10)
H10B	8149(14)	10811(7)	1949(6)	33.2(10)
H10C	10090(7)	10361(10)	1976(6)	33.2(10)
H7A	7375(12)	7257(7)	-31(6)	33.2(10)
H9C	10244(6)	7770(8)	2783(7)	33.2(10)
H6A	6858(13)	9876(10)	41(4)	33(4)
H6B	6784(13)	10638(7)	686(6)	33.2(10)
H7B	6074(14)	8193(7)	-179(6)	33.2(10)
H8C	8630(8)	6119(10)	1487(6)	33.2(10)
H7C	5419(10)	7204(7)	208(7)	33.2(10)
H6C	8629(8)	10271(9)	441(6)	33.2(10)
H14A	5613(13)	7616(5)	3450(7)	29(2)
H14B	4098(13)	8217(8)	3806(5)	29(2)
H14C	5797(12)	8810(6)	3588(7)	29(2)
H20	3380(18)	5848(11)	1409(5)	26(2)
H19	2790(20)	4802(6)	391(9)	37(2)
H16	1011(19)	8325(6)	311(8)	26(2)
H17	457(19)	7287(12)	-692(6)	37(2)
H18	1390(20)	5503(11)	-672(6)	37(2)
H11	2012(18)	8553(9)	1529(8)	23(2)
H12	4070(17)	6983(10)	2339(7)	17(3)
H13	3256(17)	9066(9)	2727(8)	23(2)

## Citations

CrysAlisPro Software System, Rigaku Oxford Diffraction, (2019).

O.V. Dolomanov and L.J. Bourhis and R.J. Gildea and J.A.K. Howard and H. Puschmann, Olex2: A complete structure solution, refinement and analysis program, *J. Appl. Cryst.*, (2009), **42**, 339-341.

Sheldrick, G.M., Crystal structure refinement with ShelXL, *Acta Cryst.*, (2015), **C27**, 3-8.

Sheldrick, G.M., ShelXT-Integrated space-group and crystal-structure determination, *Acta Cryst.*, (2015), **A71**, 3-8.

```
#=====
# PLATON/CHECK- ( 70414) versus check.def version of 310314 for Entry: rh-p-all
# Data: Rh-p-allyl-Cl.cif - Type: CIF Bond Precision C-C = 0.0010 A
# Refl: Rh-p-allyl-Cl.fcf - Type: LIST4 Temp = 100 K
# X-Ray Nref/Npar = 54.9
# Cell 7.4511(10) 12.8249(10) 18.6937(10) 90 94.11(1) 90
# Wavelength 0.71073 Volume Reported 1781.8(3) Calculated 1781.8(3)
# SpaceGroup from Symmetry P 21/c Hall: -P 2ybc monoclinic
# Reported P 1 21/c 1 -P 2ybc monoclinic
# MoietyFormula C20 H26 Cl Rh
# Reported C20 H26 Cl Rh
# SumFormula C20 H26 Cl Rh
# Reported C20 H26 Cl Rh
# Mr = 404.77[Calc], 404.77[Rep]
# Dx,gcm-3 = 1.509[Calc], 1.509[Rep]
# Z = 4[Calc], 4[Rep]
# Mu (mm-1) = 1.103[Calc], 1.103[Rep]
# F000 = 832.0[Calc], 832.0[Rep] or F000' = 828.32[Calc]
# Reported T Limits: Tmin=0.564 Tmax=1.000 AbsCorr=GAUSSIAN
# Calculated T Limits: Tmin=0.674 Tmin'=0.661 Tmax=0.736
# Reported Hmax= 15, Kmax= 26, Lmax= 37, Nref= 15581 , Th(max)= 46.218
# Obs in FCF Hmax= 15, Kmax= 26, Lmax= 37, Nref= 15581[ 15581], Th(max)= 46.218
# Calculated Hmax= 15, Kmax= 26, Lmax= 37, Nref= 15624 , Ratio = 0.997
# Reported Rho(min) = -1.10, Rho(max) = 1.34 e/Ang**3 (From CIF)
# Calculated Rho(min) = -1.24, Rho(max) = 1.35 e/Ang**3 (From CIF+FCF data)
# w=1/[sigma**2(Fo**2)+(0.0153P)**2+ 0.5675P], P=(Fo**2+2*Fc**2)/3
# R= 0.0201( 14700), wR2= 0.0482( 15581), S = 1.197 (From CIF+FCF data)
# R= 0.0201( 14700), wR2= 0.0482( 15581), S = 1.197 (From FCF data only)
# R= 0.0201( 14700), wR2= 0.0482( 15581), S = 1.197, Npar= 284
#=====
```

For Documentation: <http://http://www.platonsoft.nl/CIF-VALIDATION.pdf>

```
#=====
```

```
#=====
```

>>> The Following Improvement and Query ALERTS were generated - (Acta-Mode) <<<

```
#=====
```

Format: alert-number\_ALERT\_alert-type\_alert-level text

```
731_ALERT_1_C Bond Calc 2.4247(5), Rep 2.4247(2) ..... 3 su-Rat
RH1 -Cl1 1.555 1.555 # 1
906_ALERT_3_C Large K value in the Analysis of Variance ..... 2.581 Check
#=====
002_ALERT_2_G Number of Distance or Angle Restraints on AtSite 38 Note
153_ALERT_1_G The su's on the Cell Axes are Equal ..... 0.00100 Ang.
164_ALERT_4_G Nr. of Refined C-H H-Atoms in Heavy-Atom Struct. 26 Note
232_ALERT_2_G Hirshfeld Test Diff (M-X) Rh1 -- Cl1 .. 23.5 su
232_ALERT_2_G Hirshfeld Test Diff (M-X) Rh1 -- C1 .. 6.0 su
232_ALERT_2_G Hirshfeld Test Diff (M-X) Rh1 -- C2 .. 6.8 su
232_ALERT_2_G Hirshfeld Test Diff (M-X) Rh1 -- C3 .. 8.9 su
232_ALERT_2_G Hirshfeld Test Diff (M-X) Rh1 -- C4 .. 7.8 su
232_ALERT_2_G Hirshfeld Test Diff (M-X) Rh1 -- C5 .. 8.0 su
232_ALERT_2_G Hirshfeld Test Diff (M-X) Rh1 -- Cl1 .. 12.5 su
232_ALERT_2_G Hirshfeld Test Diff (M-X) Rh1 -- Cl2 .. 7.0 su
232_ALERT_2_G Hirshfeld Test Diff (M-X) Rh1 -- Cl3 .. 11.0 su
860_ALERT_3_G Number of Least-Squares Restraints ..... 317 Note
912_ALERT_4_G Missing # of FCF Reflections Above STh/L= 0.600 44 Note
#=====
```

ALERT\_Level and ALERT\_Type Summary

```
=====
```

2 ALERT\_Level\_C = Check. Ensure it is Not caused by an Omission or Oversight

14 ALERT\_Level\_G = General Info/Check that it is not Something Unexpected

2 ALERT\_Type\_1 CIF Construction/Syntax Error, Inconsistent or Missing Data.

10 ALERT\_Type\_2 Indicator that the Structure Model may be Wrong or Deficient.

2 ALERT\_Type\_3 Indicator that the Structure Quality may be Low.



2 ALERT\_Type\_4 Improvement, Methodology, Query or Suggestion.

#=====

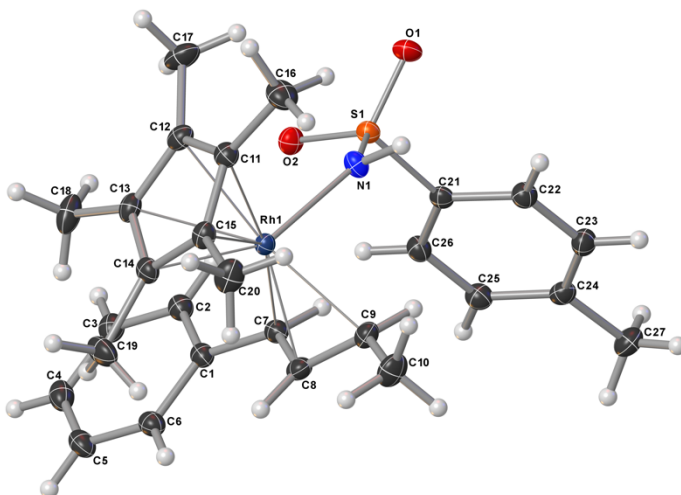
0 Missing Experimental Info Issue(s) (Out of 54 Tests) - 100 % Satisfied  
0 Experimental Data Related Issue(s) (Out of 28 Tests) - 100 % Satisfied  
13 Structural Model Related Issue(s) (Out of 117 Tests) - 89 % Satisfied  
3 Unresolved or to be Checked Issue(s) (Out of 223 Tests) - 99 % Satisfied

#=====

# RhodiumCp<sup>\*</sup>- $\pi$ -allyl-NHTs (VII)

CCDC 1918704

## Crystal Data and Experimental



**Experimental.** Single orange plate-shaped crystals of **RJIH-II-091** were recrystallised from a mixture of DCM and pentane by vapor diffusion. A suitable crystal 0.25×0.15×0.05 mm<sup>3</sup> was selected and mounted on a loop with paratone oil on an XtaLAB Synergy, Dualflex, HyPix diffractometer. The crystal was kept at a steady  $T = 102(4)$  K during data collection. The structure was solved with the **ShelXT** (Sheldrick, 2015) structure solution program using the Intrinsic Phasing solution method and by using **Olex2** (Dolomanov et al., 2009) as the graphical interface. The model was refined with version 2018/3 of **ShelXL-2014** (Sheldrick, 2015) using Least Squares minimisation.

**Crystal Data.** C<sub>27</sub>H<sub>34</sub>NO<sub>2</sub>RhS,  $M_r = 539.52$ , monoclinic,  $P2_1/n$  (No. 14),  $a = 9.08450(13)$  Å,  $b = 26.7256(4)$  Å,  $c = 10.28003(15)$  Å,  $\beta = 94.9110(13)^\circ$ ,  $\alpha = \gamma = 90^\circ$ ,  $V = 2486.71(6)$  Å<sup>3</sup>,  $T = 102(4)$  K,  $Z = 4$ ,  $Z' = 1$ ,  $\mu(\text{MoK}\alpha) = 0.794$  mm<sup>-1</sup>, 44992 reflections measured, 11459 unique ( $R_{\text{int}} = 0.0407$ ) which were used in all calculations. The final  $wR_2$  was 0.0689 (all data) and  $R_1$  was 0.0269 ( $I > 2\sigma(I)$ ).

### Compound

### RJIH-II-091

Formula	C <sub>27</sub> H <sub>34</sub> NO <sub>2</sub> RhS
$D_{\text{calc.}} / \text{g cm}^{-3}$	1.441
$\mu / \text{mm}^{-1}$	0.794
Formula Weight	539.52
Colour	orange
Shape	plate
Size/mm <sup>3</sup>	0.25×0.15×0.05
$T/\text{K}$	102(4)
Crystal System	monoclinic
Space Group	$P2_1/n$
$a/\text{\AA}$	9.08450(13)
$b/\text{\AA}$	26.7256(4)
$c/\text{\AA}$	10.28003(15)
$\alpha/^\circ$	90
$\beta/^\circ$	94.9110(13)
$\gamma/^\circ$	90
$V/\text{\AA}^3$	2486.71(6)
$Z$	4
$Z'$	1
Wavelength/Å	0.71073
Radiation type	MoK $\alpha$
$\theta_{\text{min}}/^\circ$	2.129
$\theta_{\text{max}}/^\circ$	35.630
Measured Refl.	44992
Independent Refl.	11459
Reflections with $I > 2\sigma(I)$	9946
$R_{\text{int}}$	0.0407
Parameters	311
Restraints	4
Largest Peak	0.931
Deepest Hole	-0.348
GooF	1.035
$wR_2$ (all data)	0.0689
$wR_2$	0.0667
$R_1$ (all data)	0.0334
$R_1$	0.0269

## Structure Quality Indicators

Reflections:	d min (Mo)	0.61	I/ $\sigma$	20.8	Rint	4.07%	complete at 2 $\theta$ =72°	100%
Refinement:	Shift	0.002	Max Peak	0.9	Min Peak	-0.3	Goof	1.035

An orange plate-shaped crystal with dimensions 0.25×0.15×0.05 mm<sup>3</sup> was mounted on a loop with paratone oil. Data were collected using an XtaLAB Synergy, Dualflex, HyPix diffractometer equipped with an Oxford Cryosystems low-temperature device operating at  $T = 102(4)$  K.

Data were measured using  $\omega$  scans of 0.5° per frame for s using MoK $\alpha$  radiation. The total number of runs and images was based on the strategy calculation from the program **CrysAlisPro** (Rigaku, V1.171.39.43c, 2018). The maximum resolution that was achieved was  $\Theta = 35.630^\circ$ .

The diffraction pattern was indexed using **CrysAlisPro** (Rigaku, V1.171.39.43c, 2018) and the unit cell was refined using **CrysAlisPro** (Rigaku, V1.171.39.43c, 2018) on 29649 reflections, 66% of the observed reflections.

Data reduction, scaling and absorption corrections were performed using **CrysAlisPro** (Rigaku, V1.171.39.43c, 2018). The final completeness is 100.00 % out to 35.630° in  $\Theta$ . A Gaussian absorption correction was performed using CrysAlisPro 1.171.39.43c (Rigaku Oxford Diffraction, 2018). This is a numerical absorption correction based on Gaussian integration over a multifaceted crystal model. An empirical absorption correction using spherical harmonics as implemented in SCALE3 ABSPACK was also carried out. The absorption coefficient  $\mu$  of this material is 0.794 mm<sup>-1</sup> at this wavelength ( $\lambda = 0.71073\text{\AA}$ ) and the minimum and maximum transmissions are 0.736 and 1.000.

The structure was solved and the space group  $P2_1/n$  (# 14) determined by the **ShelXT** (Sheldrick, 2015) structure solution program using Intrinsic Phasing and refined by Least Squares using version 2018/3 of **ShelXL-2014** (Sheldrick, 2015). All non-hydrogen atoms were refined anisotropically. Hydrogen atom positions were calculated geometrically and refined using the riding model. Most hydrogen atom positions were calculated geometrically and refined using the riding model, but some hydrogen atoms were refined freely.

There is a single molecule in the asymmetric unit, which is represented by the reported sum formula. In other words: Z is 4 and Z' is 1.

## Images of the Crystal on the Diffractometer





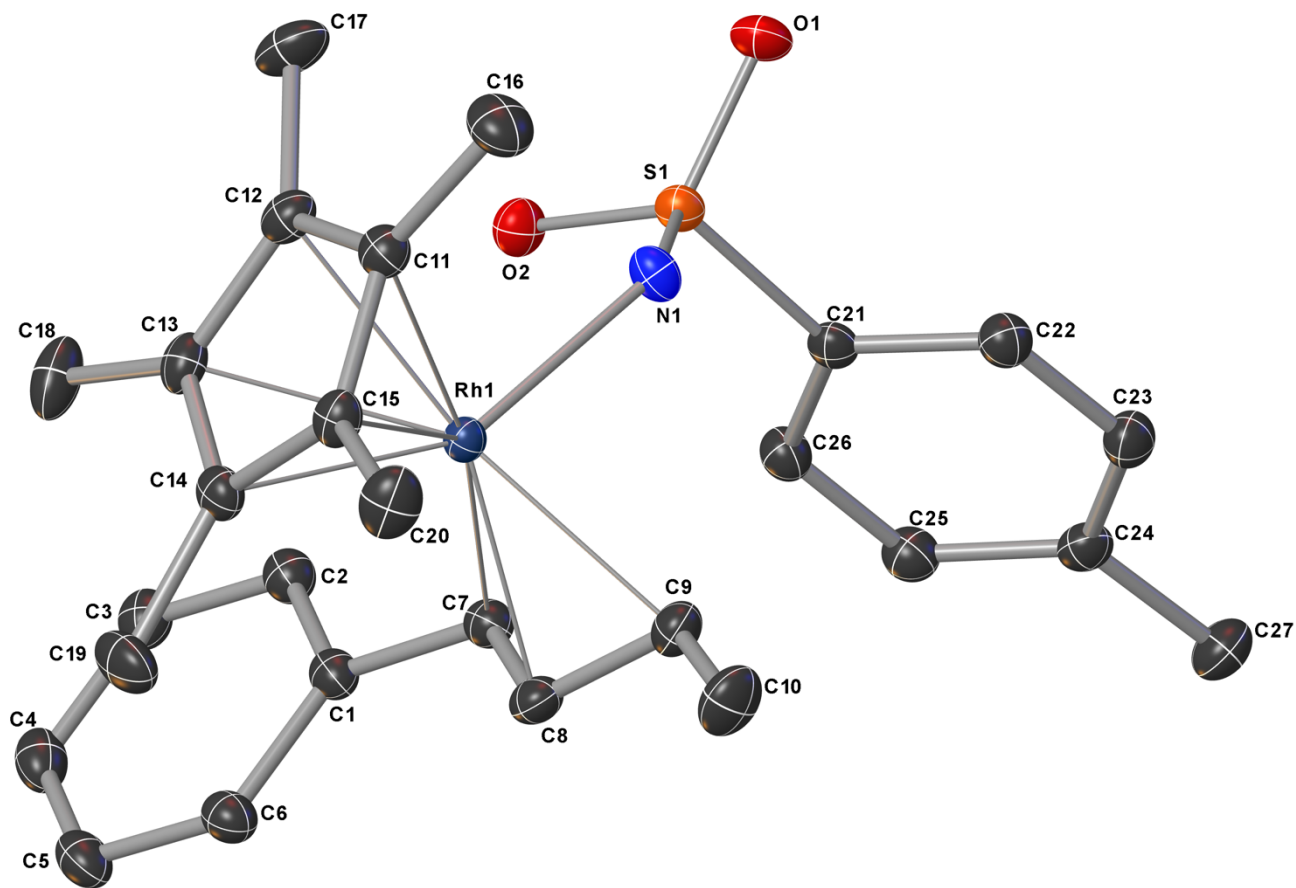
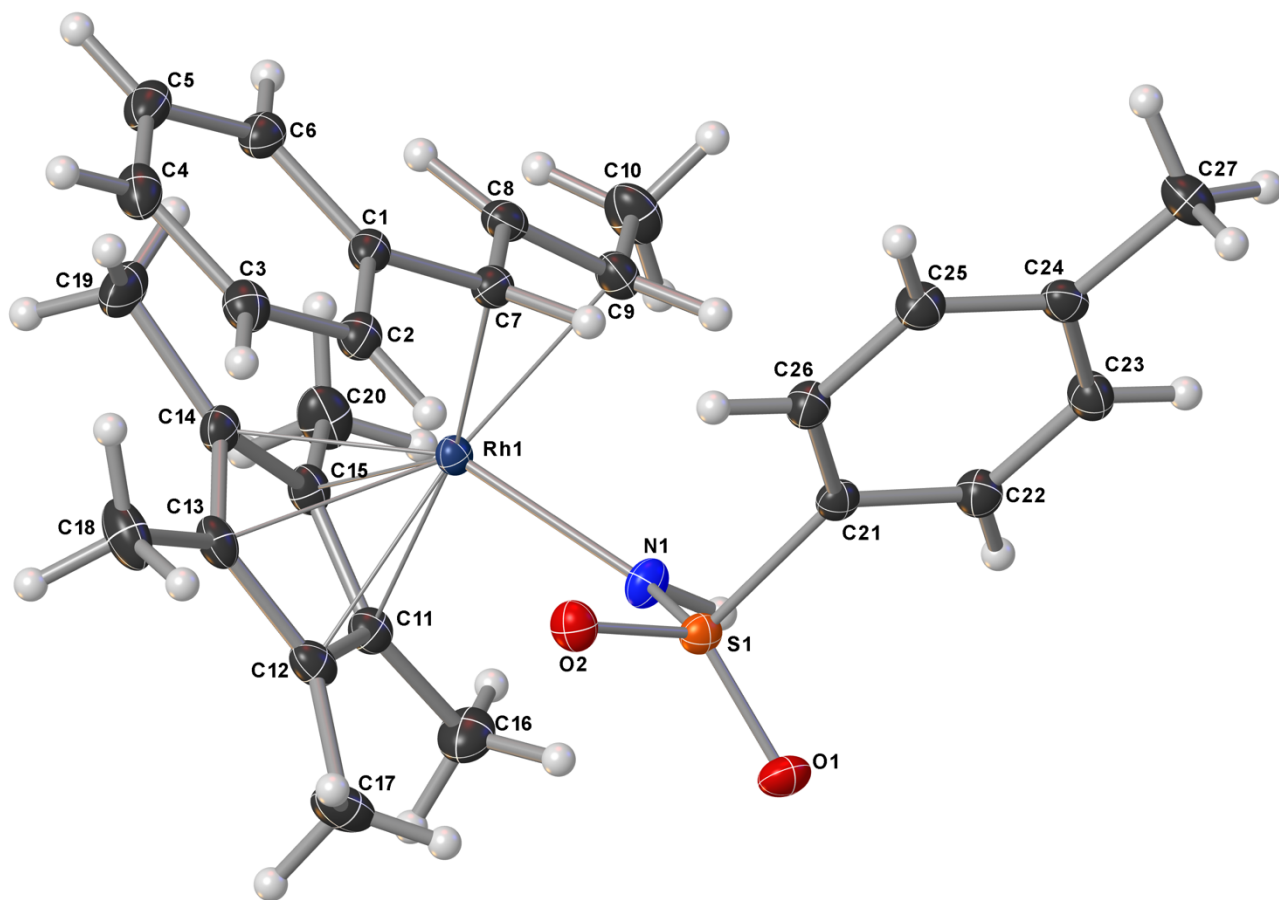
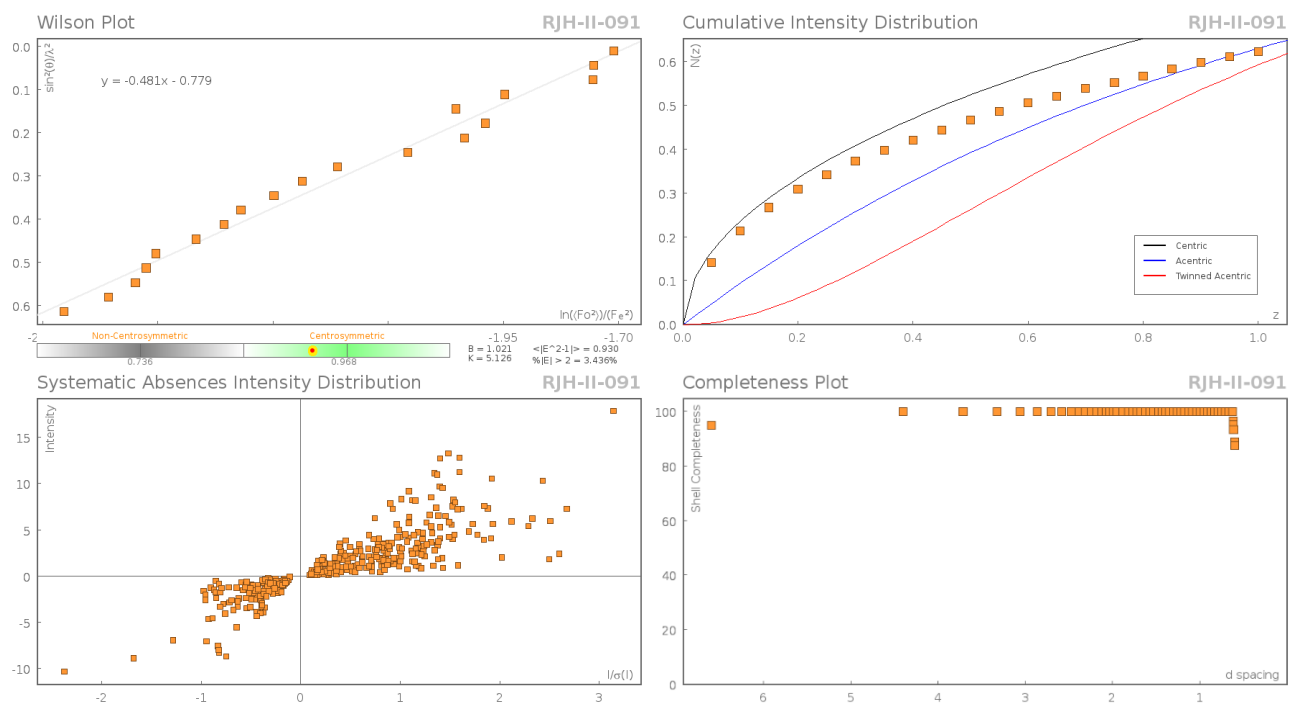


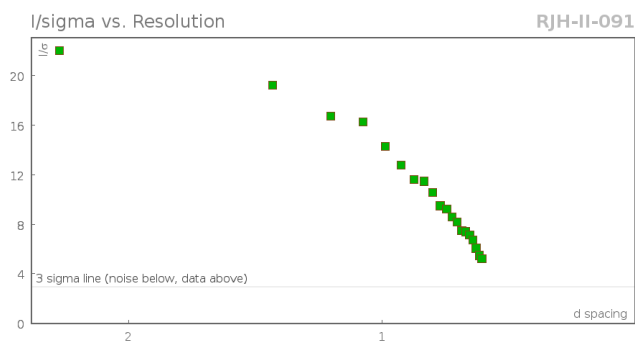
Figure 3:



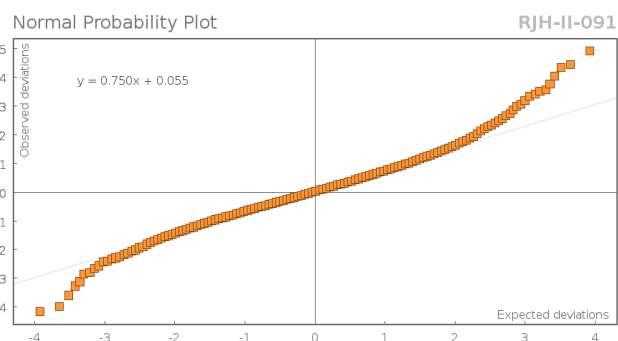
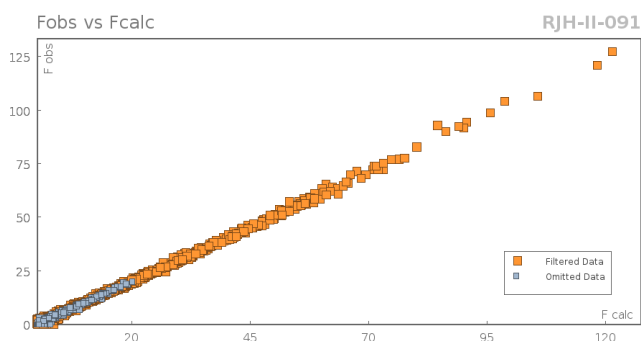
**Figure 4:**

## Data Plots: Diffraction Data





## Data Plots: Refinement and Data



## Reflection Statistics

Total reflections (after filtering)	45369	Unique reflections	11459
Completeness	1.0	Mean $I/\sigma$	21.05
$hkl_{\max}$ collected	(15, 44, 17)	$hkl_{\min}$ collected	(-15, -41, -15)
$hkl_{\max}$ used	(14, 43, 16)	$hkl_{\min}$ used	(-14, 0, 0)
Lim $d_{\max}$ collected	20.0	Lim $d_{\min}$ collected	0.61
$d_{\max}$ used	10.24	$d_{\min}$ used	0.61
Friedel pairs	9750	Friedel pairs merged	1
Inconsistent equivalents	3	$R_{\text{int}}$	0.0397
$R_{\text{sigma}}$	0.0329	Intensity transformed	0
Omitted reflections	0	Omitted by user (OMIT hkl)	0
Multiplicity	(19892, 8556, 2355, 526, 89, 16, 4)	Maximum multiplicity	15
Removed systematic absences	510	Filtered off (Shel/OMIT)	1373

## Images of the Crystal on the Diffractometer



**Table 6:** Fractional Atomic Coordinates ( $\times 10^4$ ) and Equivalent Isotropic Displacement Parameters ( $\text{\AA}^2 \times 10^3$ ) for **RJH-II-091**.  $U_{eq}$  is defined as  $1/3$  of the trace of the orthogonalised  $U_{ij}$ .

Atom	x	y	z	$U_{eq}$
Rh1	5796.2(2)	3739.2(2)	7705.4(2)	12.28(2)
S1	5415.0(3)	4177.3(2)	4636.0(2)	14.40(5)
O2	4974.9(10)	3666.6(3)	4336.7(9)	18.99(15)
O1	4540.4(10)	4571.0(3)	3972.6(8)	19.66(16)

Atom	x	y	z	$U_{eq}$
N1	5551.4(11)	4260.7(4)	6152.6(9)	16.46(16)
C8	8059.7(12)	3524.4(5)	7948.2(11)	18.02(19)
C14	4970.1(13)	3252.8(4)	9181.8(11)	17.33(19)
C2	6590.4(13)	2623.4(4)	5288.2(11)	18.18(19)
C13	4031.8(13)	3175.0(4)	7994.4(11)	17.91(19)
C9	8036.1(13)	4048.5(5)	8122.2(12)	18.87(19)
C25	9304.8(13)	3926.0(5)	3061.0(12)	19.7(2)
C24	9943.6(13)	4401.9(5)	3063.5(11)	18.13(19)
C21	7194.6(12)	4249.1(4)	4055(1)	14.89(17)
C11	3848.6(13)	4007.9(4)	8633.4(11)	17.18(18)
C1	7314.6(12)	2779.5(4)	6481.9(11)	16.67(18)
C3	6400.9(14)	2118.6(5)	5004.7(12)	20.3(2)
C26	7939.7(13)	3849.3(4)	3543.5(11)	17.80(19)
C6	7843.6(13)	2410.4(4)	7371.6(12)	19.6(2)
C7	7495.2(12)	3320.3(4)	6734.0(11)	16.12(18)
C12	3378.2(13)	3640.3(5)	7633.9(11)	18.13(19)
C22	7835.4(13)	4723.1(4)	4104.3(11)	18.74(19)
C23	9188.7(13)	4795.0(5)	3598.2(12)	19.9(2)
C4	6917.3(14)	1756.2(5)	5908.4(13)	22.8(2)
C15	4785.7(13)	3763.0(4)	9595.0(11)	16.87(19)
C19	5762.0(16)	2850.8(5)	9975.9(14)	27.5(3)
C16	3324.2(16)	4539.3(5)	8683.6(14)	26.9(3)
C5	7641.5(15)	1904.0(5)	7091.0(13)	22.7(2)
C20	5417.2(16)	3979.7(6)	10863.7(12)	25.9(2)
C27	11389.2(14)	4490.2(5)	2486.6(14)	24.8(2)
C18	3765.0(16)	2689.9(5)	7291.3(14)	27.7(3)
C17	2290.7(15)	3741.3(6)	6487.9(14)	27.3(3)
C10	8575.6(16)	4286.7(6)	9396.5(13)	27.0(3)

**Table 7:** Anisotropic Displacement Parameters ( $\times 10^4$ ) **RJH-II-091**. The anisotropic displacement factor exponent takes the form:  $-2\pi^2[h^2a^{*2} \times U_{11} + \dots + 2hka^* \times b^* \times U_{12}]$

Atom	$U_{11}$	$U_{22}$	$U_{33}$	$U_{23}$	$U_{13}$	$U_{12}$
Rh1	12.71(4)	13.41(4)	10.83(4)	0.33(2)	1.72(2)	-0.82(2)
S1	15.22(11)	15.91(11)	11.99(10)	0.79(8)	0.72(8)	0.81(9)
O2	20.4(4)	18.7(4)	17.7(4)	-2.1(3)	1.0(3)	-2.8(3)
O1	19.0(4)	22.0(4)	17.4(4)	3.1(3)	-1.8(3)	4.7(3)
N1	22.7(4)	15.3(4)	11.6(4)	0.7(3)	3.0(3)	1.0(3)
C8	12.9(4)	22.2(5)	18.9(5)	1.7(4)	1.2(3)	-0.1(4)
C14	18.6(5)	17.7(4)	16.4(4)	3.3(3)	5.8(4)	0.0(4)
C2	18.7(5)	18.0(5)	18.5(5)	0.6(4)	5.6(4)	1.2(4)
C13	17.0(4)	18.7(5)	19.0(5)	-3.1(4)	6.9(4)	-4.5(4)
C9	15.9(4)	21.3(5)	19.4(5)	0.2(4)	1.7(4)	-3.5(4)
C25	20.2(5)	20.2(5)	19.1(5)	-0.1(4)	4.0(4)	2.5(4)
C24	15.2(4)	22.2(5)	16.7(5)	1.0(4)	-0.1(3)	0.1(4)
C21	16.0(4)	16.7(4)	11.8(4)	1.6(3)	0.2(3)	1.1(3)
C11	16.9(4)	18.7(5)	16.5(4)	0.3(4)	4.8(4)	0.5(4)
C1	15.8(4)	16.5(4)	18.4(5)	1.7(3)	5.8(4)	1.7(4)
C3	20.0(5)	20.0(5)	21.9(5)	-1.5(4)	7.1(4)	-0.4(4)
C26	19.9(5)	16.4(4)	17.5(5)	0.7(3)	3.8(4)	1.0(4)
C6	19.2(5)	19.4(5)	20.7(5)	2.9(4)	4.5(4)	3.3(4)
C7	15.1(4)	17.4(4)	16.2(4)	1.6(3)	3.3(3)	1.1(4)
C12	14.3(4)	24.5(5)	15.8(5)	-0.7(4)	3.1(3)	-1.8(4)
C22	19.5(5)	18.0(5)	18.9(5)	-0.4(4)	2.3(4)	0.4(4)
C23	19.2(5)	18.7(5)	21.9(5)	-0.5(4)	1.8(4)	-2.3(4)
C4	23.5(5)	16.4(5)	30.0(6)	0.0(4)	10.7(5)	1.0(4)
C15	18.5(5)	19.9(5)	12.7(4)	-0.4(3)	4.3(3)	-2.9(4)
C19	29.6(6)	27.3(6)	27.0(6)	12.9(5)	10.3(5)	6.4(5)



Atom	$U_{11}$	$U_{22}$	$U_{33}$	$U_{23}$	$U_{13}$	$U_{12}$
C16	28.1(6)	22.1(6)	31.4(6)	0.7(5)	8.6(5)	7.1(5)
C5	24.0(5)	18.3(5)	26.8(6)	5.0(4)	8.0(4)	4.9(4)
C20	30.0(6)	32.4(6)	15.3(5)	-2.9(4)	2.7(4)	-6.6(5)
C27	17.0(5)	29.4(6)	28.4(6)	-1.3(5)	4.1(4)	-3.1(4)
C18	28.5(6)	23.8(6)	32.8(7)	-10.8(5)	14.0(5)	-10.8(5)
C17	16.7(5)	44.3(8)	20.3(6)	0.9(5)	-2.5(4)	-1.0(5)
C10	24.8(6)	32.8(7)	22.8(6)	-5.1(5)	-1.3(4)	-8.8(5)

**Table 8:** Bond Lengths in Å for **RJH-II-091**.

Atom	Atom	Length/Å	Atom	Atom	Length/Å
Rh1	N1	2.1165(9)	C13	C12	1.4139(17)
Rh1	C8	2.1290(11)	C13	C18	1.4939(17)
Rh1	C14	2.1798(11)	C9	C10	1.5006(17)
Rh1	C13	2.2390(11)	C25	C24	1.3978(17)
Rh1	C9	2.2041(12)	C25	C26	1.3897(17)
Rh1	C11	2.2012(11)	C24	C23	1.3931(17)
Rh1	C7	2.2128(11)	C24	C27	1.5052(17)
Rh1	C12	2.2074(11)	C21	C26	1.3919(16)
Rh1	C15	2.2193(11)	C21	C22	1.3932(16)
S1	O2	1.4480(9)	C11	C12	1.4590(16)
S1	O1	1.4528(9)	C11	C15	1.4094(17)
S1	N1	1.5693(9)	C11	C16	1.5002(17)
S1	C21	1.7812(11)	C1	C6	1.4020(16)
C8	C9	1.4126(17)	C1	C7	1.4750(16)
C8	C7	1.4172(16)	C3	C4	1.3952(18)
C14	C13	1.4428(17)	C6	C5	1.3926(18)
C14	C15	1.4420(16)	C12	C17	1.4958(18)
C14	C19	1.4958(17)	C22	C23	1.3887(17)
C2	C1	1.4052(16)	C4	C5	1.3892(19)
C2	C3	1.3878(17)	C15	C20	1.4957(17)

**Table 9:** Bond Angles in ° for **RJH-II-091**.

Atom	Atom	Atom	Angle/°	Atom	Atom	Atom	Angle/°
N1	Rh1	C8	107.70(4)	C14	Rh1	C15	38.26(4)
N1	Rh1	C14	153.85(4)	C9	Rh1	C13	152.41(5)
N1	Rh1	C13	120.90(4)	C9	Rh1	C7	67.01(4)
N1	Rh1	C9	86.29(4)	C9	Rh1	C12	161.96(5)
N1	Rh1	C11	94.33(4)	C9	Rh1	C15	105.26(4)
N1	Rh1	C7	91.44(4)	C11	Rh1	C13	63.33(4)
N1	Rh1	C12	90.79(4)	C11	Rh1	C9	123.80(4)
N1	Rh1	C15	128.07(4)	C11	Rh1	C7	168.02(4)
C8	Rh1	C14	98.29(4)	C11	Rh1	C12	38.65(4)
C8	Rh1	C13	119.87(4)	C11	Rh1	C15	37.18(4)
C8	Rh1	C9	38.00(5)	C7	Rh1	C13	104.72(4)
C8	Rh1	C11	147.28(4)	C7	Rh1	C15	140.01(4)
C8	Rh1	C7	38.04(4)	C12	Rh1	C13	37.07(4)
C8	Rh1	C12	156.93(5)	C12	Rh1	C7	130.92(4)
C8	Rh1	C15	111.89(4)	C12	Rh1	C15	63.10(4)
C14	Rh1	C13	38.09(4)	C15	Rh1	C13	63.17(4)
C14	Rh1	C9	117.09(4)	O2	S1	O1	116.93(5)
C14	Rh1	C11	63.60(4)	O2	S1	N1	110.00(5)
C14	Rh1	C7	107.91(4)	O2	S1	C21	105.80(5)
C14	Rh1	C12	63.31(4)	O1	S1	N1	110.92(5)

Atom	Atom	Atom	Angle/°
O1	S1	C21	103.90(5)
N1	S1	C21	108.73(5)
S1	N1	Rh1	130.54(6)
C9	C8	Rh1	73.88(7)
C9	C8	C7	119.00(10)
C7	C8	Rh1	74.19(6)
C13	C14	Rh1	73.18(6)
C13	C14	C19	125.43(11)
C15	C14	Rh1	72.36(6)
C15	C14	C13	108.09(10)
C15	C14	C19	125.51(11)
C19	C14	Rh1	129.06(8)
C3	C2	C1	120.83(11)
C14	C13	Rh1	68.73(6)
C14	C13	C18	126.45(12)
C12	C13	Rh1	70.25(6)
C12	C13	C14	107.42(10)
C12	C13	C18	126.11(12)
C18	C13	Rh1	127.49(8)
C8	C9	Rh1	68.11(6)
C8	C9	C10	121.59(11)
C10	C9	Rh1	123.77(9)
C26	C25	C24	121.10(11)
C25	C24	C27	121.19(11)
C23	C24	C25	117.94(11)
C23	C24	C27	120.86(11)
C26	C21	S1	121.92(9)
C26	C21	C22	119.77(10)
C22	C21	S1	118.30(8)
C12	C11	Rh1	70.91(6)
C12	C11	C16	125.94(11)
C15	C11	Rh1	72.11(6)
C15	C11	C12	107.70(10)
C15	C11	C16	126.17(11)
C16	C11	Rh1	126.38(8)
C2	C1	C7	118.76(10)
C6	C1	C2	117.99(11)
C6	C1	C7	123.24(11)
C2	C3	C4	120.42(12)
C25	C26	C21	119.95(11)
C5	C6	C1	121.13(12)
C8	C7	Rh1	67.77(6)
C8	C7	C1	123.93(10)
C1	C7	Rh1	120.24(7)
C13	C12	Rh1	72.68(7)
C13	C12	C11	108.46(10)
C13	C12	C17	126.83(11)
C11	C12	Rh1	70.44(6)
C11	C12	C17	124.55(11)
C17	C12	Rh1	126.36(9)
C23	C22	C21	119.52(11)
C22	C23	C24	121.66(11)
C5	C4	C3	119.50(11)
C14	C15	Rh1	69.39(6)
C14	C15	C20	125.27(11)
C11	C15	Rh1	70.71(6)
C11	C15	C14	108.12(10)
C11	C15	C20	126.53(11)

Atom	Atom	Atom	Angle/°
C20	C15	Rh1	128.15(8)
C4	C5	C6	120.12(11)

**Table 10:** Hydrogen Fractional Atomic Coordinates ( $\times 10^4$ ) and Equivalent Isotropic Displacement Parameters ( $\text{\AA}^2 \times 10^3$ ) for **RJH-II-091**.  $U_{eq}$  is defined as 1/3 of the trace of the orthogonalised  $U_{ij}$ .

Atom	x	y	z	$U_{eq}$
H2	6225.95	2866.38	4667.49	22
H25	9812.35	3650.46	2723.82	24
H3	5916.51	2019.12	4190.09	24
H26	7515.48	3524.2	3524.29	21
H6	8348.64	2507.32	8179.73	24
H22	7350.06	4995.11	4481.35	22
H23	9610.28	5120.48	3617.08	24
H4	6774.79	1410.97	5716.54	27
H19A	6085.09	2589.86	9394.06	41
H19B	5094.92	2705.08	10573.62	41
H19C	6624.87	2994.23	10480.08	41
H16A	3835.16	4708.35	9438.67	40
H16B	2256.94	4543.59	8763.31	40
H16C	3537.77	4713.08	7881.66	40
H5	7999.53	1659.19	7709.41	27
H20A	6360.36	3816.23	11131.62	39
H20B	4726.93	3925.31	11532.15	39
H20C	5578.09	4339.47	10758.38	39
H27A	12076.92	4218.58	2747.66	37
H27B	11809.3	4809.74	2804.19	37
H27C	11222.74	4499.61	1532.36	37
H18A	3600.67	2752.75	6350.86	42
H18B	2891.99	2526.72	7596.79	42
H18C	4627.16	2472.07	7464.91	42
H17A	2423.84	4083.68	6177.47	41
H17B	1284.69	3702	6749.21	41
H17C	2450.99	3504.38	5786.27	41
H10A	7942.9	4572.24	9566.54	40
H10B	9594.17	4402.16	9353.58	40
H10C	8542.01	4041.3	10101.69	40
H8	8250(18)	3299(5)	8720(10)	18(4)
H7	7628(18)	3521(5)	5936(10)	19(3)
H9	8144(18)	4267(5)	7351(10)	19(3)
H1	5580(30)	4614(2)	6370(20)	55(7)

## Citations

CrysAlisPro Software System, Rigaku Oxford Diffraction, (2018).

O.V. Dolomanov and L.J. Bourhis and R.J. Gildea and J.A.K. Howard and H. Puschmann, Olex2: A complete structure solution, refinement and analysis program, *J. Appl. Cryst.*, (2009), **42**, 339-341.

Sheldrick, G.M., Crystal structure refinement with ShelXL, *Acta Cryst.*, (2015), **C27**, 3-8.

Sheldrick, G.M., ShelXT-Integrated space-group and crystal-structure determination, *Acta Cryst.*, (2015), **A71**, 3-8.

```
#=====
# PLATON/CHECK- ( 70414) versus check.def version of 310314   for Entry: rjh-ii-0
# Data: RJH-II-091.cif - Type: CIF                      Bond Precision   C-C = 0.0017 A
# Refl: RJH-II-091.fcf - Type: LIST6                      Temp = 102 K
#                                           X-Ray           Nref/Npar =   36.8
# Cell 9.08450(13)  26.7256(4)10.28003(15)              90   94.9110(13)   90
# Wavelength 0.71073   Volume Reported   2486.71(6)   Calculated   2486.71(6)
# SpaceGroup from Symmetry P 21/n      Hall: -P 2yn      monoclinic
#           Reported P 1 21/n 1      -P 2yn      monoclinic
# MoietyFormula C27 H34 N O2 Rh S
#           Reported C27 H34 N O2 Rh S
#           SumFormula C27 H34 N O2 Rh S
#           Reported C27 H34 N O2 Rh S
# Mr           =      539.53[Calc],      539.52[Rep]
# Dx,gcm-3     =      1.441[Calc],      1.441[Rep]
# Z            =           4[Calc],      4[Rep]
# Mu (mm-1)    =      0.794[Calc],      0.794[Rep]
# F000         =     1120.0[Calc],     1120.0[Rep]   or F000' =     1116.37[Calc]
# Reported T Limits: Tmin=0.736           Tmax=1.000   AbsCorr=GAUSSIAN
# Calculated T Limits: Tmin=0.867 Tmin'=0.820   Tmax=0.961
# Reported Hmax= 14, Kmax= 43, Lmax= 16, Nref= 11459           , Th(max)= 35.630
# Obs in FCF Hmax= 14, Kmax= 43, Lmax= 16, Nref= 11459[ 11459], Th(max)= 35.630
# Calculated Hmax= 14, Kmax= 43, Lmax= 16, Nref= 11463           , Ratio = 1.000
# Reported Rho(min) = -0.35, Rho(max) = 0.93 e/Ang**3 (From CIF)
# w=1/[sigma**2(Fo**2)+(0.0316P)**2+ 0.7328P], P=(Fo**2+2*Fc**2)/3
# R= 0.0267( 9921), wR2= 0.0636( 11459), S = 1.791           (From FCF data only)
# R= 0.0269( 9946), wR2= 0.0689( 11459), S = 1.035, Npar= 311
#=====
For Documentation: http://http://www.platonsoft.nl/CIF-VALIDATION.pdf
#=====
```

```
#=====
>>> The Following Improvement and Query ALERTS were generated - (Acta-Mode) <<<
#=====
Format: alert-number_ALERT_alert-type_alert-level text
```

```
#=====
094_ALERT_2_C Ratio of Maximum / Minimum Residual Density ....      2.68 Why ?
#=====
002_ALERT_2_G Number of Distance or Angle Restraints on AtSite      8 Note
008_ALERT_5_G No _iucr_refine_reflections_details in the CIF      Please Do !
164_ALERT_4_G Nr. of Refined C-H H-Atoms in Heavy-Atom Struct.      3 Note
760_ALERT_1_G CIF Contains no Torsion Angles .....      ? Info
795_ALERT_4_G C-Atom in CIF Coordinate List out of Sequence ..      C2 Note
796_ALERT_4_G O-Atom in CIF Coordinate List out of Sequence ..      O1 Note
802_ALERT_4_G CIF Input Record(s) with more than 80 Characters      ! Info
860_ALERT_3_G Number of Least-Squares Restraints .....      4 Note
910_ALERT_3_G Missing # of FCF Reflections Below Th(Min) .....      1 Why ?
912_ALERT_4_G Missing # of FCF Reflections Above STh/L= 0.600      4 Note
961_ALERT_5_G Dataset Contains no Negative Intensities .....      Please Check
#=====
```

#### ALERT\_Level and ALERT\_Type Summary

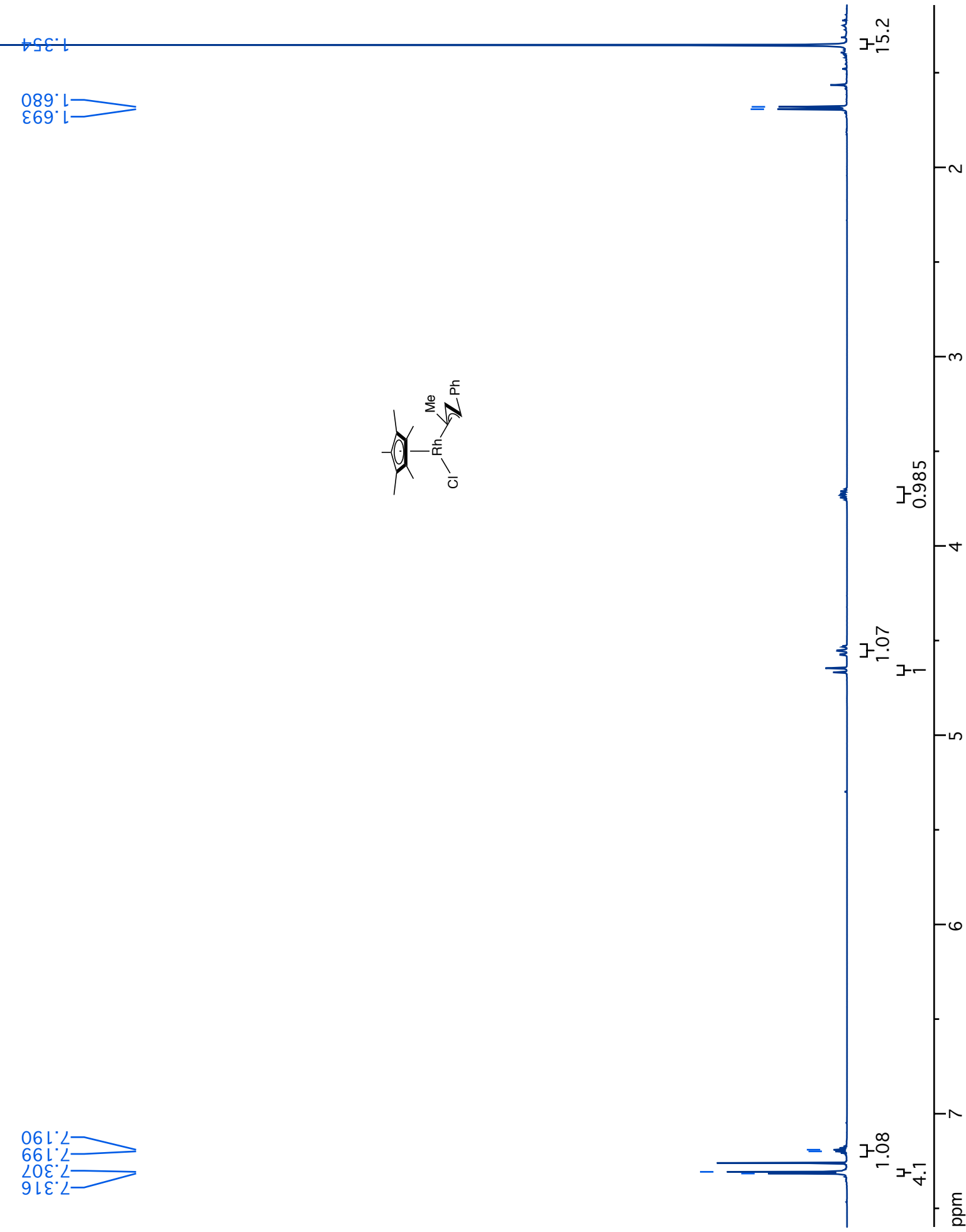
```
=====
```

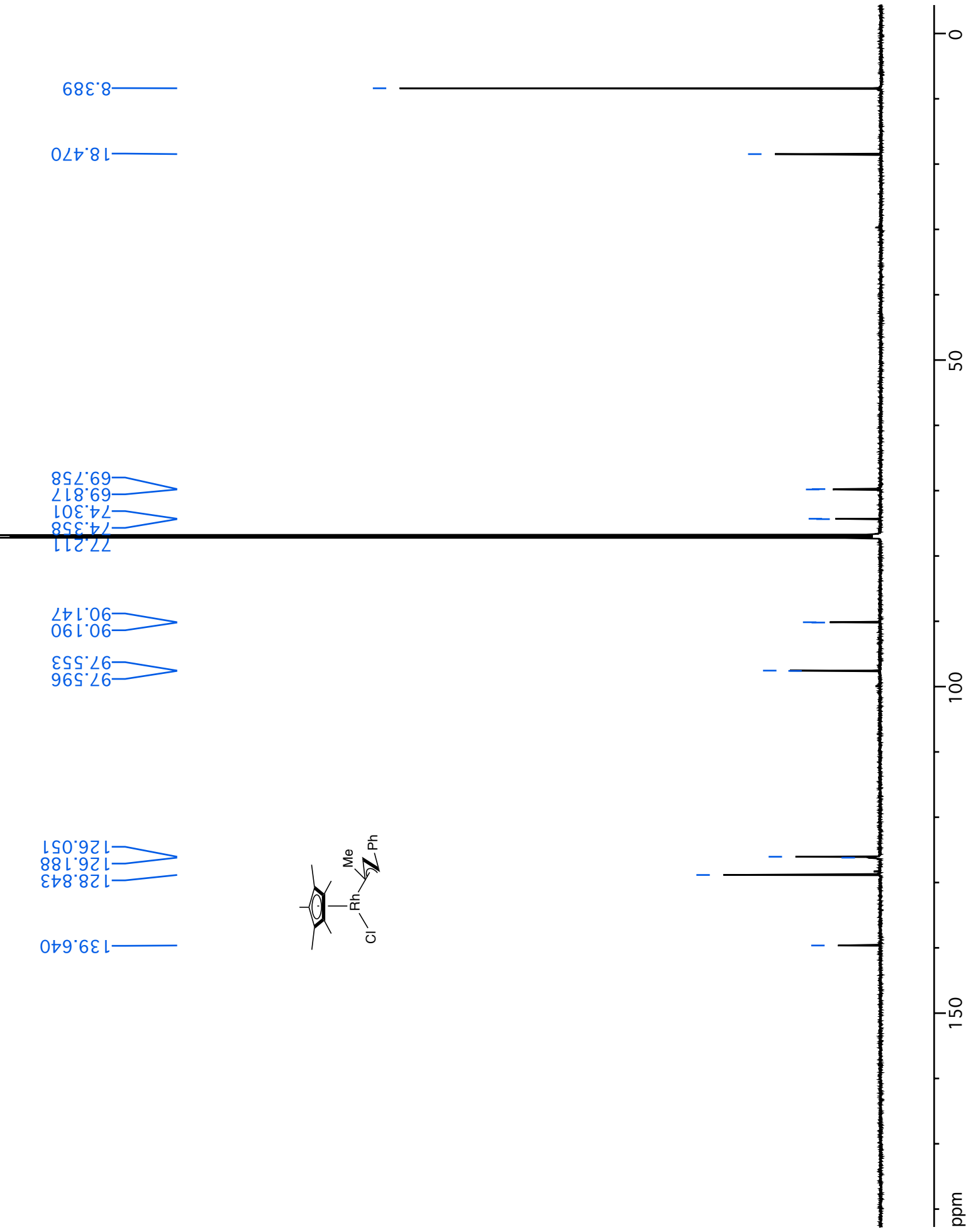
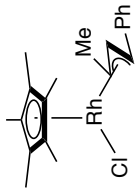
```
2 ALERT_Level_A = Most Likely a Serious Problem - Resolve or Explain
2 ALERT_Level_B = A Potentially Serious Problem - Consider Carefully
1 ALERT_Level_C = Check. Ensure it is Not caused by an Omission or Oversight
11 ALERT_Level_G = General Info/Check that it is not Something Unexpected
```

```
4 ALERT_Type_1 CIF Construction/Syntax Error, Inconsistent or Missing Data.
```

2 ALERT\_Type\_2 Indicator that the Structure Model may be Wrong or Deficient.  
3 ALERT\_Type\_3 Indicator that the Structure Quality may be Low.  
5 ALERT\_Type\_4 Improvement, Methodology, Query or Suggestion.  
2 ALERT\_Type\_5 Informative Message, Check.  
#=====

1 Missing Experimental Info Issue(s) (Out of 54 Tests) - 98 % Satisfied  
0 Experimental Data Related Issue(s) (Out of 28 Tests) - 100 % Satisfied  
5 Structural Model Related Issue(s) (Out of 117 Tests) - 96 % Satisfied  
10 Unresolved or to be Checked Issue(s) (Out of 223 Tests) - 96 % Satisfied  
#=====







1.770  
1.758

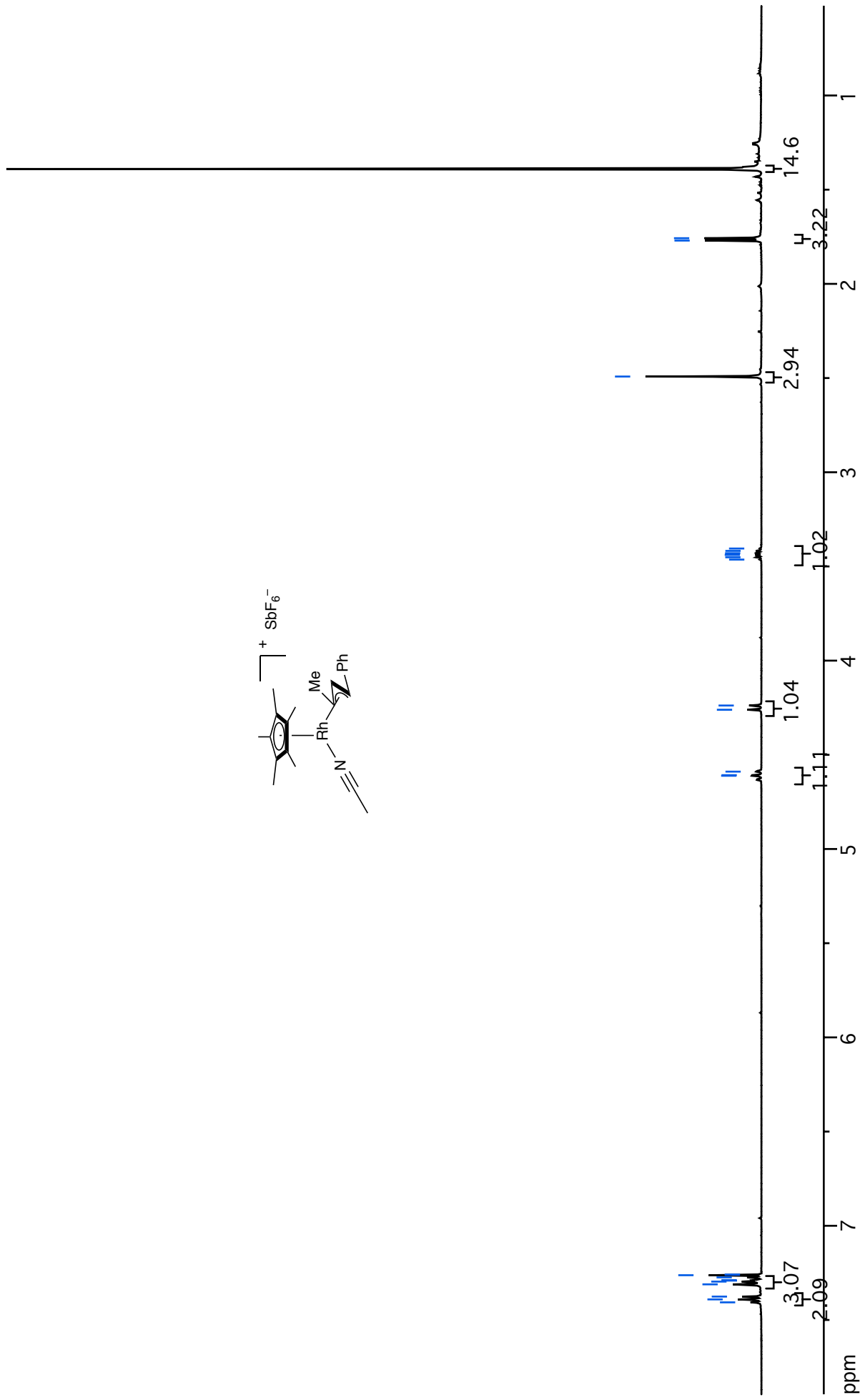
2.492

3.464  
3.451  
3.439  
3.430  
3.417  
3.405

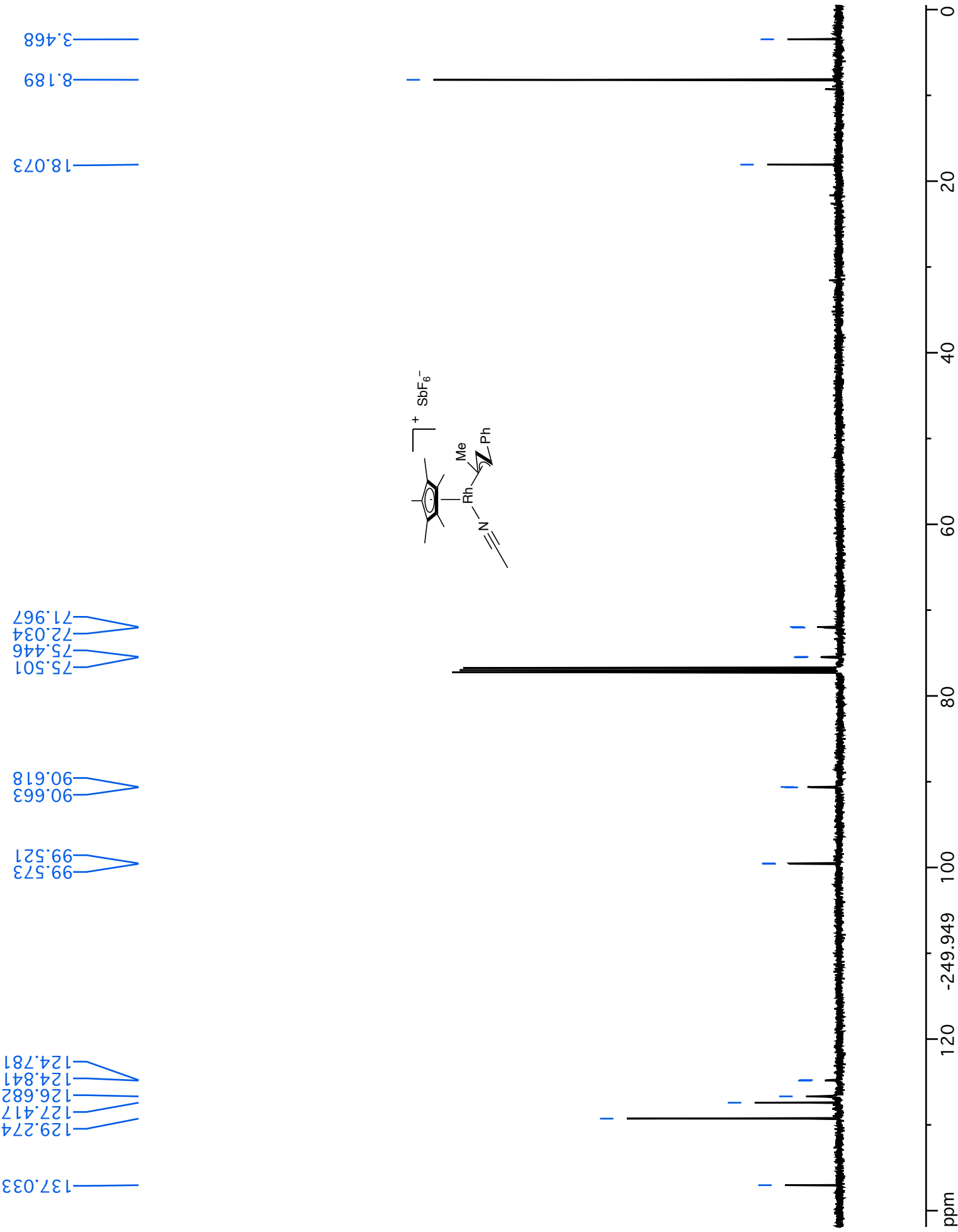
4.261  
4.238

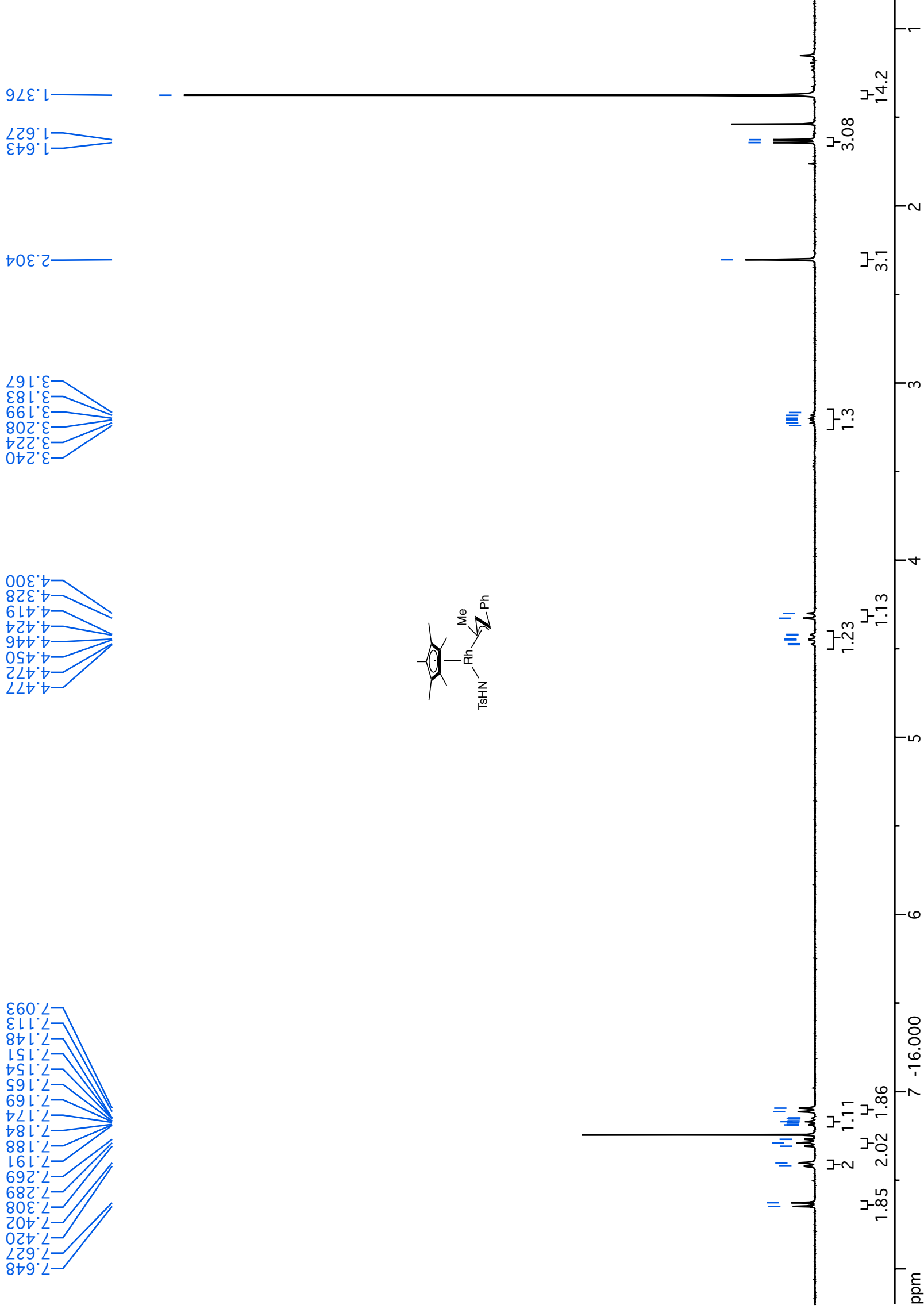
4.611  
4.608  
4.589

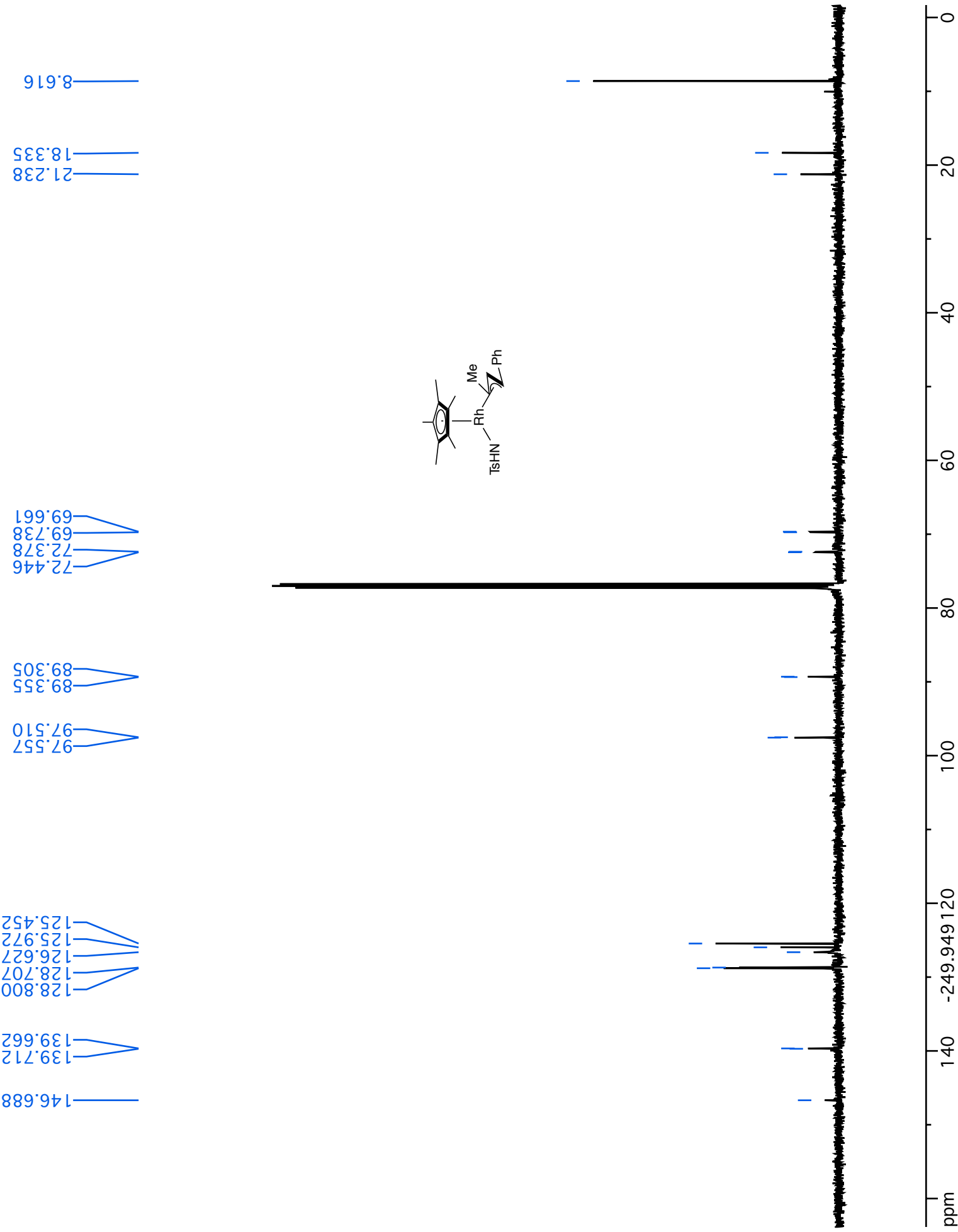
7.407  
7.391  
7.376  
7.311  
7.296  
7.291  
7.289  
7.274  
7.262  
7.260  
7.259

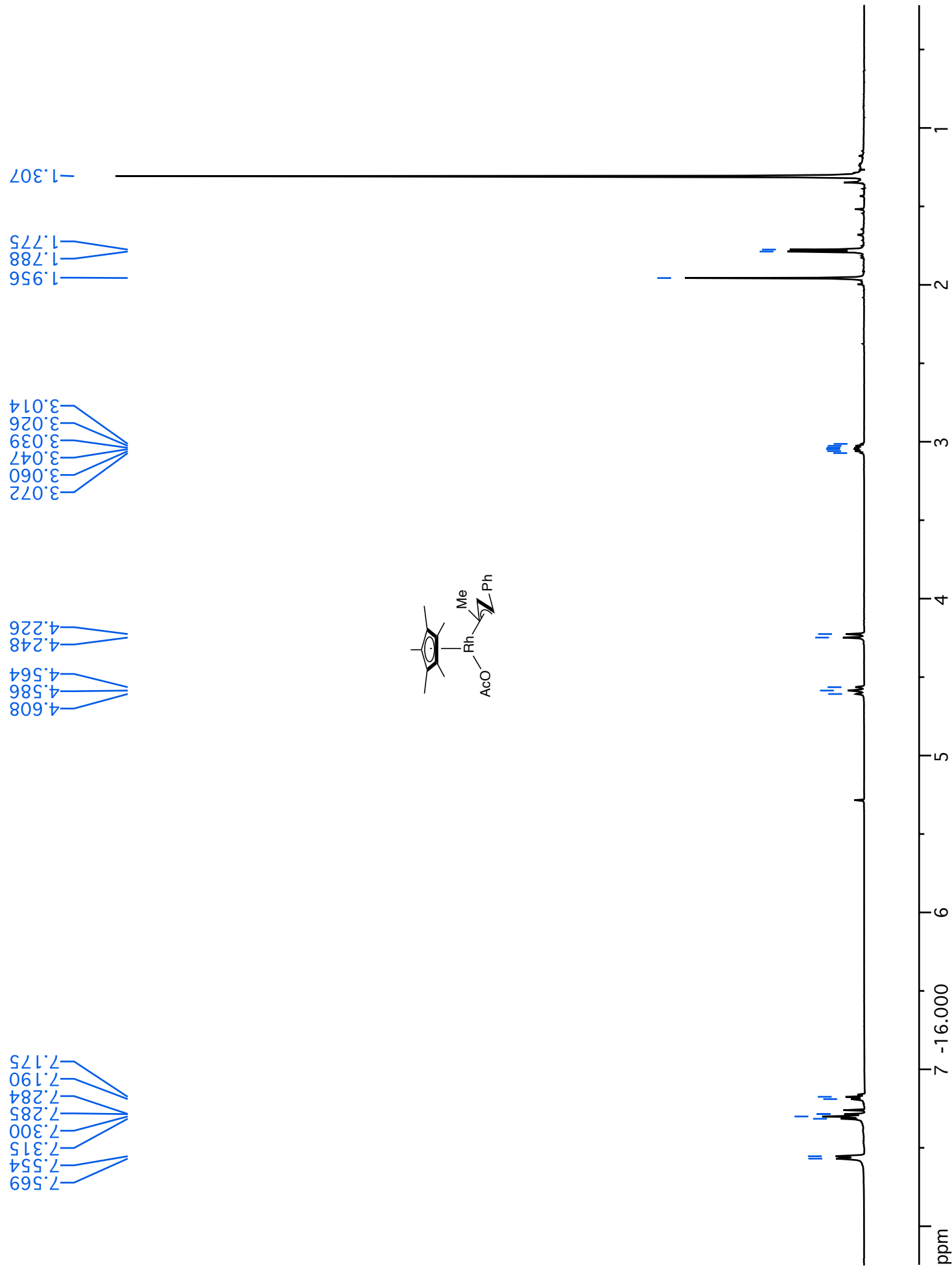












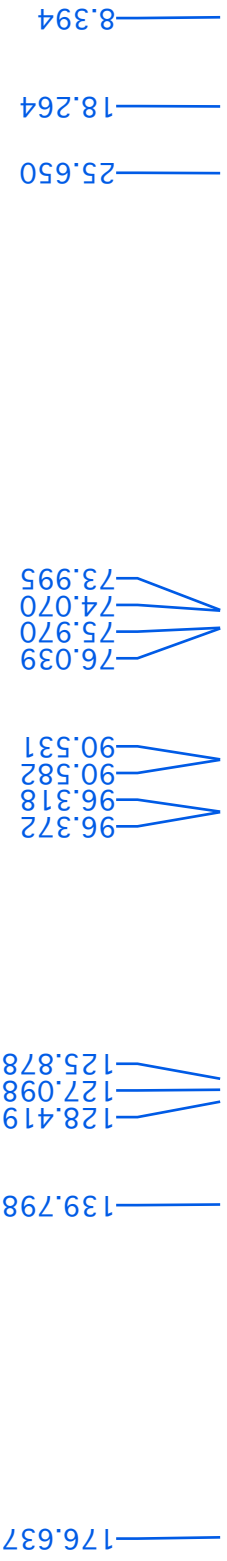
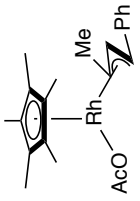
ppm

150

100

50

0



Compiled Allylic Amination Mechanism SI.pdf (8.76 MiB)

[view on ChemRxiv](#) • [download file](#)

---